POLITECNICO DI MILANO

School of Industrial and Information Engineering

Master of Science Degree in Biomedical Engineering

A SEMI-AUTOMATED SEGMENTATION-DRIVEN MORPHING PROCEDURE FOR CORONARY STENTS RECONSTRUCTION FROM OCT IMAGES

Supervisor: Prof. Luca Mainardi

Co-supervisor: PhD. Stud Eng. Marco Bologna, Dott. Eng. Eros Montin

Master of Science Thesis of: Carl Mark Magsino (852892)

Table of contents

Acronyms and abbreviations

BMS	Bare Metallic Stent
BRS	BioResorbable Stent
CAD	Computer Aided Design
COP	Cloud Of Points
CD	Coronary Disease
CP	Control Points
CT	Computed Tomography
CFD	Computational Fluid Dynamics
DES	Drug Eluting Stent
FD-OCT	Frequency Domain Optical Coherence Tomography
GA	Genetic Algorithm
GUI	Graphical User Interface
ISR	In-Stent Restenosis
ITK	Insight Tool Kit
IVOCT	IntraVascular Optical Coherence Tomography
IVUS	IntraVascular UltraSound
LAD	Left Anterior Descending
LMCA	Left Main Coronary Artery
µCT	Micro-Computed Tomography
MI	Mutual Information
MICS	Minimally Invasive Cardiac Surgery
MSE	Mean Square Error

NGF	Normalized Gradient Field
NMI	Normalized Mutual Information
NURBS	Non-Uniform Rational B-Splines
OCT	Optical Coherence Tomography
PDF	Probability Density Function
POBA	Plain Old Balloon Angioplasty
PTA	Percutaneous Transluminal Angioplasty
RCA	Right Coronary Artery
SAM	Surface Adherent Monocyte
TD-OCT	Time Domain Optical Coherence Tomography
TIM	Tissue Infiltrating Monocyte
VF	Vector Fields
VFA	Vector Field Affine
VFB	Vector Fields B-spline
VFR	Vector Field Roto-translation
VFS	Vector Fields Scaling
VFT	Vector Fields Translation
VSMC	Vascular Smooth Muscle Cell
WSS	Wall Shear Stress

Sommario

Introduzione

Tra le patologie cardiovascolari più ricorrenti ci sono quelle coronariche (CD, dall'inglese *coronary disease*). L'aterosclerosi ha un ruolo importante nell'insorgenza di tali patologie; essa consite nella formazione di placche contenenti grassi, calcio e cellule muscolari lisce in corrispondenza della tunica intima. La degenerazione dello stato del vaso dovuto all'accumularsi di tali sostanze può portare alla stenosi (ingrossamento del lume del vaso) o trombosi (spaccatura della placca in particelle con conseguente circolazione nel sangue). Questi, dopo un periodo di tempo, possono causare infarti o ictus al paziente.

La tecnica più usata per curare l'aterosclerosi è l'angioplastica con palloncino (Figura 1), con successivo impianto di stent. Le principali problematiche che possono nascere da questo impianto riguardano soprattutto il fenomeno di ristenosi (o ISR, dall'inglese *In-Stent Restenosis*) e trombosi. Il primo, consiste in una crescita anomala di tessuto fibroso attorno alle maglie della protesi vascolare; il secondo, come già accennato precedentemente, nella rottura dei coaguli formatisi sulla superficie del dispositivo.
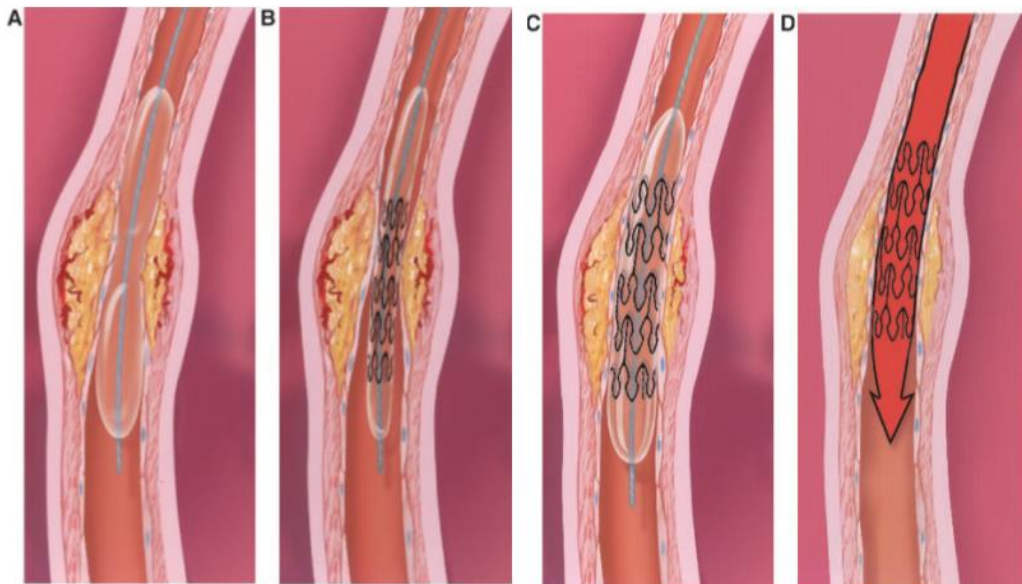
Figura 1 Angioplastica con palloncino e impianto di stent. A) Un catetere alla cui sommità è installato un palloncino (ancora sgonfio) è spinto fino alla zona stenotica ed espanso. B) Stesso tipo di palloncino attorno al quale viene posto lo stent. C) Il rigonfiamento del palloncino provoca l'espansione del dispositivo e la sua adesione alle pareti del vaso. D) Il palloncino è sgonfiato e rimosso lasciando in-loco lo stent. Immagine presa da [1]*.*

L'individuazione preventiva dell'ISR è importante per non causare peggioramenti nello stato di salute del paziente. Un'analisi dettagliata attraverso acquisizioni di immagini del complesso coronaria-stent e successive costruzioni di modelli possono aiutare i medici, permettendo di predire possibili effetti a lungo termine. È infatti emerso dalla letteratura [2], [3] che una delle principali cause della ristenosi può essere dovuta all'alterazione della circolazione sanguigna causata dall'inserimento dello stent. L'impianto del dispositivo, infatti, genera zone di ricircolo oppure zone a basso sforzi di taglio, che possono portare all'insorgenza di ristenosi. Per questo motivo, lo studio della fluidodinamica, attraverso simulazioni computerizzate (CFD, *computational fluid dynamics*) su modelli tridimensionali dello stent *in-vivo*, possono aiutare a risalire a monte del problema [3].

La ricostruzione di modelli tridimensionali di stent *in-vivo* può essere ottenuto con tecniche di imaging. Tra queste, grande importanza è la tomografia a coerenza ottica intravascolare (IVOCT, dall' inglese *IntraVascular Optical Coherence Tomography*). Tale tecnica è basata sull'utilizzo di raggi infrarossi e consente di ottenere immagini con risoluzione di 10-20 μm, circa dieci volte maggiore rispetto ad altre tecniche tradizionalmente utilizzate nella pratica clinica [4] (Figura 2). L'elevata risoluzione permette di distinguere in maniera dettagliata le sezioni del dispositivo (*strut*), consentendo a sua volta, da queste immagini di sezioni, di ricostruire la geometria tridimensionale dello stent, anche nel caso di geometrie complesse.

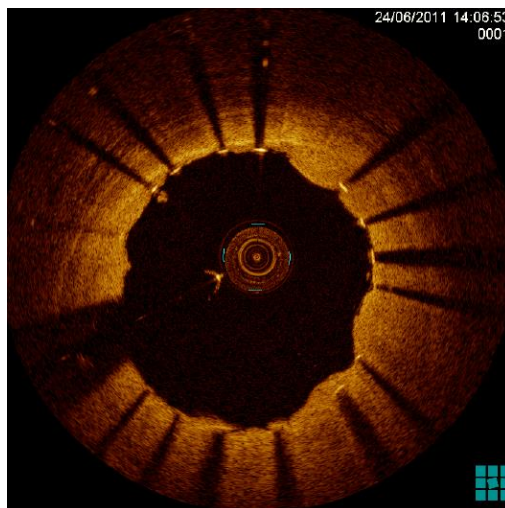*Figura 2 Immagine della sezione trasversale di un vaso acquisita tramite imaging IVOCT (IntraVascular Optical Coherence tomography). Le strut dello stent sono chiaramente visibili grazie all'elevata risoluzione spaziale dell'IVOCT, che consente la valutazione della malappposizione dello stent. Le strut dello stent nella figura sono identificabili come pixel ad alta luminosità seguite da linee d'ombra. Immagine tratta da* [5]*.*

Sommario

In letteratura si possono già trovare alcuni algoritmi di ricostruzione della geometria dello stent. La maggior parte di questi, partono dalla segmentazione delle immagini OCT. Come nel caso di Migliori et al. [2], in cui le immagini segmentate generano nuvole di punti (COP, dall'inglese *Cloud Of Points*) che verranno utilizzate per guidare un processo di *morphing* di un modello CAD (dall'inglese *Computer Aided Design*) dello stent indeformato (Figura 3). In altri lavori, come in Ellwein et al. [6], la geometria dello stent *in-vivo* è ottenuta attraverso l'utilizzo di un modello idealizzato che viene fatto aderire alla geometria riscostruita del lume attraverso l'allineamento delle immagini IVOCT rispetto ad una linea guida, ottenuta da scansioni di micro-tomografia computerizzata (micro-CT o μCT, dall'inglese *Micro-Computed Tomography*). Sottraendo in seguito da questa operazione il lume ricostruito, si ottiene una stima della geometria dello stent. L'uso di modelli non idealizzati è alla base del metodo di ricostruzione adottato da diversi autori [7]–[15]. In questi lavori, i punti dello stent e i contorni del lume sono delineati manualmente in ogni immagine IVOCT e successivamente, connessi attraverso tecniche di interpolazione. In O'Brien et al. [16], si sfrutta di nuovo la nuvola di punti (come in Migliori et al. [2]), alla quale si applica un *fitting* di uno stent con geometria nota, che verrà poi deformata usando tecniche di interpolazione; successivamente, allo scheletro deformato della protesi vascolare, viene costruita la vera struttura attraverso il metodo di *swept cross-section*.

Il metodo proposto in questa tesi, basato sulla registrazione di immagini tridimensionali, mira ad automatizzare, almeno in parte, il lavoro di ricostruzione, velocizzando in questo modo il processo; in contrasto con gli altri metodi, nei quali la geometria dello stent è ottenuto spesso attraverso una procedura non automatizzata che richiede maggiori tempi di elaborazione, come nel caso del *morphing* manuale. Inoltre, diversamente da alcuni algoritmi (Ellwein et al. [6]), questo metodo utilizza modelli di stent geometrici non ideali, ma provenienti da segmentazione di immagini IVOCT con caratteristiche e geometrie note.
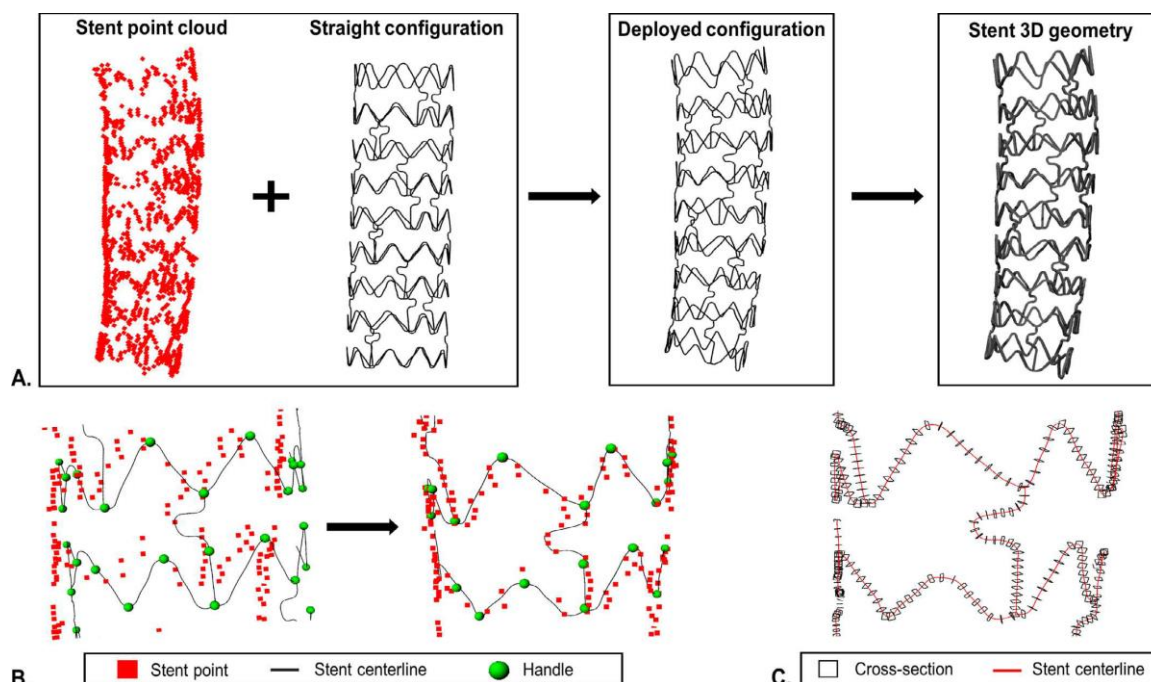
Figura 3 Descrizione del metodo di Migliori et al. [2] per la ricostruzione della geometria dello stent 3D. A) La nuvola di punti (cloud of points o COP) dello stent ottenuto mediante tomografia a coerenza ottica e la configurazione non deformata della centerline (ottenuta da micro-tomografia computerizzata) vengono utilizzati per generare la configurazione deformata su cui viene costruita la geometria 3D dello stent. B) Morphing della centerline con l'uso deglio handles, attraverso la minimizzazione della distanza di queste con i punti della COP. C) Procedura basata sul loft di sezioni trasversali dello stent posizionate lungo la centerline. Immagine tratta da [2].

Materiali e metodi

Il metodo proposto per la ricostruzione della geometria dello stent è stato sviluppato utilizzando MATLAB (versione 2017, Mathworks, Natick, MA, USA). In aggiunta, viene utilizzato anche PARAVIEW (versione 5.5, Kitware, Clifton Park, NY, USA) come software di rendering grafico per avere un confronto dei risultati della ricostruzione.

L'algoritmo si basa sulla registrazione dell'immagine tridimensionale (ottenuta da un modello CAD) dello stent non deformato sull'immagine proveniente dalla segmentazione di immagini IVOCT ed esporatate come nuvola di punti (ottenute dal lavoro di tesi di Marco Bologna [17]). Il campione usato per questa prova è lo XIENCE V (Abbot Vascular, Santa Clara, CA, USA), uno stent metallico con diametro di 3 mm e lunghezza nominale effettiva di 28 mm (Figura 4).
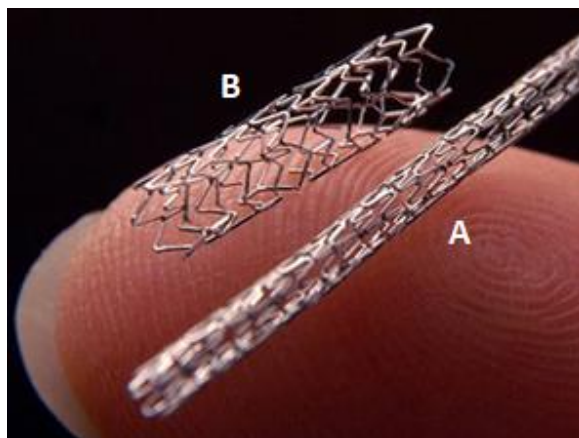
Sommario

Figura 4 Fotografie digitali che mostrano lo stent metallico non espanso (A) ed espanso (B). Immagine tratta da [18]

La procedura di ricostruzione parte con la conversione della nuvola di punti e del modello CAD in immagini tridimensionali, rispettivamente attraverso un'interpolazione B-spline e una tecnica che si basa su triangolazione. Ottenute le immagini, queste vengono nuovamente binarizzate, dato che durante la loro creazione, tale proprietà era stata persa. Successivamente, per diminuire il volume di calcolo, vengono ridotti i voxels (con valore nullo) più esterni allo stent, lasciando un margine di 20 (voxels) per permettere maggior spazio di manovra durante la fase di registrazione.

La procedura di creazione della geometria del dispositivo sfrutta la registrazione d'immagini tridimensionali, considerando l'immagine proveniente da IVOCT come fissa e quella dal modello come mobile. La registrazione si basa fondamentalmente su trasformazioni rigide (traslazione e rotazione) e non rigide (deformazioni basate su interpolazione B-Spline). In aggiunta a queste, vi sono anche lo scaling e una trasformazione lineare affine.

La registrazione sfrutta degli algoritmi provenienti da *Insigth Tool Kit (ITK)* [19], una libreria open source per l'image processing, e rielaborate in forma di eseguibili da Eros Montin [20]. In queste eseguibili è possibile selezionare tra varie metriche da ottimizzare: *Mean Square Error (MSE), Normal Gradient Fields (NGF) e Mutual Information (MI)*. Il calcolo di queste funzioni ad ogni iterazione tiene conto della bontà di sovrapposizione delle immagini e attraverso la discesa del gradiente, tale sovrapposizione viene ottimizzata riaggiornando i parametri di registrazione (3 per traslazione, 6 per rototraslazione, 3 per scaling e 12 per affine). In questa sperimentazione sono stati usati come metriche MSE e MI.

La procedura è suddivisa in due parti: registrazione globale e locale. Tale suddivisione è dovuta all'impossibilità di applicare la registrazione non-rigida (attraverso la B-Spline) sull'intero immagine di stent per l'enorme volume di calcoli richiesto. Perciò, si è proceduto

prima ad allineare l'immagine intero del modello rispetto a quello dell'IVOCT attraverso una traslazione e rototrasalazione. Successivamente, entrambe le immagini sono suddivise in 20 anelli (*rings*), e per ogni anello mobile (CAD) rispetto al corrsipondente fisso (IVOCT), si applicano le seguenti trasformazioni: i) scaling, ii) traslazione, iii) rototraslazione, iv) affine, v) B-Spline come descritto in Figura 5A.

Il ricongiungimento degli anelli (descritto Figura 5B) , per ottenere l'immagine registrata dello stent, viene effettuato sfruttando i campi vettoriali (VF, dall'inglese *vector fields*) che erano stati salvati, per ogni anello, in ogni trasformazione. In tale procedura, la VF dell'n-esimo anello, per ogni trasformazione viene ricongiunta allo stent ricostruito parzialmente all'iterazione precedente. In questo modo si ottengono, alla fine del processo di registrazione di tutti gli anelli, cinque VF per lo stent intero, corrispondenti alle cinque trasformazioni.

Il modello finale è ottenuto applicando all'immagine iniziale dello stent le cinque VF nello stesso ordine di trasformazione definito in precedenza (Figura 5C).

Per valutare la qualità dell'algoritmo si è cercato di confrontare la registrazione con un altro processo analogo tra un altro modello 3D dello stesso caso (ottenuto mediante µCT) e l'immagine IVOCT di riferimento [17]. Per prima cosa, è stata creata una superficie 3D dall'immagine dello stent deformato. È stato poi utilizzato il software MIMICS (Materialise, Leuven, Belgium) per calcolare la *centerline* (termine usato per definire lo scheletro dello stent) del modello registrato, ottenuta sotto forma di COP. Tale centerline è stata confrontata con la nuvola di punti contenente i centroidi delle strut nelle immagini IVOCT. Da ogni punto della COP dell'IVOCT è stata calcolata la distanza rispetto al punto più vicino della COP della centerline ottenuta dal CAD. Queste distanze sono state poi confrontate con quelle provenienti dalla tesi di Bologna [17]. Il confronto tra le due distribuzioni è stato fatto attraverso un test statistico (Mann-Whitney). In aggiunta, è stata analizzata anche la bontà di registrazione per ogni anello facendo un confronto tra tutti e 20 gli anelli.
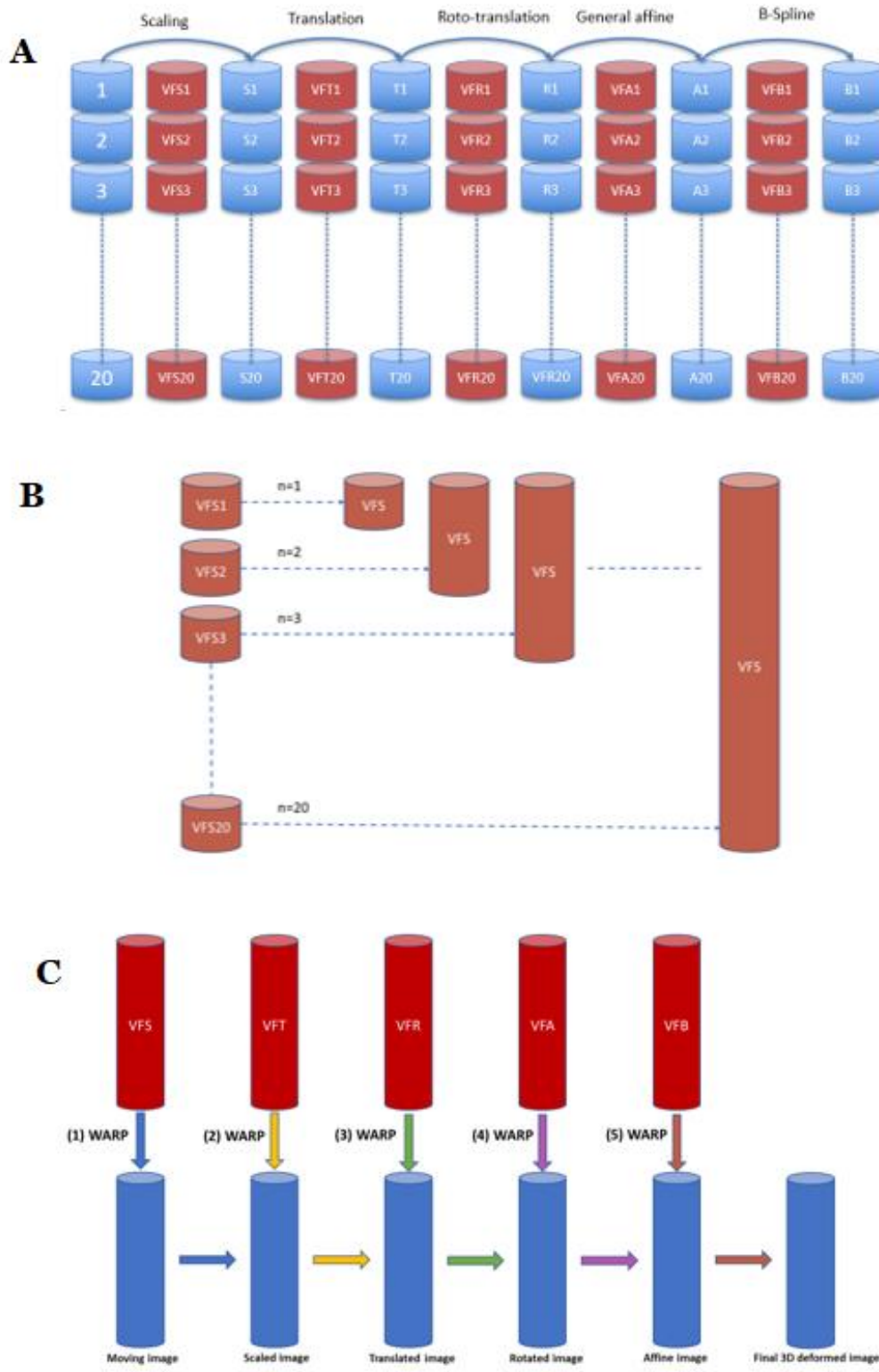
Figura 5 Immagine che descrivono le tre fasi della ricostruzione della geometria dello stent. A) Schema della registrazione locale ring per ring con ordine di trasformazione predefinito; gli output di ogni registrazione sono i vector fields (VFS, VFT, VFR, VFA, VFB) di ogni ring. B) Schema del processo di ricostruzione del VF dell'intero stent per ogni trasformazione attraverso il ricongiungimento dei VF dei singoli rings. C) Applicazione in cascata delle 5 VF totali, partendo dall'immagine dello stent non deformato di partenza, per ottenere infine la geometria dello stent deformato.

Risultati e conclusioni

La validazione del metodo è stata eseguita su un campione di nuvola di punti proveniente dalla segmentazione di immagini IVOCT. In Figura 6 A, si può vedere l'immagine dello stent (blu) dopo la registrazione e in Figura 6 B, la sua sovrapposizione con l'immagine della nuvola di punti (verde). Si può osservare una buona sovrapposizione delle strutture delle due immagini, in particalore nella zona distale (dal primo a circa il decimo ring, Figura 6 D), dove vi è una giusta corrispondenza tra le due immagini, a dimostrazione della buona riuscita sia della trasformazione rigida che non rigida. Nella zona prossimale (da circa l'undicesimo ring fino alla fine, Figura 6 C), si osserva comunque una buona deformazione globale, in particolare nella direzione radiale dello stent; ma non c'è una perfetta corrispondenza tra le due geometrie.
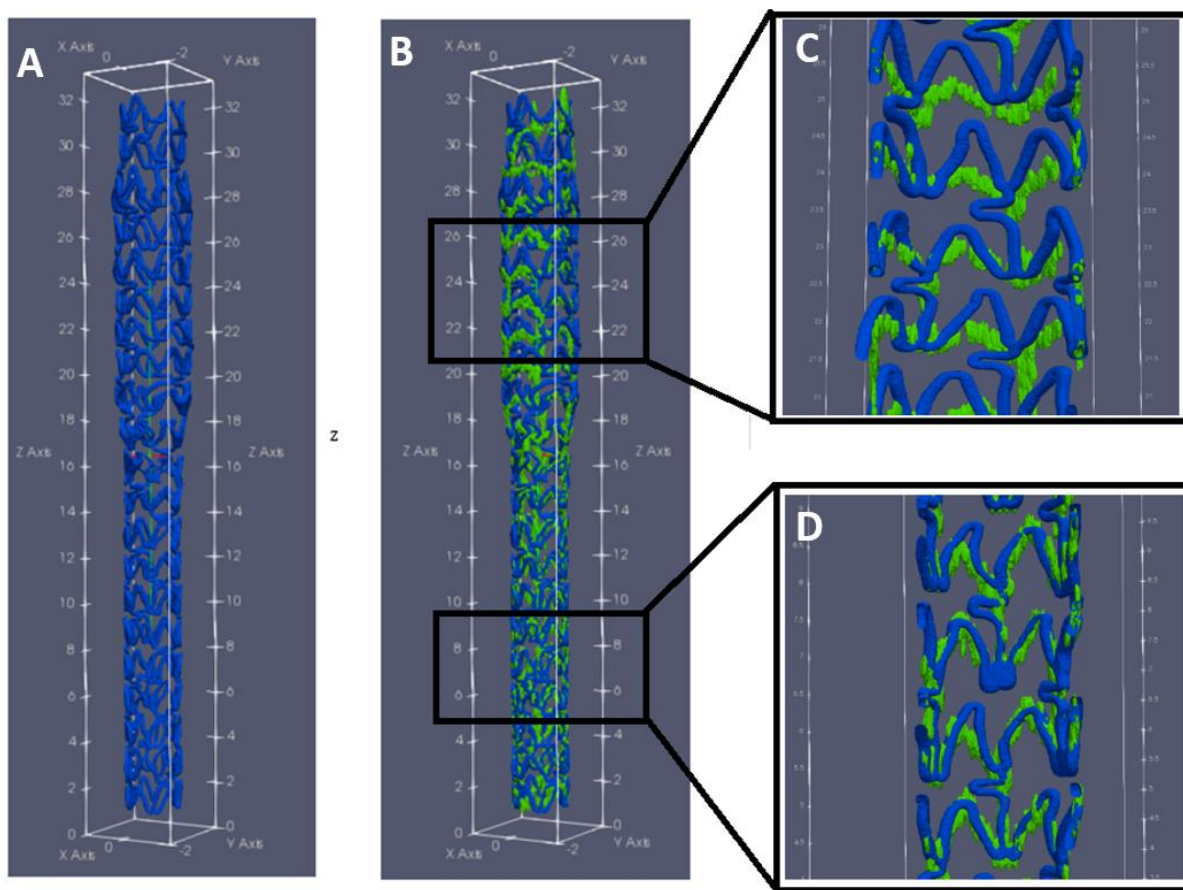
Figura 6 Immagini che mostrano i risultati del modello registrato (A) e la sua sovrapposizione con l'immagine di riferimento (verde) proveniente dall'IVOCT (B). In (C), nella parte prossimale (tra circa l'undicesimo ring fino al ventesimo) si dimostra una buona registrazione a livello macroscopico (giusta rotazione e scaling) e meno al livello di deformazione locale. In (D) nella parte distale (dal primo al decimo ring) si osserva una ottima sovrapposizione tra le due immagini anche al livello dei dettagli delle due strutture.

Il test statistico di Mann-Whitney sulle distanze ha dimostrato che le distanze tra punti corrispondenti nei due stent sono significativamente maggiori rispetto alla registrazione tra IVOCT e μCT da parte di Bologna [17], come si vede nei boxplots in Figura 7 . La differenza però non è netta, visto che l'ordine di grandezza è il medesimo e la distanza tra le mediane è di circa 40 μm. Questo risultato potrebbe essere attribuito a diverse cause: la non-uniformità dei ring IVOCT in direzione longitudinale, che influisce sulla qualità della registrazione locale; possibili effetti dovuti alla rotazione relativa tra i rings nell'IVOCT, dovuti ad artefatti da movimento del catetere OCT che non vengono completamente recuperati nella registrazione; il basso numero di control points per la registrazione non-rigida B-Spline. Nonostante le problematiche evidenziate, questo metodo può esibire in confronto ai metodi disponibili in letteratura un vantaggio notevole. Infatti, la semi automaticità e la relativa velocità nell'ottenere i risultati rendono l'algoritmo una valida alternativa alle procedure manuali di ricostruzione dello stent visti precedentemente, come ad esempio in Migliori et al. [2], dove si applica un *morphing* manuale, che richiede un tempo di applicazione ben superiore ai circa due giorni richiesti nel metodo proposto.

In conclusione, questo studio ha dimostrato che la ricostruzione della geometria dello stent da immagini IVOCT attraverso il *morphing* può essere automatizzata e velocizzata, facilitando enormemente il processo di creazione di modelli 3D per le simulazioni CFD, che daranno informazioni fondamentali sul legame tra emodinamica e insorgenza della ristenosi.
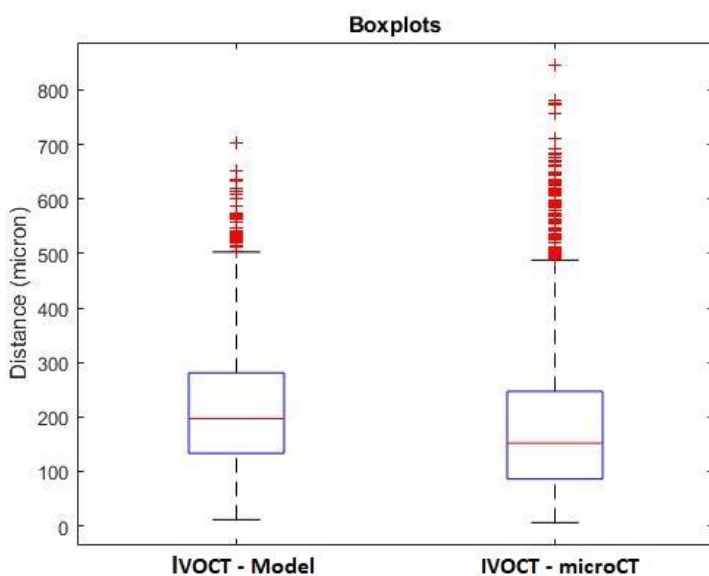

Figura 7 Boxplot che mostrano la distribuzione delle distanze ottenute dal metodo proposto (sinistra) e la distribuzione nella sperimentazione di Bologna [17] (destra). Come si osserva, e confermato anche dai test statistici, le distanze in Bologna [17] risultano inferiori.

Summary

Introduction

Among the cardiovascular pathologies, coronary disease (CD) is one of the most widespread. Atherosclerosis is one of the causes of the insurgence of such disease and it consists into the formation of an atherosclerotic plaque containing fats, calcium and vascular smooth muscle cells (VSMC) in the tunica intima. The accumulation of such substances in the vessel causes its degeneration and, therefore, two phenomena could occur: i) In-stent restenosis or ISR (thickening of the lumen) and ii) thrombosis (disintegration of the atherosclerotic plaque in smaller particles that will circulate in the blood circuit). These complications leave the patient, highly exposed to heart attack and ictus.

The most used technique against atherosclerosis is the balloon angioplasty, followed by a stent implantation (Figure 1). Despite the success in restoring the normal blood flow in the vessel, the presence of the stent may cause ISR and thrombosis in the long term. In restenosis, an anomalous growth of fibrotic tissue surrounding the stent structure, is observed. In the thrombosis, the rupture in many smaller particles of the clot that has deposited on the surface of the stent, may cause their circulation in the blood flow.
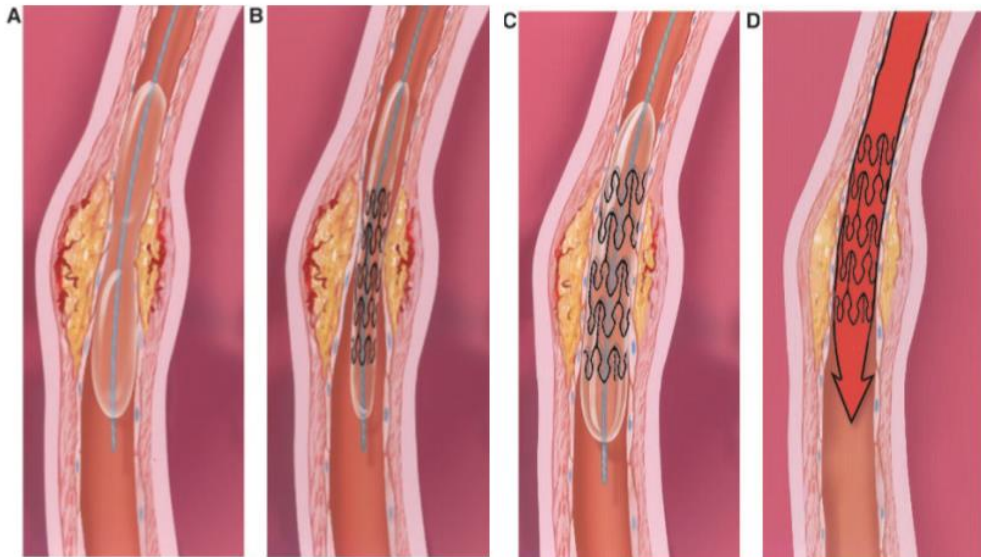
Figure 1 Balloon angioplasty and stenting. A) A balloon-tipped catheter is positioned in the coronary artery narrowing and inflated. B) A stented balloon is inserted in the stenotic site. C) The balloon inflation causes the stent to expand and adhere to the artery walls. D) The balloon is deflated and took out leaving the stent scaffolding the vessel. Image taken from [1]*.*

Summary

Early detection of ISR is important to avoid worsening the patient's health. Performing a detailed analysis through image acquisitions of the coronary-stent complex and model constructions can help physicians to predict possible long-term complications. As a matter of fact, it has emerged from the literature [2], [3] that one of the main causes of restenosis may be due to the changes in blood circulation due to the presence of the stent. In fact, the implantation of a stent produces alterations in physiological hemodynamics, creating recirculation or low shear areas, which can lead to ISR. For this reason, performing computational fluid dynamics (CFD) simulation on tridimensional model of the stent is important to understand the causes of these pathologies.

The reconstruction of three-dimensional models of in-vivo stents can be obtained with imaging techniques. Among these, intravascular optical coherence tomography (IVOCT) plays an important role. This technique uses infrared light and allows to obtain images with a resolution of 10-20 µm, about ten times greater than other imaging techniques [4] (Figure 2). The high resolution allows to distinguish the cross-sections of the stent, enabling to reconstruct the three-dimensional geometry of the device, even in the case of complex geometries.
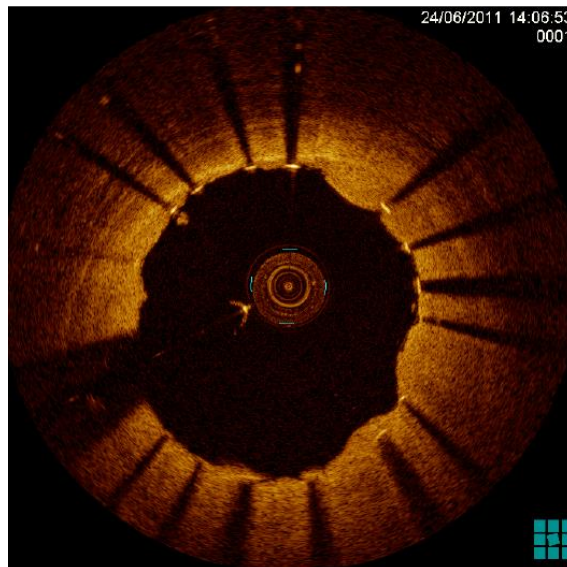
Figure 2 Cross-section image of a vessel acquired through IVOCT (Intravascular optical coherence tomography). Stent's strut is clearly visible thanks to the high spatial resolution capability of IVOCT, enabling the assessment of stent's malappostion. Struts in the figure are identifiable as high brightness area followed by shadow lines [5].

Summary

In the literature some algorithms of reconstruction of the stent geometry can already be found. Most of these begin with the segmentation of OCT images, as in the case of Migliori et al. [2] in which the segmented images generate cloud of points (COP) of stent, that will be used in the reconstruction through the morphing of an undeformed stent from Computer Aided Design or CAD (Figure 3). In other works, like in Ellwein et al. [6], the geometry of the *in-vivo* device is obtained using an idealized stent model that was deformed to adapt to the reconstructed geometry of the lumen, with the alignment of IVOCT images with respect to the guideline that was extracted from micro-computed tomography (micro-CT or μCT) scans. Subtracting from this operation the reconstructed lumen, an estimate of the stent geometry is obtained. The use of non-idealized models is common in the works of several authors [7]–[15]. In these works, lumen and stent points are manually outlined in each IVOCT images and subsequently, connected through interpolation techniques. In O'Brien et al. [16], the COP is used again (like in Migliori et al. [2]). A fitting of a stent with known geometry is applied to the COP, which will then be deformed using interpolation techniques; subsequently, the true structure is built by the cross-section swept method to the deformed skeleton of the stent.

The method proposed in this thesis, based on the registration of three-dimensional images, aims at automatizing, although partially, the reconstruction work, with a result of a much faster process with respect to other methods seen in literature, such as in Migliori et al. [2] where a morphing is proposed, in which the geometry of the stent is obtained manually, with a consequence of higher elaboration time. Moreover, unlike other algorithms (Ellwein et al. [6]), this method uses non-idealized geometrical stent models; instead, it uses samples coming from the segmentation of IVOCT images with known characteristics and geometries.
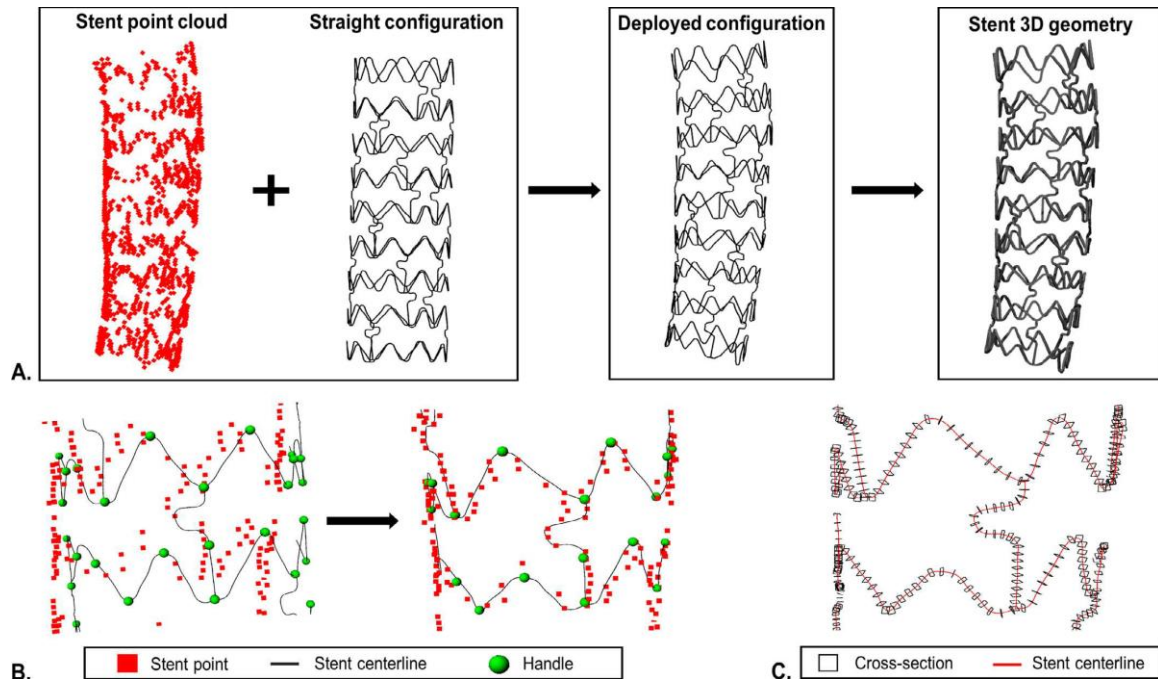
Figure 3 Step by step schematic of Migliori et al. 3D stent geometry reconstruction. A) The COP of the stent (obtained from optical coherence tomography scans) and the straight configuration of the centerline (obtained from micro-computed tomography) are used to generate the deployed configuration of the centerline and the stent 3D geometry. B) Morphing of the stent centerline using the handles so that their distances with the selected stent are minimized. C) Curve loft of the stent strut cross-sections along the morphed stent centerline. Image taken from [2]*.*

Materials and methods

The proposed method for the reconstruction of the stent geometry was developed using MATLAB (version 2017, Mathworks, Natick, MA, USA). In addition, PARAVIEW (version 5.5, Kitware, Clifton Park, NY, USA) is also used as a graphical rendering software to compare the results of the reconstruction.

The algorithm is based on the registration of the CAD of the non-deformed stent on the image coming from the segmentation of IVOCT images and exported as a COP (obtained from Marco Bologna's thesis work [17]). The stent that was used as a sample for this test is the XIENCE V (Abbott Vascular, Santa Clara, CA, USA), a metallic device with a diameter of 3 mm and an effective nominal length of 28 mm (Figure 4).

Summary

Figure 4 Digital photographs showing a metallic stent in crimped (A) and expanded (B) forms. Image from [18].

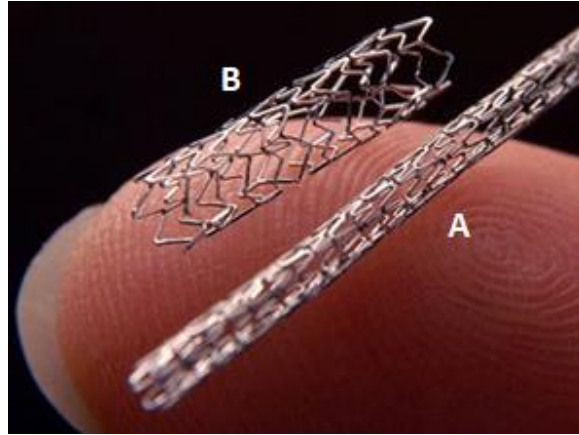The reconstruction procedure begins with the conversion of the COP and of the CAD model into three-dimensional images, respectively through a B-spline interpolation and a technique based on triangulation. Once the three-dimensional images are obtained, they are re-binarized as the property was lost during their creation. Subsequently, to decrease the computational volume, the voxels of the images are reduced by eliminating those (with null value) more external to the stent, up to leaving 20 voxels around the margins to increase the registration maneuverability.

The procedure of creating the stent geometry exploits the registration of three-dimensional images, considering the one coming from IVOCT as fixed and the image from the model as mobile. The registration is based on rigid (translation and rotation) and non-rigid transformations (deformations based on B-Spline interpolation). In addition to these, there is also scaling and a general affine transformation.

The method uses algorithms from the Insight Tool Kit (ITK) [19], an open source library for image processing, and re-elaborated in the form of executables by Eros Montin [20]. In these executables it is possible to select from various metrics to be optimized: Mean Square Error (MSE), Normal Gradient Fields (NGF) and Mutual Information (MI). The calculation of these functions at each iteration considers the goodness of the overlap between the images and through the descent of the gradient, this overlap is optimized by updating the registration parameters (3 for translation, 6 for roto-translation, 3 for scaling and 12 for affine). In this experimentation, MSE and MI metrics were used.

The procedure is divided into two parts: global and local registration. Such subdivision is due to the impossibility of applying the non-linear registration (through the B-Spline) on the entire image of the stent due to the huge computational cost of the operation. The whole image

of the model was first aligned with respect to that of the IVOCT through a global translation and roto-translation. Subsequently, both images are divided into 20 rings and for each moving ring (model) a local image registration is performed with respect to the fixed counterpart (IVOCT). The local registration consists of the following transformations: i) scaling, ii) translation, iii) roto-translation, iv) general affine, v) B-Spline as described in Figure 5A. The rebuilding of the rings (described in Figures 5B), to obtain the registered image of the stent, is carried out using the vector field (VF) that were saved, for each ring, in each transformation. In this procedure, the VF of the nth ring, for each transformation, is rejoined to the VF of the partial reconstructed stent of the previous iteration (as described in Figure 5B for VFS). In this way, at the end of the registration process of all the rings, five VF's (VFS – for scaling, VFT – for translation, VFR – for roto-translation, VFA – for general affine, VFB – for B-Spline), are obtained for the whole stent, corresponding to the five transformations.
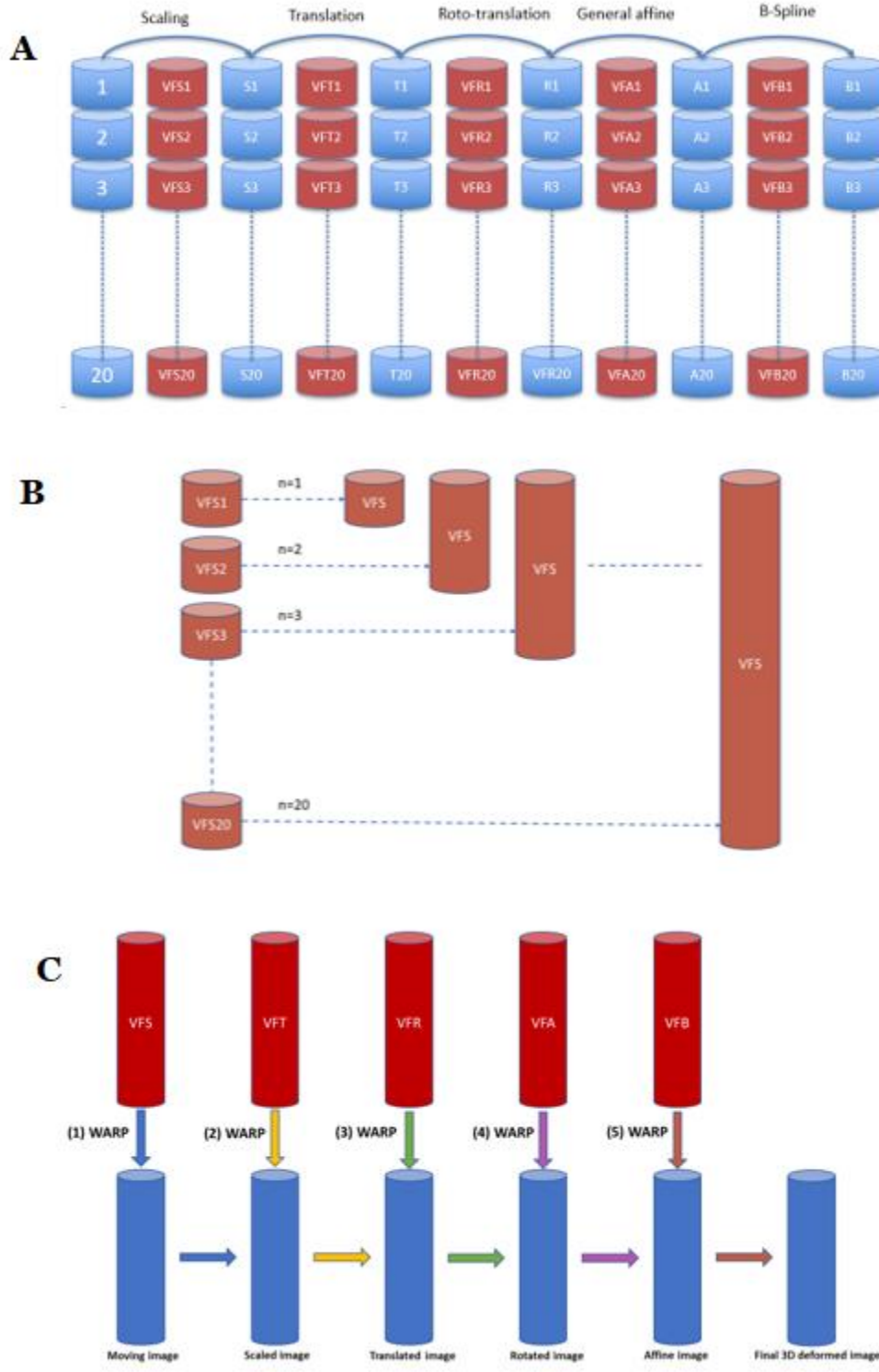
Figure 5 Image describing the three phases of stent's geometry reconstruction. A) Scheme of the local ring-by-ring registration with a fixed transformation order; the outputs of each registration are the vector fields (VFSn, VFTn, VFRn, VFAn, VFBn) of each ring. B) Diagram of the reconstruction process of the entire stent VF for each transformation through the re-joining of the VF of the rings. (C) Having obtained the VF of the 5 transformations for the entire stent, these are applied in cascade beginning with the image of the non-deformed stent, to finally obtain the geometry of the deformed stent.

The final model is obtained by applying to the initial image of the stent the five VF's in the same order of transformations previously defined, as described in Figure 5C.

To evaluate the quality of the algorithm, the registration performed in this study has been compared to a similar registration performed between a 3D model of the same stent (obtained by μCT) and the reference IVOCT image from the thesis of Bologna [17]. First a 3D surface of the deformed stent has been created from the 3D image. The software MIMICS (Materialise, Leuven, Belgium) has been used to extract the centerline (the skeleton) of the deformed CAD, which was obtained as a COP. The centerline has been compared to the COP of the centroids of the strut in IVOCT images. From each point of the IVOCT COP, the distance to the closest point of the deformed CAD centerline has been computed. The obtained distances were then compared with the ones from the thesis of Bologna [17]. The comparison between the two distances distributions was done through a statistical test (Mann-Whitney). In addition, the goodness of registration for each ring was also analyzed by comparing the distances between the IVOCT centerlines and the registered model, among all 20 rings.

Results and conclusions

The validation of the method was performed on a 3D COP coming from the segmentation of IVOCT images. Figure 6A shows the image of the stent (blue) after registration and Figure 6B shows its overlap with the 3D COP IVOCT image (green). It can be observed a good overlap of the structures of the two images, especially in the distal zone (from the first to about the tenth ring, Figure 6D), where there is a correct correspondence between the two stents, which demonstrates the success of both the rigid and non-rigid transformations. In the proximal region (from about the eleventh ring up to the end, Figure 6C), a good global deformation is observed, in particular in the radial direction of the stent, although the registration locally resulted a little worse, since there is no perfect correspondence between the two geometries.
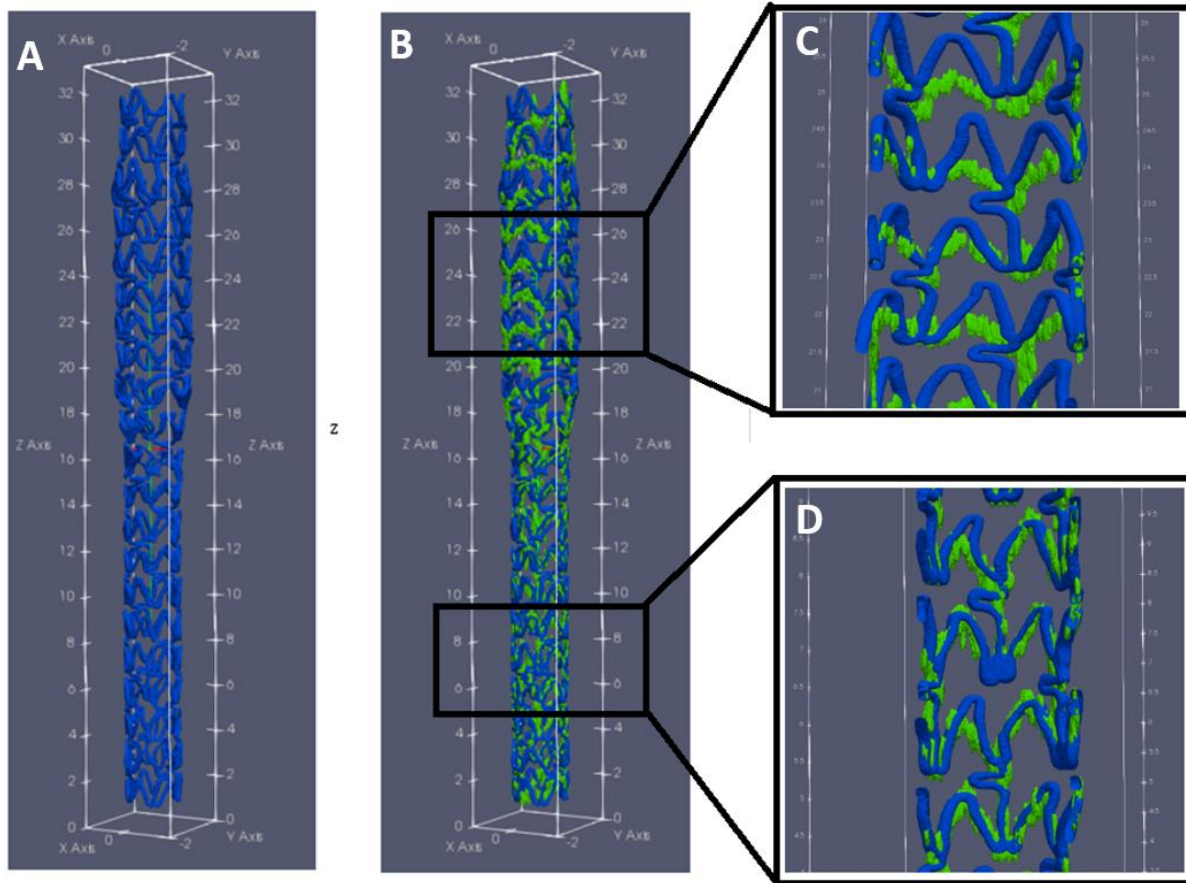
Figure 6 Images showing the results of the registered model (A) and the superimposition with the reference image (green) from the IVOCT (B). In (C), in the proximal part (from about the eleventh ring up to the twentieth) a good registration at the macroscopic level (good rotation and scaling) and less regarding the local deformation level is demonstrated. In (D), in the distal part (from the first to the tenth ring), it can be observed an excellent matching between the two images also at the level of the details of the two structures.

The Mann-Whitney statistical test on the distances computed for this method is significantly worse compared to the IVOCT-µCT registration by Bologna [17] as is also shown in the boxplots in Figure 7. However, the order of magnitude is the same and the distance between the medians is about 40 µm. The possible causes to which this result can be attributed, might be: the non-uniformity of the IVOCT rings, that reduces the quality of local registration; from possible effects due to the relative twist among the rings in the IVOCT, that are due to catheter motion artifacts and that are not completely recovered in the local registration; the relatively low number of control points for the B-spline local registration. Despite such limitations, the proposed method offers an important advantage over other from the literature. In fact, the semi-automaticity and the relative speed make the algorithm a good alternative to the manual procedure stent reconstruction previously seen, such as in Migliori et al. [2], where a manual

morphing is applied, which requires a time of application well above the two days required in the proposed method.

In conclusion, this study showed that the reconstruction of the stent geometry from IVOCT images through morphing can be automatized and sped up. This will surely facilitate the process of creating 3D models for CFD simulations, which will help understanding the link between hemodynamics and ISR insurgence.
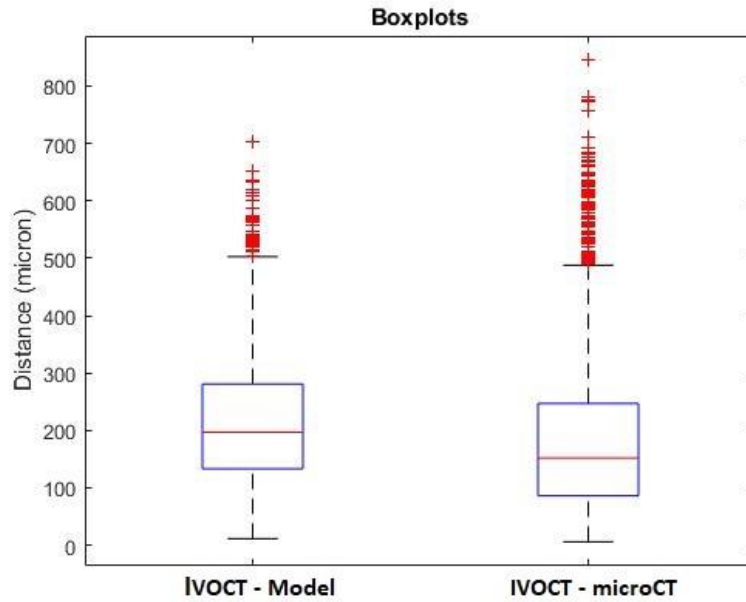
Figure 7 Boxplots showing the distribution of distances obtained from the proposed method (left) and the distribution in the experimentation of Bologna. [17] *(right). As observed, and confirmed by the statistical tests, the distances in Bologna* [17] *are better because they are inferior with respect to the ones obtained in this thesis.*

1.

Coronary atherosclerosis

This chapter aims to explain first the anatomy of the coronary focusing on its main parts and subsequently, there are exposed some details about the atherosclerosis, its causes and the surgical approach for its treatment.

1.1. Coronary anatomy

Coronary arteries are responsible for delivering the nutrition to the heart. The cardiac cells, in fact, cannot be fed by the blood circulating in its chambers due to the thickness of the walls. Therefore, diffusion of metabolic substances is not permitted. Diffusion is only possible in the endocardium, while in the myocardium and in the epicardium, mass exchange occurs only at the level of the cardiac capillary vessels.

As shown in Figure 1.1 from the aortic valve of the heart, two small arteries emerge:

- The left main coronary artery (LMCA) which subdivides into two subordinate vessels: the left anterior descending (LAD) and the circumflex arteria (CFX).
- The right coronary artery (RCA) that perfuses the entire right part of the heart.

From these two main arteries, by a series of bifurcations, smaller vessels are generated enabling the perfusion of all the heart cells. Left coronary artery and its branches supply the oxygen to the following districts: almost the entire left ventricle, two third of the anterior atrioventricular septum, partial part of the right ventricle, the heart's apex, the left atrium and finally, the lower portion of the interatrial septum. The right coronary artery and its branches deliver the oxygen to the following districts: the right atrium and right ventricle, the upper part of the interatrial septum, the intraventricular septum and the sinoatrial node.

Deoxygenated blood is collected from the coronary sinus and from the Tebesio's vein. These veins address the blood directly to the right atrium [21].
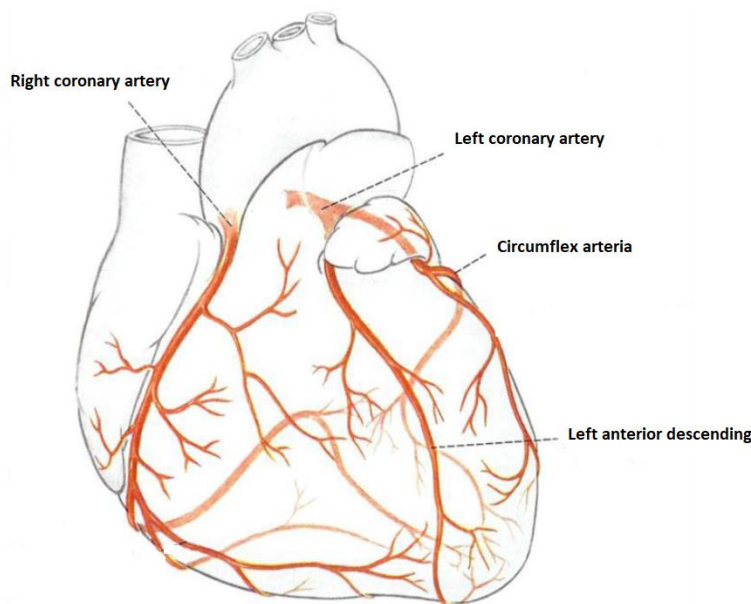
Figure 1.1 Coronary arteries. Image from [22]*.*

Blood flows in the coronary mainly during diastole phase (Figure 1.2) since during systole, coronary vessels are compressed by the left ventricle pumping action which causes the myocardium to contract and decrease the blood flow in the coronary. Consequently, there is an increase of hydraulic resistance inside the artery. Conversely, during diastole, the myocardium muscle is relaxed allowing the blood flow in the arteries.

During rest, blood flow in the coronary is 225 ml/min. This value could increase during exercise sessions up to four to five times [23].

1.2.   Atherosclerosis

Atherosclerosis is a pathology that affects medium-large sized arteries [21] and it is characterized by a hardening of the coronary on the surface of the heart with an increase in thickness of the internal stratum. This is due to the formation of the atherosclerotic plaque which is caused by the accumulation of fats and lipids. Consequently, the artery becomes rigid and the lumen diameter decreases. When waxy substances called plaque, build up inside the coronary arteries, it is used to refer this kind of pathology to coronary disease (CD).
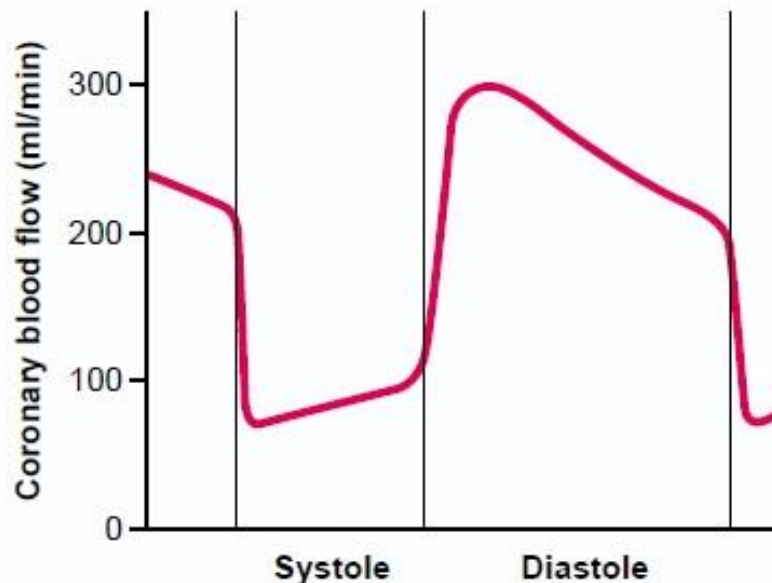
Figure 1.2 Phasic flow of blood through the coronary capillaries of the human left ventricle during cardiac systole and diastole (as extrapolated from measures flows in dogs). Image taken from [24]*.*

Atherosclerotic plaque is a problem mainly for two reasons: i) the formation of a stenosis and ii) the possibility of forming a platelet thrombus. Stenosis is the narrowing or obstruction of the artery due to the tissue damage after the growth of the atherosclerotic plaque (Figure 1.3). Such narrowing increases the hydraulic resistance of the vessel and to maintain the blood flow rate constant, the heart must increase the pumping work bringing to a high blood pressure and an increase of the muscle fatigue. If this process continues constantly, the risk of heart attack is very high. In case the vessel is completely occluded, the cells at the valley of the occlusion lacks the necessary nutrition from the blood and this could cause ischemia (for coronary arteries) or ictus (for cerebral arteries).
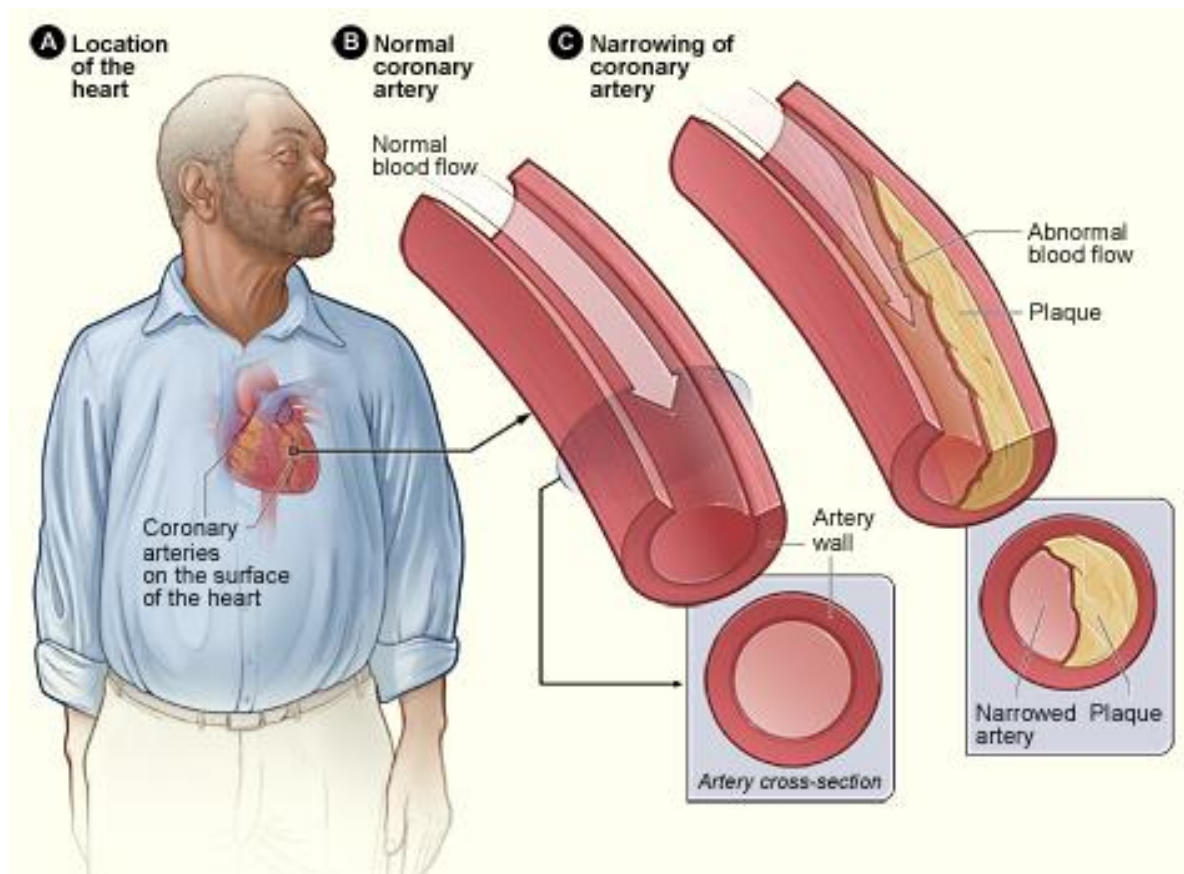
Figure 1.3 A) Location of the heart in the body. B) Normal coronary artery. C) the coronary artery affected by stenosis after the growth of the atherosclerotic plaque. Image taken from [25]

Pressure drop ΔP_S between the two extremities of the stenosis cannot be calculated by the classical Poiseuille law, but it is necessary to make various considerations about the pulsatility of the blood flow and the local pressure drops. Such pressure drops can be calculated by the following equation [26]:

$$\Delta P_S = K_V(\alpha)R_S Q + \frac{\rho R_T}{2A_0^2}\left[\frac{A_0}{A_S} - 1\right]^2 * |Q|Q + K_U L_U \frac{dQ}{dt} \tag{1.1}$$

Where:
- Q is the flow rate in the vessel;
- A_O and A_S are the cross section respectively with and without stenosis;
- R_S is the Poiseuille resistance and can be calculated by knowing the blood viscosity μ, the length l and the diameter D of the vessel:

$$R_S = \frac{128\mu l}{\pi D^4} \tag{1.2}$$

- L_U is the vessel inertance which is dependent from geometric characteristics (cross section A, length l), as well as from the fluid density:

$$L_U = \frac{\rho l}{A} \tag{1.3}$$

- K_U and R_T are constant coefficients that are respectively equal to 1.2 and 0.95; K_V is a coefficient in function of Womersly number α and depends on the frequency of the heart rate:

$$\alpha = \frac{D}{2}\sqrt{\frac{2\pi f}{\rho}} \tag{1.4}$$

Thrombus formation is another problem when dealing with atherosclerosis. In fact, if the atherosclerotic plaque breaks up into small parts, in that same region there is the possibility

of forming a thrombus (an accumulation of platelets and fibrin). Consequently, this thrombus could break and, as a result, the fragments will form a clot that will obstruct the blood flow through the circulatory system.

1.3. Surgical intervention against coronary atherosclerosis

There are mainly two types of intervention for treating coronary atherosclerosis: the coronary artery bypass graft (CABG) and the percutaneous transluminal angioplasty (PTA). The former is a surgical procedure that consists into the deviation of the blood flow through a substitute path; the latter is a surgical procedure that aims at restoring the correct functionality of the coronary artery affected by atherosclerosis avoiding the deviation of blood flow.

1.3.1. Coronary Artery Bypass Graft (CABG)

CABG is a type of surgery that improves the blood flow to the heart. During CABG, a healthy artery or vein from the body is connected or grafted to the blocked coronary. The grafted artery or vein bypasses the vessel affected by stenosis creating a new path for oxygen-rich blood to flow to the heart (Figure 1.4). During surgery, the proximal extremity of the graft is anastomosed to the healthy artery in the upstream of the stenosis, and the distal extremity is connected downstream.
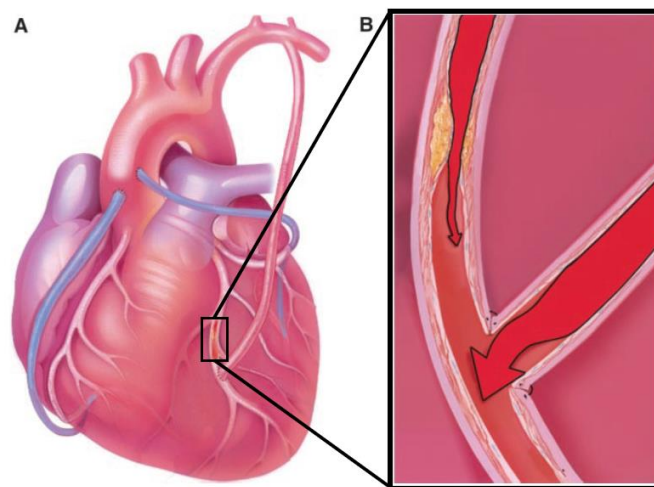

Figure 1.4 A) A coronary artery bypass graft (CABG). The cardiac surgeon can use a vein removed from the leg or an artery from the chest (mammary artery) to provide a new path for the blood flow from the aorta to the heart muscle. B) Zoom on the region downstream of the bypass. Image taken from [27].

Typically, the most commonly used vessels for bypass are the saphenous vein from the leg, the internal mammary artery from the chest, and the radial artery from the arm [1]. In case the vessel is the mammary artery (Figure 1.4A, *the red vessel*), only its distal extremity is anastomosed to the downstream of the stenosis while the proximal extremity is maintained in its location. When saphenous vein is used (Figure 1.4, *the blue vessel*), it is completely transferred from its original site to the heart connecting its proximal part to the aorta and the distal extremity to the valley of the stenosis.

Patients who undergo CABG treatment usually are subjected to a multiple sessions of bypass, from one to five follow-up interventions [21]. This kind of strategy implies a major disadvantage in terms of invasiveness. In fact, during the surgery patient's heart is temporarily stopped and an extra-corporeal circulation of the blood is used to perfuse the organism. Generally, for this intervention, one week in hospital and a time of recovery that lasts a few months are required [1]. Recently, surgical strategies that are less invasive have been developed, i.e. minimally invasive cardiac surgery (MICS) that allows the intervention even when the heart is still beating. The main advantage of MICS is the lower blood loss, reduced post-operative discomfort, faster healing times and lower risk of infections, as well as avoiding the possibility of deep sternal wound infection or sternal non-union [28].

1.3.2. Percutaneous transluminal angioplasty (PTA)

PTA was first performed in 1977 [29]. Initially, the angioplasty was conducted without stent deployment, a technique that is now referred as plain old balloon angioplasty (POBA).

The procedure can be summarized with these steps [21]:

i. The deflated balloon is inserted in the systemic circulation through a peripheral artery (typically the femoral or the radial artery) and, with the aid of radiographic imaging for better visualization (Figure 1.5A), it is pushed up to the occluded site (Figure 1.5B).

ii. After reaching the occluded site, the balloon is inflated. Such maneuver compresses the atherosclerotic plaque against the vascular wall (Figure 1.5C).

iii. Finally, the balloon is deflated, and the catheter removed, restoring the patency of the coronary artery (Figure 1.5D).
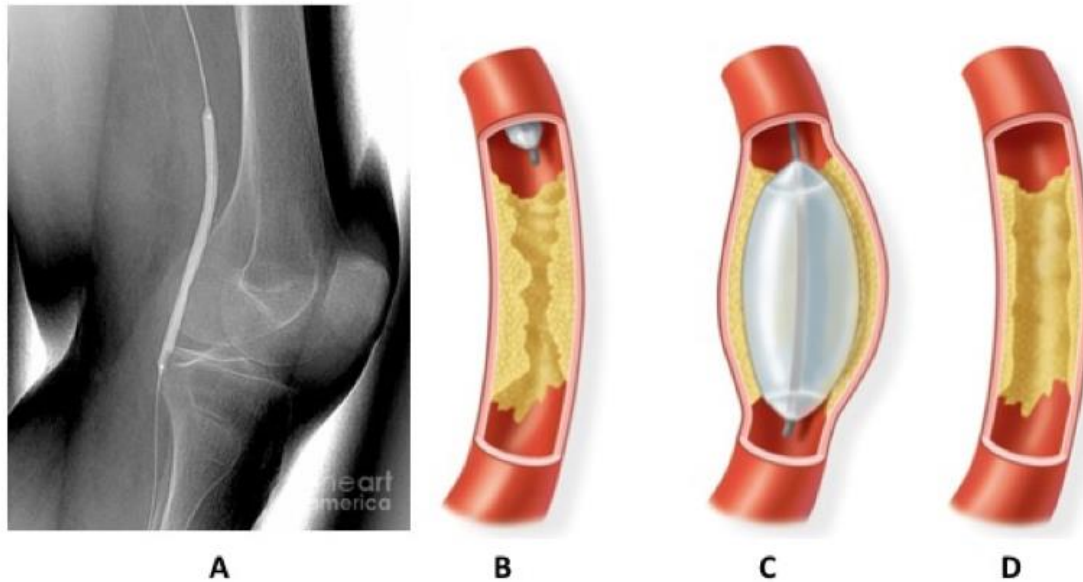
Figure 1.5 POBA procedure. A) Angiogram of the leg of a 69-year-old patient undergoing balloon angioplasty. B) The catheter, with the deflated balloon, is inserted through the leg. C) After reaching the stenotic site in the heart's coronary artery, the balloon is inflated pushing the atherosclerotic plaque against the coronary wall, leaving the coronary (D) open and unobstructed.

POBA certainly revolutionized the treatment of CD. However, the outcomes were compromised by re-narrowing of coronary arteries due to acute vessel closure because of: elastic recoil, late vascular remodeling and neointimal proliferation. In 5-10% of the patients elastic recoil has been observed in the immediate follow up, leading to a rebound occlusion of the artery and often to severe complications such as myocardial infarction causing emergency re-intervention using CABG [29].

Angioplasty induced endothelial cells denudation and medial tearing, also exposed circulating blood cells to the sub-endothelial matrix, leading to platelet aggregation and thrombosis, and hence, contributing to acute closure of the artery. Balloon application also induces medial smooth muscle necrosis. Consequently, a phase of coordinated proliferation of vascular smooth muscle cells (VSMC) is activated; VSMC migrates into the intima in response to the release of chemo-attractants such as the platelet-derived growth factor [30]. This neointimal proliferation leads to post-angioplasty restenosis.

Coronary stents were, therefore, developed to overcome these issues, by scaffolding the balloon-dilated artery, sealing the dissection flaps and preventing late recoil. Nowadays, most PTA procedures involves balloon angioplasty and stent deployment.

1.3.3. Angioplasty with stent deployment

One way to decrease the insurgence of restenosis is combining balloon angioplasty with stent deployment. In the mid-1980's coronary stents were developed and since then have seen a major refinements in design and composition [31]. Stents are small wire-mesh (a sample is shown in Figure 1.6) tubes that provide scaffolding to support the damaged arterial wall, reducing the chance that the vessel will re-close again after angioplasty [1].

Stents are made in a biocompatible material to reduce cells' uncontrolled reaction against foreign body. They are also well sensitive to x-ray imaging for good visibility during the intervention. In addition to these properties, stents must have good characteristics against mechanical stresses to avoid any vascular collapsing.

Typically stents are made of stainless steel (AISI 316L), Cr-Co alloy, tantalum and super-elastic alloy Ni-Ti (Nitinol) [17]; these type of stents are related to the family of bare metal stents (BMS). In recent years, it has been observed that polymeric stents are also a viable solution for angioplasty surgery and eventually are destined to replace conventional metallic devices in the coming years [32]. The main advantage is the possibility of not implanting a permanent metal prosthesis. In fact, polymeric stents are also known as bioresorbable stents (BRS) since they dissolve completely in the biological tissue avoiding problems related to formation of thrombi and in-stent restenosis (ISR). Restenosis, which is the main problem in BMS, is caused by the presence of the stent that induces local variation of the fluid dynamics of the blood flow (*explained in 1.3.4*). Most BMS are made of polylactic acid, a naturally dissolvable material also used in dissolving sutures. The drawbacks of using polymer are the following: recoil action after the expansion, stent thickness causing maneuverability and crossing issues, difficulty visualizing of a non-metallic material on fluoroscopy and stents not crimping firmly on delivery balloons [32].
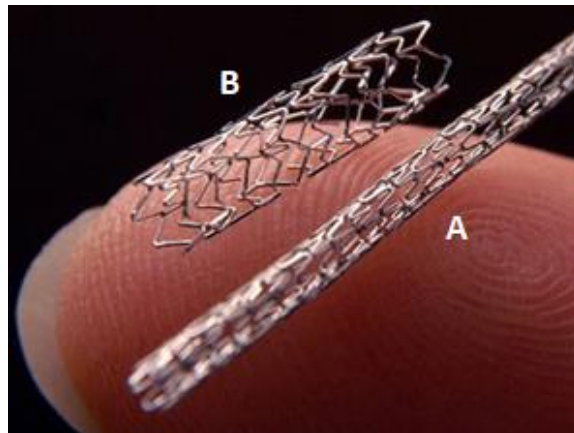
Figure 1.6 Digital photographs showing a metallic stent in (A) crimped and (B) expanded form. Image taken from [18]*.*

Stent deployment with balloon angioplasty was introduced in 1986 [17] and it is a similar procedure to the previously described POBA, differing only for having a stent in a crimped form around the balloon. After reaching the stenotic site and after the deflation of the balloon, the stent is left adherent to the wall to prevent its collapsing following the surgery (shown in Figure 1.7).

It has been observed [33] that stent deployment in angioplasty surgery decreases the risk of stenosis and for this reason it is the most utilized therapy for CD treatment. Despite the reduction of risk compared to the classical balloon angioplasty, there is still a major problem caused by in-stent restenosis (ISR). One solution that could contribute into the decrease of restenosis is the introduction of drug eluting stent (DES) that is able to inhibit the elements that are responsible for causing such phenomenon.
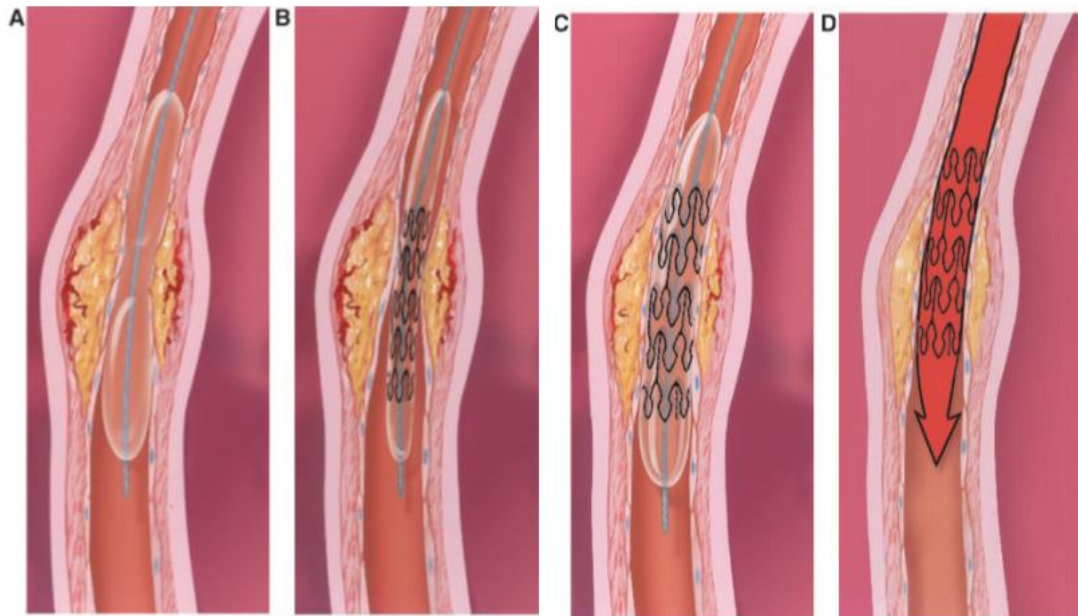
Figure 1.7 Balloon angioplasty and stenting. (A) A balloon-tipped catheter is positioned in the narrowed coronary artery and inflated. Similarly, in (B) is inserted together with the balloon in the stenotic site. The balloon inflation (C) causes the stent to expand and adhere to the artery walls. Finally, (D) the balloon is deflated and took out leaving the stent scaffolding the vessel. Image taken from [1].

1.3.4. In-Stent restenosis and thrombi formation

In-stent restenosis is the re-occlusion of a vessel that has been previously treated with angioplasty with stent deployment [33]. Such re-occlusion is caused partially by the elastic recoil of the atherosclerotic plaque that was initially compressed by the balloon; and partially by fluid dynamic alterations between the blood flow and the artery walls. The latter is due to the induced direct contact between the blood and the vascular smooth muscle cells of the tunica media as a result from the angioplasty surgery [34]. The VSMC tend to proliferate causing intimal hyperplasia and fibrosis. In addition to this, platelets aggregation and clotting activation causing the formation of thrombi is also possible due to endothelial disruption during the stent deposition or the balloon inflation.

DES could decrease ISR by releasing substances that can attenuate the VSMC proliferation, although it has some drawbacks in terms of generating thrombi due to delayed reendothelialization by the anti-restenotic drugs or delayed hypersensitivity reaction to the stent's material (metallic/polymeric) [29]. This whole process is described in Figure 1.8 and in addition to the previously mentioned reason regarding thrombi formation and ISR, it must be considered as well as other factors such as vascular inflammation due to strange body reactions, which could increase even more the VSMC proliferation and platelet-clotting activation together with an inadequate stenting during the surgery procedure and other systemic risk factors.

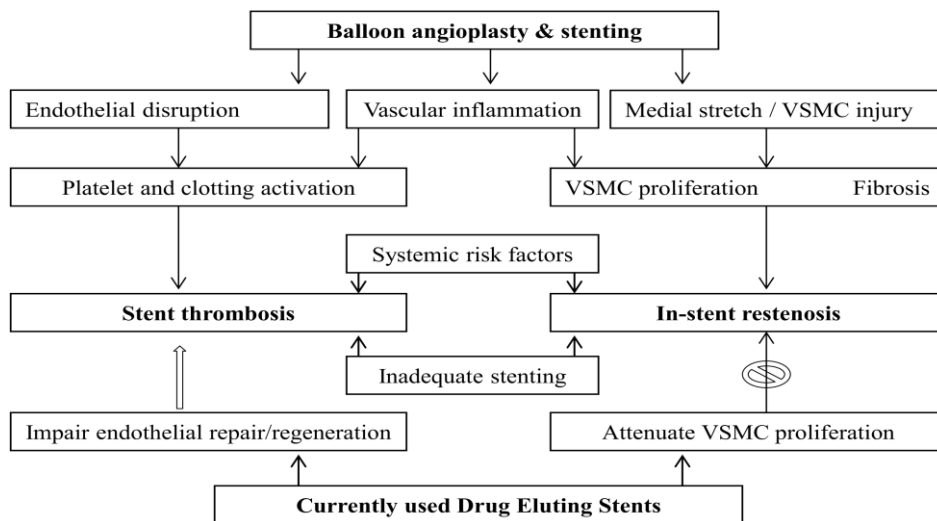*Figure 1.8 Pathophysiological impact of angioplasty, stenting and drug-eluting stents. Angioplasty and stenting induce injury to the vessel wall, which can activate several pathways promoting smooth muscle cells' proliferation and in-stent restenosis. Drug eluting stents, although attenuates restenosis, may also impair endothelial healing, making them prone to stent thrombosis. Image taken from* [29]*.*

In classic balloon angioplasty, typically, restenosis occurs in 40-50% of treated patients after a few months from the intervention [33]. In angioplasty with stent deployment, restenosis incidence rate is reduced, 25% and 10% respectively for classic stent and DES since the intima elastic recoil is blocked by the presence of the stent.

ISR after the scaffold implantation can be subdivided in function of time in four phases [34], [35] (as described in Figure 1.9):

i.   Thrombosis

This phase characterizes the first 3 days after the stent deployment. It is due to the damage that the stent causes to the walls which activates the platelets in the blood. Thrombus deposition is proportional to the structural damage but in general, it doesn't cause a significative reduction of the vascular lumen.

ii.   Inflammatory response

After platelet deposition, follows the inflammatory response in which the surface adherent monocytes (SAM) adhere to the lumen and to the stent. These monocytes move to the intima where they transform to macrophages (tissue infiltrating monocytes, TIM) and try to engulf the stent mesh. After failing the attempt, they aggregate forming polymorphonucleate cells that will lay around the scaffold. This process occurs mainly during the first week after the implantation.

iii.   Cells proliferation

In this phase monocytes starts to proliferate causing the release of substances that attract vascular smooth muscle cells. VSMC produce collagen fiber because of wall damage and altered blood flow in the peri-stent region. Such process is called neointimal hyperplasia.

iv.   Remodeling

Weeks after the implantation of the stent, the artery wall is remodeled due to collagen fiber deposition. In most of the cases, stent can stop the elastic recoil of the artery wall but not the remodeling phenomenon since the fibrotic tissue could infiltrate through the stent's mesh covering it completely.

The identification of ISR and thrombi formation is an important task and usually physicians are assisted by medical imaging techniques that provide crucial information about the

coronary-stent structure. Anticipating such pathologies is fundamental to avoid late post-surgical complications, but to achieve this goal, the phenomenon must be fully understood. One aspect that is under investigation is the interaction that fluid dynamics has on the development of restenosis and thrombosis. To perform such investigation, coronary-stent complex must be reconstructed in laboratory to obtain models. The reason is that, although nowadays imaging technology provides high detailed and complex images, for this field, basing the analysis on them only could not be enough (more details in the next chapter).
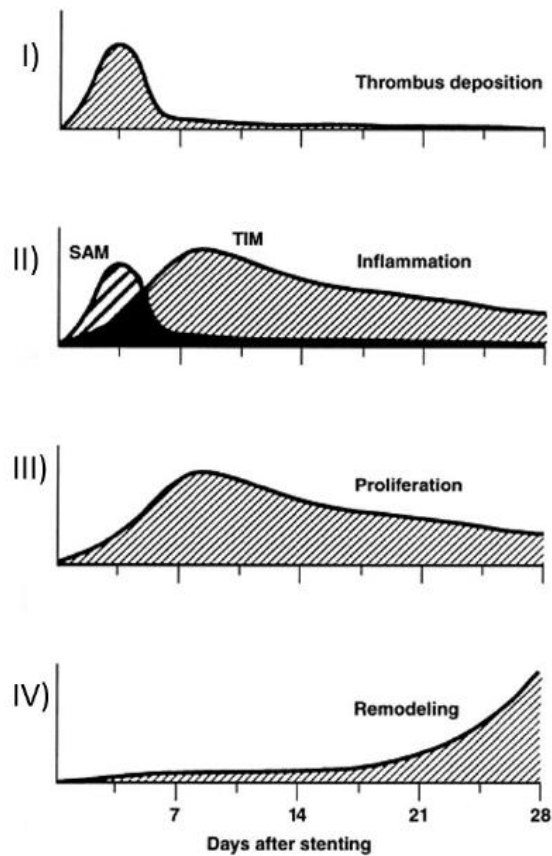
Figure 1.9 In-stent restenosis phases in function of time. I) Thrombus deposition during thrombosis. II) Inflammatory response phase monocyte deposition and infiltration. III) Monocyte and VSMC proliferation. IV) Remodeling phase with collagen fiber deposition [35].

2.

Imaging and stent reconstruction

In this chapter, a review of intravascular imaging techniques is presented. The use of IVOCT will be discussed focusing on the working principles and the advantages of this technique with respect to the others. The last part of the chapter is related to issues regarding 3D stent geometry reconstruction, which is the main topic of this thesis, focusing onto the differences that the proposed method has with respect to the algorithms already available in literature.

2.1. X-ray Angiography

Classical X-ray angiography is the most used imaging technique in assessing CD. It is based on the possibility of visualizing the blood flow thanks to the injection of a contrast enhancement fluid that is distinguishable from the background when the patient is exposed to X-rays. The fluid is injected through a catheter which is inserted in a peripheral artery (radial or femoral) and is pushed up to the region of interest. By using X-rays, it is possible to obtain 2D images that allow to identify pathological situations such as stenosis. In the image, stenosis is represented by a narrowing of the cross-section in which the contrast enhancement fluid flows (as shown in the sample image in Figure 2.1).

Although conventional angiography is the most used imaging technique in CD assessment, it has some drawbacks: i) the necessity of exposing the patient to X-rays; ii) the invasiveness of using a catheter; iii) the limited spatial resolution (100-200 μm); iv) the inability to give any details about the atherosclerotic plaque.

Figure 2.1 Conventional angiography showing the presence of stenosis (between the arrows) in the left anterior descending coronary artery. Image taken from [36]*.*

2.2. Intravascular ultrasound (IVUS)

IVUS, like conventional angiography, is an invasive imaging technique. It is based on the insertion of a catheter with a sound emitter at its extremity. At the beginning of the process, the catheter is positioned in the distal part of the vessel and then pulled backward with a fixed velocity, mapping tomographic images of the artery. The sound wave travels into the artery walls and is reflected or backscattered from the internal structures that have different acoustic properties. The frequency of the sound determines the image resolution, with higher frequencies yielding higher space resolutions. The time behavior or echo of the reflected sound is detected by the same inserted device and the ranges and dimensions of internal structures determined from the echo delay. Based on these echo delays, 2D images of the vessel are generated (example of a section image is in Figure 2.2). Sound waves have high penetrability in the artery walls and with IVUS technique it is possible to distinguish the layers (tunica intima, tunica media and tunica adventitia). Unlike X-ray angiography, IVUS can characterize the atherosclerotic plaque and it enables the assessment of the presence of elements such as lipid and calcium deposits as well as fibrous tissues [37], [38].

The major drawback of IVUS is the space resolution (around 100 μm) which, similarly to conventional angiography [38], limits the image quality.
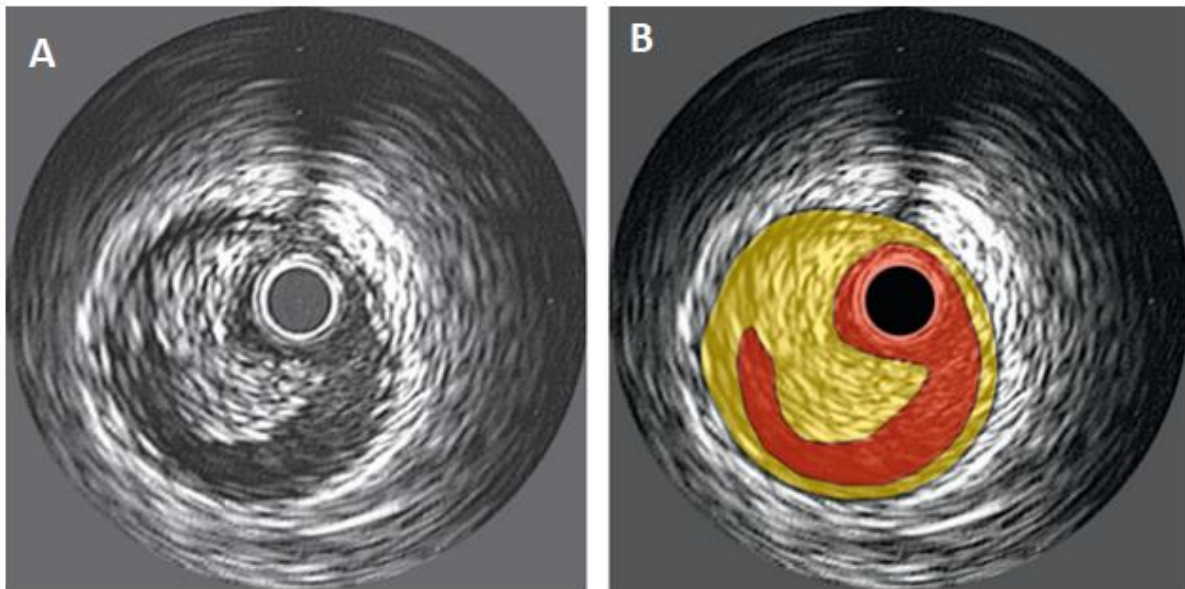

Figure 2.2 A) Intravascular ultrasound image of a coronary section with presence of atherosclerotic plaque. B) Same image with highlighted lumen (red) and plaque (yellow). The picture is taken from [39].

2.3. Intravascular optical coherence tomography (IVOCT)

IVOCT imaging is analogous to IVUS, except that it uses infra-red light instead of sound. IVOCT can provide cross-sectional images of the stent and has a better resolution than IVUS (10-20 μm in IVOCT vs 100-200 μm in IVUS). Optical coherence tomography (OCT) was introduced in 1991 [40]. At first, it was used mainly for the imaging of the eye. More recently, it grew in popularity among the intravascular imaging techniques. IVOCT's working principle is the same as for the IVUS: a catheter with the light emitter is inserted in the coronary artery; the light traverses the surrounding tissues and it is backscattered from structures with different optical properties [41]. IVOCT images allow better characterization of the atherosclerotic plaque, giving the possibility to differentiate between the layers of tissues and assessing the presence of calcium depositions. IVOCT also enables the possibility to identify the stent implant (a sample of a cross-section from IVOCT scan is shown in Figure 2.3). In addition, the IVOCT acquisition process gives the possibility to acquire images *in-situ* and in real time.

One of the drawbacks of IVOCT, besides to the invasiveness of its procedure, is that, since light is highly scattered by most biologic tissues, optical scattering limits image penetration depths to 2-3 mm [41] whereas for IVUS is about 10 mm [4]. Consequently, for IVOCT, the external layers of the vessel are hard to represent in the image. Moreover, IVOCT imaging is not suitable for vessels with diameter greater than 10 mm [4].
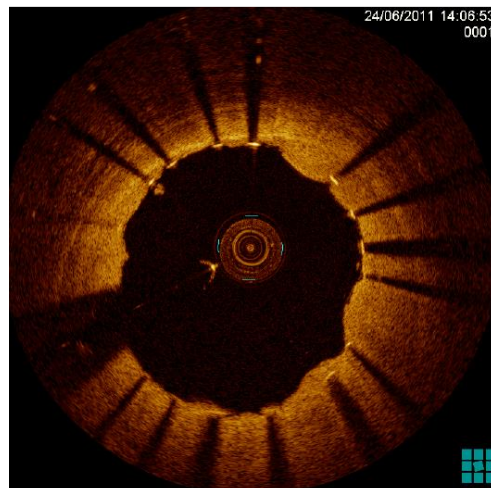

Figure 2.3 Cross-section image of a vessel acquired through IVOCT imaging. Stent's strut is clearly visible thanks to the high spatial resolution capability of IVOCT, enabling the assessment of stent's malappostion. Stents in the figure are identifiable as high brightness area followed by shadow lines. Image taken from [5].

2.3.1. OCT working principle

OCT image acquisition instrument exploits a Michelson's interferometer (Figure 2.4). A Michelson's interferometer is a device in which an infrared light is emitted from a source to a beam splitter. One of the beams is incident onto the sample to be imaged, while the second beam travels a reference path with variable path length and time delay. The backscattered light from the sample is interfered with the light reflected from the reference side and detected with a photodetector at the output of the interferometer. If the light source is coherent, then the interference fringes will be observed as the relative path are varied. In the Michelson interferometer, the light emitted from the source is a short pulse or has a low coherence. Consequently, interference of the light reflected from the sample and reference path can occur only when the two path lengths match to within the coherence length of the light. Imaging is based on the detection of the echo time delay and intensity backscattered light from the matter within the sample, and onto the demodulation of the interference output, while scanning the reference path length [41].
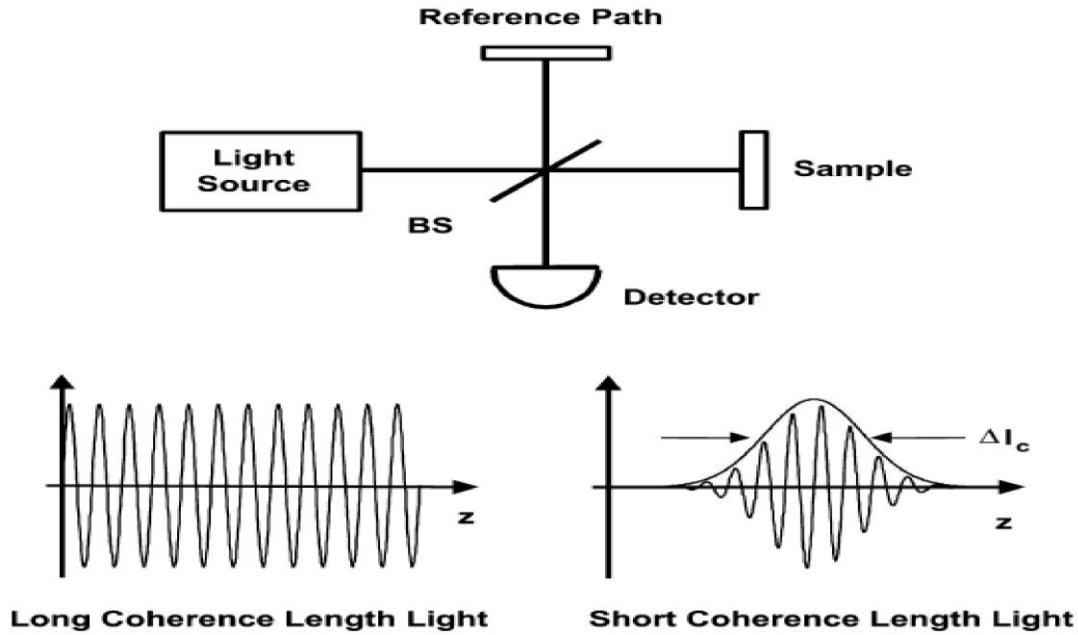
Figure 2.4 Michelson's interferometer. The short coherence infrared light is emitted by the source and sent to a beam splitter (BS). One beam travel to the sample and produces backscattered light from the matter along the path causing a series of echo with delayed time and intensity. These echoes are detected and demodulated at the interferometer output by scanning the reference path with different distance length. Image taken from [41].

The image that can be obtained by this acquisition process (A-scan) is a one-dimensional image (Figure 2.5A). Michelson's interferometer can be also used in intravascular imaging by integrating it into a rotating system mounted to the extremity of the catheter. By acquiring A-scans from different angles it is possible to obtain a complete mapping of the vessel's cross-section, also known as B-scan (Figure 2.5B). In this way, IVOCT can be used to build 3D models, by stacking B-scans of multiple cross-sections along the longitudinal direction, following the centerline of the vessel (Figure 2.5C).

An IVOCT acquisition system can be characterized by two resolutions: the axial and the lateral resolution. The former is the spacing along the radial direction and parallel to the A-scan, it is characterized by the wavelength of the infrared light and can be calculated from this formula [41]:

$$\Delta r = \frac{2 * ln2 * \lambda^2}{\Delta\lambda} \tag{2.1}$$

In the equation, λ is the central wavelength of the light source and $\Delta\lambda$ is half of the infrared emitted bandwidth. Typically, the wavelength is around 1300 nm and the axial resolution is around 10-20 μm.

The lateral resolution is in function of the depth of field f and of the diameter D of the emitted light, as shown in this formula [41]:

$$\Delta x = \frac{4 * \lambda * f}{\pi * D} \tag{2.2}$$

There is a relationship between the penetration depth of the light source and the lateral resolution: when the former increases, the latter decreases [41]. Therefore, on one hand IVOCT has a better lateral resolution with respect to IVUS (40 μm vs 200-300 μm [4]), conversely, IVOCT's penetration is worse than the one of IVUS (2 mm vs 10 mm [4]).
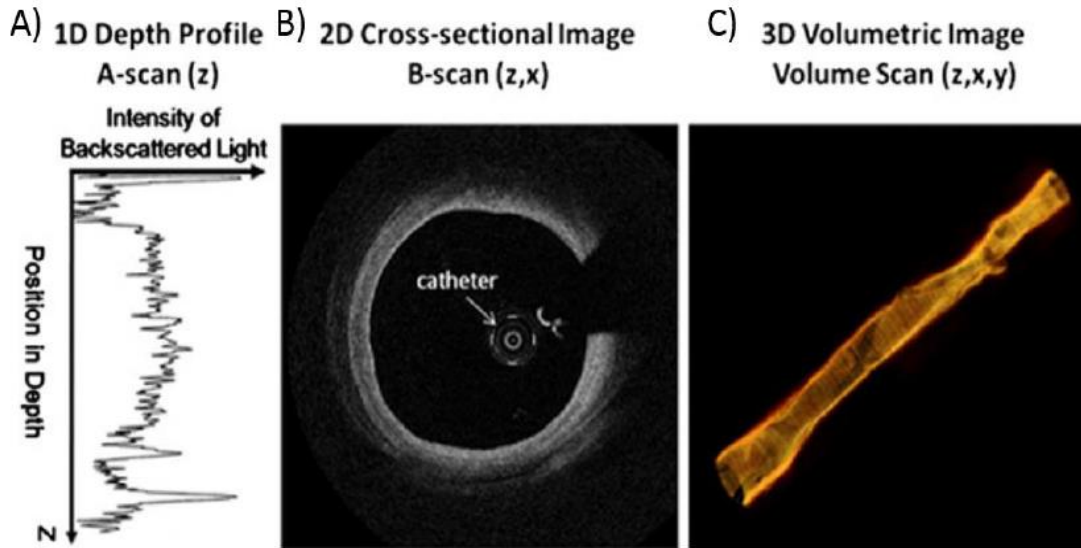
Figure 2.5 Three images representing the three scans. A) Sample of A-scan from IVOCT acquisition where the intensity of backscattered light detected by the sensor is in function of position in depth. B) 2D Cross-sectional image obtained by combining multiple A-scan resulting into a bi-dimensional image known as B-scan. C) A 3D model of the vessel obtained from stacking multiple B-scans. Image taken from [42]*.*

2.3.2. FDOCT vs TDOCT

OCT signal detection can be subdivided in two types: time domain optical coherence tomography (TD-OCT) and frequency domain optical coherence tomography (FD-OCT) [4], [43]. Table 2.1 shows the main characteristics of both techniques in comparison with IVUS. TD-OCT exploits a light from the source that has a wavelength between 1280-1350 nm [4]. In addition, TD-OCT uses a variable reference path of the light that goes to the reference mirror. Since interference occurs only when the difference between the distances travelled by the two lights is below the coherence distance [41], it is necessary to vary the distance from the mirror in order to characterize the tissues at different levels of depth. Since the acquisition must be done layer by layer, TD-OCT usually has a duration of acquisition greater than the FD-OCT. Conversely, FD-OCT enables the recording of an entire A-scan simultaneously [4], considerably reducing the time of acquisition. There are two types of FD-OCT: the spectral domain and the swept source [4]. The main difference with respect to TD-OCT is that the reference mirror in FD-OCT is maintained at a fixed distance. In the spectral domain, a spectrometer is placed before the photosensor to differentiate between the different wavelengths of the backscattered infrared light. Each of monochromatic wavelength hits a single pixel in the photosensor forming as a result the entire A-scan. In the swept source, there

is no presence of spectrometer. Instead, a very narrow bandwidth of light source with a variable frequency in function of time is used. Such narrowing of the light source enables the acquisition of all the pixels of the A-scan by analyzing the frequency characteristic of each backscattered light. As far as intravascular imaging technique is concerned, the most used technique between the two-frequency domain OCT is the swept source. On the other hand, the spectral domain FD-OCT, is mostly used in the ophthalmology field [4]. An illustration of the described OCT acquisition modalities is shown in Figure 2.6.

Table 2.1 Main characteristics of the three types of intravascular imaging: TD-OCT, FD-OCT, IVUS [4], [44].

	TD-OCT	**FD-OCT**	**IVUS**
Energy source	Infrared	Infrared	Ultrasound
Wavelength	1.3 µm	1.3 µm	35-80 µm
Axial resolution	15-20 µm	10-20 µm	100-200 µm
Lateral resolution	90 µm	20-40 µm	150-300 µm
Sampling frequency	15-20 Hz	100 Hz	30 Hz
Catheter pullback speed	1-3 mm/s	2 cm/s	0.5-1 mm/s
Scanning diameter	7 mm	10 mm	15 mm
Penetration depth	1.5-2 mm	1-2 mm	10 mm
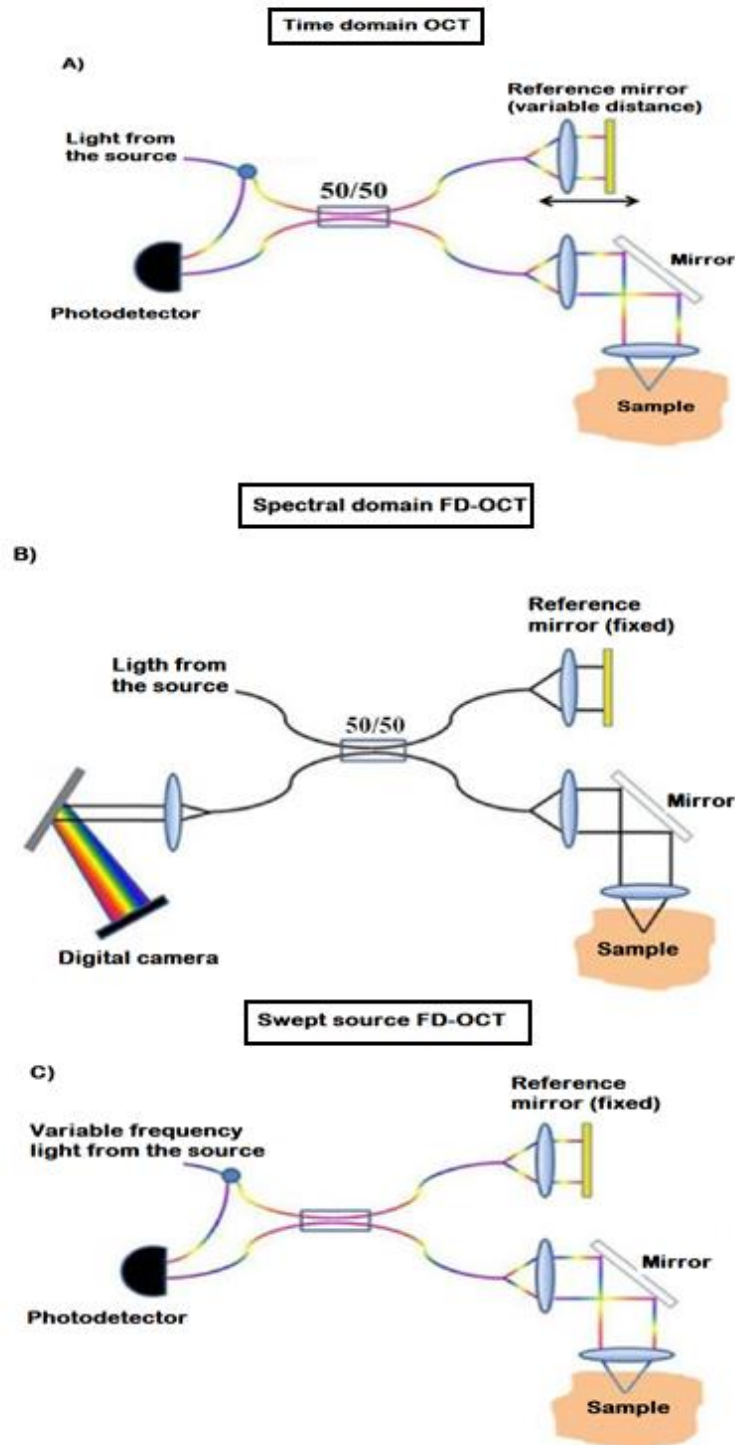
Figure 2.6 Image representing the three types of acquisition modality in OCT imaging. A) In the TD- OCT, the reference mirror is varied in distance to record information about the sample layer by layer at different level of depth. B) In the spectral domain FD-OCT the backscattered infrared light goes through a spectrometer where the wavelengths are separated before hitting the sensor. C) In the swept source FD-OCT, the frequency variable light emitted from the source is analyzed in frequency domain to obtain a multi-layer mapping of the sample. Schematic image taken from [42].

2.3.3. In vivo acquisition techniques

IVOCT uses a fiber optic device to scan and acquire information about the surrounding tissues. Such device is introduced in the artery through an intravascular catheter, usually far from the stenotic zone (femoral or radial vena). After reaching the point of interest, by using an electric motor, a pullback and rotational motion of the catheter is applied. Such process enables the acquisition of multiple A-scans around 360 degrees and as a result, a series of cross-sectional images of the vessel is obtained.

One fundamental drawback of IVOCT imaging *in-vivo* is that, infrared light is usually reflected by the heavier elements of the blood (e.g. red cells). To avoid this problem, two possible procedures are used [42], [45]:

i.   Occlusive technique

This procedure is usually applied for TD-OCT and it requires the stopping of the coronary blood flow by inserting and inflating a balloon. To guarantee a continuous flow of the vital nutrition to the heart, avoiding in this way the damaging of the myocardium, the balloon is equipped with a system that supplies a colloidal solution. Such use of a blood substitute, in a long period of application, could cause ischemia. For this reason, the occlusive technique can last only for a few seconds. In addition to this, there is also the possibility that the balloon could damage the lumen's wall.

ii.   Non-occlusive technique

This procedure removes the red cells by injecting a high viscosity liquid. It is usually applied for FD-OCT. The major drawback of this technique is that, if used excessively, it could cause kidneys failure [46].

2.3.4. Utility of IVOCT

IVOCT is useful for multiple reasons in assessing the status of CD. Some of the main information obtainable from IVOCT imaging are listed below:

i.   <u>Assessing the correct positioning of the stent</u>

IVOCT, like IVUS, can give important information about the stent's correct positioning with respect to the vessel's walls. The better resolution of IVOCT makes it the best choice for this type of analysis. In fact, from IVOCT it is possible to extract not only qualitative data about the stent malapposition (Figure 2.7) but also to quantitively evaluate the error. Such information is useful in clinical practice, e.g. for surgeons during follow-up intervention to know whether to re-expand the stent. Additionally, IVOCT images can be used for better analysis of the relationship between the wrong positioning of the stent and post-implant phenomenon such as ISR.

ii.   <u>Assessing the vessel's walls response to the stent implant</u>

After stent implant, IVOCT images can show the presence of thrombi, tissue ruptures and tissue prolapse (Figure 2.8). These information helps to assess the acute inflammatory response to stenting as well as long-term phenomenon such as ISR (Figure 2.9). By characterizing the vessel's lumen and the stent's post-implant position (or after follow-up intervention), it is possible to evaluate the entity of the ISR.

iii.   <u>Coronary-stent complex fluid-dynamic analysis</u>

From IVOCT images it is possible to build 3D models of the coronary-stent complex. Such 3D models can be used for fluid-dynamic simulations which in turn can give detailed information regarding local distributions and variations of a variable such as shear stress. The evaluation of this physical quantity enables the assessment of the locations where there is a potential arising of stenosis or thrombosis.
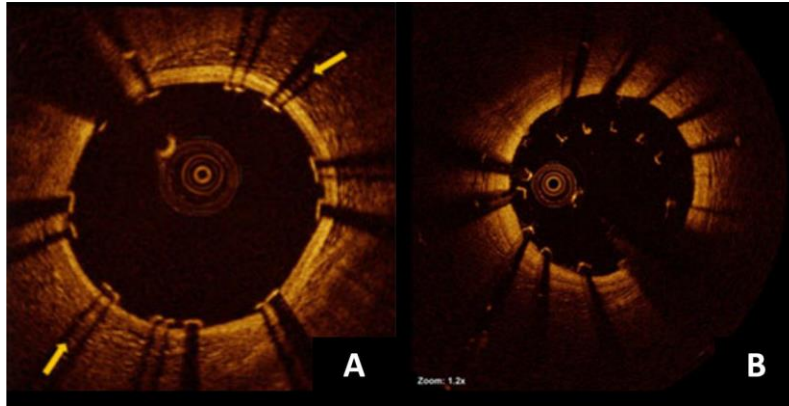
Figure 2.7 Two images of coronary-stent cross-section. A) Cross-section of a good stent positioning; stent struts are recognizable by the shadow line along the radial direction (indicated with arrows). B) Cross-section of stent malapposition. Image taken from [47].
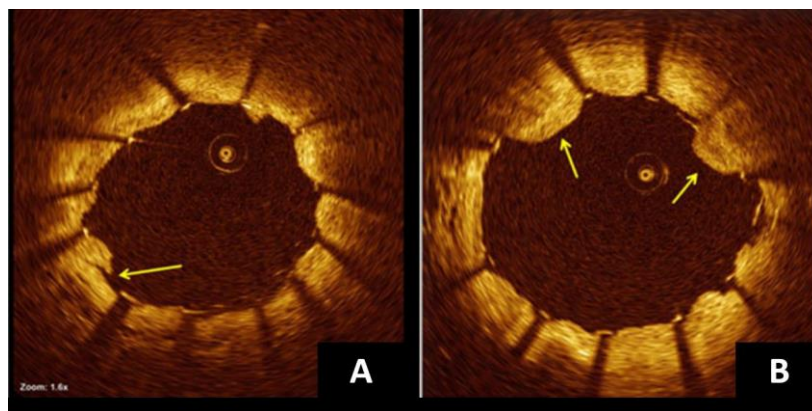
Figure 2.8 Two images representing the vascular damages after stent implant. A) Vascular walls lesions (indicated by the arrow). B) Tissue prolapse in-between the struts of the stent (indicated by the arrows). Image taken from [47].
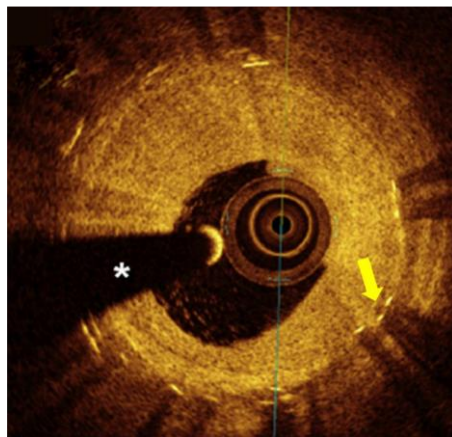
Figure 2.9 Sample of ISR with stent struts still visible, although covered with fibrotic tissue and indicated by the arrow. Image taken from [47].

2.4. Stent reconstruction algorithms from IVOCT

IVOCT imaging is a new methodology in assessing CD and therefore is not a very diffuse procedure in clinical field. There are only few studies in literature that proposed methods for reconstructing the *in-vivo* stent implant from OCT scans. The gold standard for intravascular reconstruction is the IVUS in combination with other imaging technique such as angiography or CT. The better resolution of IVOCT images makes it the best choice in intravascular imaging in the future.

IVOCT scans provide 2D images that could already give information about the disease. In fact, from 2D IVOCT images, the fibrotic tissue depositions and the narrowing of the lumen as well as the wrong positioning of the stent are detectable. One of the reasons to reconstruct the stent *in-vivo* comes from the possibility of performing computational fluid dynamics (CFD) analyses onto the 3D reconstructed model. Such studies will give a better understanding of the ISR phenomenon, which has been demonstrated to be affected by the alteration of the wall shear stress (WSS) induced by the presence of the stent [2]. These analyses could be useful from the clinical point of view. In fact, wrong stent positioning is the main cause of the fluid-dynamics alteration. Patient-specific 3D stent reconstruction is a useful way of providing clinicians new instruments to predict ISR due to stent post-implant malapposition.

The segmentation of the IVOCT images brings to the identification of the lumen and the stent. The contour of the lumen can be obtained in different ways. Often, the lumen is identified in polar coordinates, typically with edge detection algorithms, followed by a gap filling phase, necessary because of the guide wire shadow artifacts that make part of the wall invisible (as shown in Figure 2.9), and a smoothing process [2]. As for the stent, the process consists of a manual or semi-automatic identification of the struts that, in the IVOCT images, represent the stent's cross-section. For example, in Migliori et al. [2], after converting the frames in polar coordinates, the struts are identified exploiting the peculiar characteristic of OCT images, where the stents struts appear as high reflecting elements followed by a trailing shadow (Figure 2.7). A first set of candidate struts are identified in the A-scans. The line connecting the candidate pixel (high intensity with high peak) with the thirtieth low intensity pixel must have a sufficiently high slope, meaning that that pixel is isolated, in terms of intensity, with respect to its neighbor. Subsequently, a fuzzy logic approach is applied to identify strut pixel and delete false positives. The images are then converted back to Cartesian coordinates. The detected stent and lumen are aligned and oriented, following the centerline of the artery phantom that was extracted after micro-CT (µCT) scans (Figure 2.10*)*. Two cloud of points (COP) are then generated from this alignment: one for the lumen and one for the stent [2].

From the COP of the stent, the 3D stent geometry is reconstructed using a morphing procedure, in which the centerline of a free expanded stent (extracted from μCT slices) is morphed into the deployed stent configuration. The handles for morphing are created on the centerline and move to points that belong to the COP minimizing their distances. Finally, the stent geometry is obtained by positioning cross-section curves on each ring (Figure 2.11) [2].
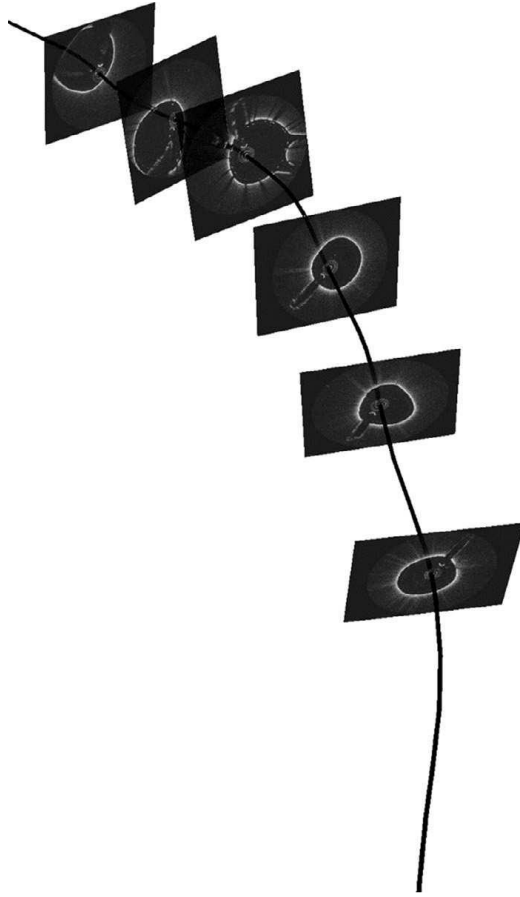

Figure 2.10 Alignment of intravascular optical coherence tomography frames with the centerline of the main branch that was acquired through micro-computed tomography scan. Image taken from [2].
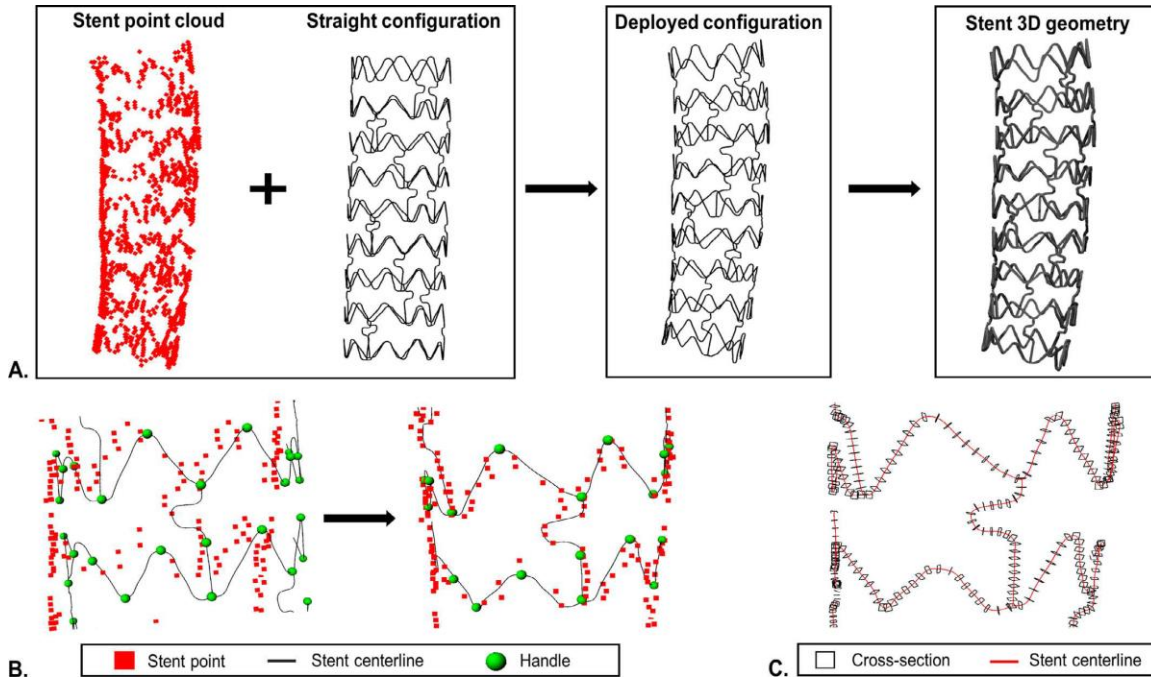
Figure 2.11 Step by step scheme of Migliori et al. [2] *3D stent geometry reconstruction. A) The COP of the stent (obtained from optical coherence tomography scans) and the straight configuration of the centerline (obtained from micro-computed tomography) are used to generate deployed configuration of the centerline and the stent 3D geometry. B) Morphing of the stent centerline using the handles so that their distances with the selected stent are minimized. C) Curve loft of the stent strut cross-sections along the morphed stent centerline. Image taken from* [2].

Some author tried to reconstruct the stent 3D geometry without a prior stent design knowledge. In particular, in Ellwein et al. [6], the IVOCT scans are positioned orthogonally to a guide-wire pathway and smoothly connected to obtain the final lumen model. Such guide-wire pathway was obtained from a preliminary 3D vessel reconstruction from μCT scans. Subsequently, since the guide-wire adopts the straightest configuration inside a tortuous vessel, the shortest path algorithm to a graph representation of the artery was estimated. After reconstructing the lumen, an idealized model of a thick stent is drawn (matching the vessel geometry) and subtracted from the lumen model to generate the fluid domain for the CFD simulations.

Other authors [7]–[15] did not use idealized model of the stent. Conversely, the stented vessel geometry was generated directly from the IVOCT scans. Such method is resumed into these three steps: i) the lumen contour is delineated manually accounting also for the presence of the stent strut in each OCT frame; ii) the centroid of each stented lumen contour was calculated and used for placing the OCT frames orthogonally to a centerline that was generated from two angiographic projections; the orientation of the stented vessel is improved

by choosing the arterial side branches as landmarks in order to estimate the relative axial twist of the OCT frames; iii) the contours were connected with a non-uniform rational B-splines (NURBS) surface.

In O'Brien et al. works [16], like in Migliori et al. [2], the reconstruction is based on the prior definition of a 3D COP yielded from the segmentation of the OCT frames associated to *a-priori* known stent geometry. Since reconstruction with general interpolation of the points generated discontinuous stent structures, O'Brien et al. [16] computationally constrained interpolation to the known stent geometry fitted to the 3D COP as shown in Figure 2.12A. In this process, data registration is used to fit a dataset Y of points representing the stent skeleton to a COP (representing the detected struts from the OCT frames segmentation). Subsequently, surfaces were then built around the deformed skeleton using a swept cross-section to define the stent's mesh surface as described in Figure 2.12B.

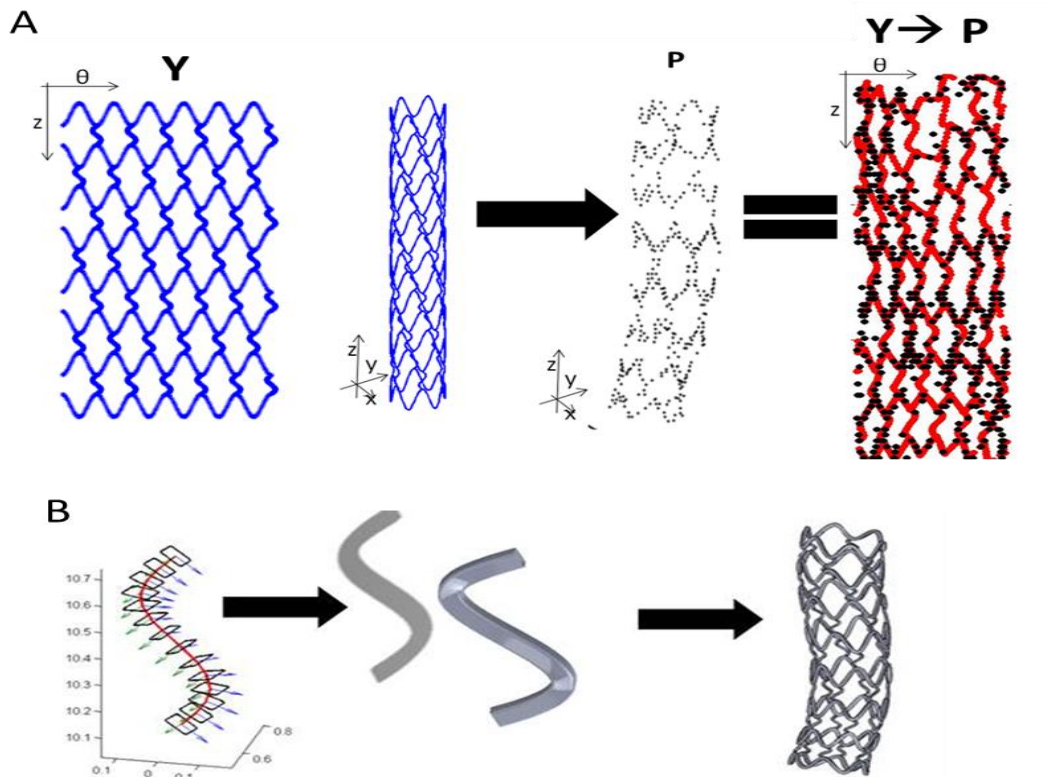*Figure 2.12 Scheme of 3D stent reconstruction from O'Brien et al [16]. A) An idealized dataset Y of points representing the stent structure registered to a cloud of points P representing the strut's points from the OCT frame segmentation resulting into a deformed structure of the stent. B) The stent surface is obtained by building around the deformed stent skeleton surfaces using a swept cross-section method.*

2.4.1. Stent reconstruction algorithm by image registration

In the previous section, some algorithms that reconstruct the *in-vivo* stent geometry from IVOCT frames for patient-specific characterization of the CD have been presented. In Ellwein et al. [6], the reconstruction is based on the use of a virtual stent that will be subtracted from the previously reconstructed lumen model. In this case, the modeling is based on an approximate geometry of the stent, where the global artery deformation prevails at the expense of a detailed representation of the stent, resulting in a difficult detection of malapposition.

In this thesis, a new method of patient-specific 3D stent reconstruction is proposed. It aims to give a better description of the *in-vivo* stent's mesh. Similarly to the methods of previously mentioned authors [2], [16], the stent geometry, before the implant, is known *a-priori*. The current method is based on image registration in which the stent in non-deformed configuration is mapped onto the *in-vivo* and deformed stent, whose 3D COP was obtained from the segmentation of the IVOCT frames. To proceed with the registration, the non-deformed model and the 3D COP must first be converted into images. In Migliori et al. [2], the stent in non-deformed configuration is morphed onto the 3D COP by manually creating the handles to the stent wire centerline, minimizing the distances between these and their corresponding points. Conversely, the current algorithm tries to partially automatize the process of stent geometry reconstruction by means of image registration where the non-deformed image from the ideal model is super-imposed and deformed with respect to the image from the 3D COP. The process of reconstruction tends to be faster compared to the methods proposed in literature since image registration, involves, in some of its parts, automatized procedures.

In several works [7]–[15], the coronary-stent complex contour for each frame, were defined and then connected using NURBS. This permitted to recreate the real and overall stent shape within the artery. However, the resulting geometries were corrugated and hardly continuous [3]. In O'Brien et al., B-Spline curves are used as interpolator during the registration of the stent in non-deformed configuration to the 3D COP. The final stent surface is then defined by stacking cross-sections of the stent model onto the resulting stent skeleton from the interpolation. In the current method, the registration is not applied on scattered points of data, but on voxels of 3D images with specific grey values. Using images instead of raw scattered data gives the possibility to optimize the registration process. In fact, image registration implies many types of transformations on the data which could facilitate the super-imposition and deformation of the non-deformed stent to the 3D COP image. This

significantly decreases the computational cost and the final 3D stent geometry model can be obtained in a shorter time compared to the previously mentioned methods. In the next chapter the concepts and the rules for registering 3D images will be explained more in detailed.

3.

An overview of the registration procedure in imaging

In this chapter, the general concepts of image registration are explained, followed by the discussion regarding the transformation model, the metrics and the optimization algorithms.

3.1. Introduction

Image registration is one of the fundamental procedures of image processing in the field of medical imaging. The main aim of this procedure is to achieve the best alignment between a fixed (reference) and a moving image (source).

Images are matched by adjusting the parameters of a geometrical transformation which map points in one image to the corresponding points in the other one [48]. This transformation typically does not lead to an absolute and perfect alignment between the two objects. Thus, image registration evolves to an optimization problem which maximizes the matching between the two. Consequently, geometric transformation model, similarity measure and optimization algorithm are the most significant component of image registration and, they need to be carefully determined depending on the nature of the problem.

The differences of the images to be registered and the multiple type of noise make the design of a universal method applicable to all the fusion tasks impossible. These diversities can be subdivided into four groups [49].

    i.   Different modality (multi-modal analysis): it is the case in which images, of the same body district, are acquired by different kind of techniques. The objective is to merge the information from different imaging procedures to gain more complex and detailed tissues representations [50].

    ii.   Different time (multi-temporal analysis): it is the case in which images are acquired during follow-up investigations of a patient. The aim is to detect and test the changes in the body district which appeared during consecutive image acquisition.

    iii.   Different viewpoints: it is the case in which the two images to overlap were acquired with dissimilar geometries.

    iv.   Scene model registration: the model can be a computer representation of the scene, for instance a priori knowledge of a specimen. The objective is to localize the acquired image in the scene or model and compare them.

To solve the problem of image registration, several strategies have been proposed; all of them required the definition of three main components [51], such as:

- Spatial transformation model that describes the way the source image can be deformed to match the target.
- The Metric, a similarity measure which resumes information of images match.
- The Optimization algorithm, that can vary the transformation model to find the best matching transformation.

3.2. Transformation model

Superimposing one image to another requires the determination of a geometrical transformation model; this is a spatial function that maps the N-dimensional space of the image to be registered to the space defined by the reference one. By considering *FS* as the floating space where the moving image is located and *TS* for the space of the reference one, a generic transform **T** applied to a point **p** ∈ *FS* produces a point **p'** ∈ *TS* by the general equation:

$$\boldsymbol{P}_{TS} = \ \boldsymbol{T}(\boldsymbol{P}_{FS})$$
(3.1)

Transformation **P**$_{TS}$ can be subdivided into two main classes: nonlinear transformation and linear transformation. Because of the non-linear nature of image acquisition systems and, sometimes, the deformable nature of the scene, the images to be registered often have non-linear geometric differences. Non-linear transformations map straight lines to curves [52] and allow for a more localized deformation. In some other cases, a linear transformation is applied, and it allows for a global change of scale and shear.

3.2.1. Linear transformations

Linear transformations on N-dimensional images are characterized by several spatial transformations such as translation, scaling, rotation, rigid and affine. The main characteristic of these classes of transformations is that they preserve the straightness of lines and parallelism and can be totally described by using up to (N+1) x N parameters.

3.2.2. Non-linear transformations

Non-linear transformations are those that do not preserve the straightness of the line during registration, and therefore can adapt to complex deformations between the images. They can be subdivided in two categories: physical based models and function representations [52]. The former is derived from the theory of continuum mechanics and fluid flow and it constrain the deformations to act in a physical manner; the latter considers basis function expansions, derived from interpolation and approximation theory, to model the deformation. Among the functions that are mostly used for non-linear transformations, there are the Thin Plate Splines and Basis Splines, which respectively can be considered to have a global and local support. In fact, basis splines transformations use control points (CP) in the source and the target and a spline function to define the correspondences, while thin-plate splines, conversely, use CP belonging to a *thin-plate*.

This definition of the CP of thin plate can be a disadvantage since it limits the ability of having complex and localized deformations and also, as the number of CP increases, the computational cost associated with moving a single point arises [51]. Basis spline transformations are spline function that have minimal support and the perturbation of one CP can affect only small part of the neighborhood of that CP.

One main disadvantage that can be found for both functions is that special measures are sometimes required to prevent folding of the deformation field, called regularization terms.

3.3.   The similarity measures

Feature patterns contained in each image are compared and match based on intensity based fusion procedures using mathematical or statistical criteria. They expect that a correct registration transformation corresponds to good similarity between the images. These approaches are mainly subdivided in two macro groups in relation to the kind of registration problem they solve: mono-modal and multi-modal. For example, in the mono-modal registration, the mean squared error (MSE) is the mostly used, while mutual information (MI) and normalized gradient field (NGF) are generally chosen for multi-modal image fusion.

3.3.1. MSE

MSE assumes ideally that two homologous points in the same scene have the same intensity value in both images, except for noise. It also be considered as a measure of fidelity or, conversely, the degree of distortion between two pixels in the same region of the two images. The required perfect equality in terms of intensity level implies the utilization of MSE only in mono-modal registration methods. MSE has two principal advantage: an easy implementation of the calculation, and consequently, the possibility of running it in parallel leading to a faster registration procedure. MSE is defined as:

$$MSE(X,Y) = \frac{1}{N}\sum_{i=1}^{N}(X_i - Y_i)^2 \tag{3.2}$$

where X_i and Y_i are the i-th pixel of image X and Y respectively, while N is the number of pixels considered.

3.3.2. MI

MI measures the content of information that a random variable (fixed image intensity) explains about another random variable (moving image intensity). MI has been shown to be robust in multi-modality image registration and does not depend on the dynamic range or intensity scaling of the images and complex mapping between the two images can be modeled [53]. MI can be defined in terms of entropy and joint entropy:

$$H(X) = -\int p_X(x)log(p_X(x)))dx \tag{3.3}$$

$$H(X,Y) = -\int p_{X,Y}(x,y)log(p_{X,Y}(x,y))dxdy \tag{3.4}$$

If X and Y are independent $p_{X,Y}$ can be obtained as:

$$p_{X,Y}(x,y) = p_X(x) \cdot p_Y(y) \tag{3.5}$$

And therefore

$$H(X,Y) = H(X) + H(Y) \qquad (3.6)$$

if there's dependency between X and Y then

$$H(X,Y) < H(X) + H(Y) \qquad (3.7)$$

MI can be computed as:

$$MI(X,Y) = H(X) + H(Y) - H(X,Y) \qquad (3.8)$$

MI implementation

Viola and Wells [50] implemented MI using two separate intensity samples, S and R: the first to compute the density and the second approximate the entropy as sample mean:

$$H(X) = \frac{1}{N} \sum_{r_j \in S} log(P * (r_j)) \qquad (3.9)$$

Where $P * (r_j)$ is the probability densities of pixels values of sample $r_j \in S$.

Mattes MI implementation [54], [55], differently from Viola and Well's implementation, uses only one set of intensity samples drawn from the image, and the marginal and the joint probability density function (PDF) are evaluated at discrete positions or bins uniformly spread within the dynamic range of the images. Entropy values are then computed by summing over the bins. This results in a reduced computation time.

3.3.3. **Normalized mutual information (NMI)**

Normalized Mutual Information is a version of MI which is invariant to the size of the field of view of the images [56]. It is computed as:

$$NMI(X,Y) = 1 + \frac{MI(X,Y)}{H(X,Y)} = \frac{H(X) + H(Y)}{H(X,Y)} \qquad (3.10)$$

where $H(X)$ and $H(Y)$ are the entropy of the images, and $H(X,Y)$ is the joint entropy.

3.3.4. **NGF**

In the normalized gradient field (NGF) metric it is assumed that two images are similar if intensity changes occur at the same locations. These intensity variations can be detected by calculating the image gradient in all the three directions [57]. The magnitude of these changes might be related to the imaging device; therefore, a normalization of the gradient field must be considered. To minimize this effect the NGF of an image X in a coordinate space $s \in \mathbb{R}^d$ is calculated as:

$$N_\epsilon(X,s) = \frac{\nabla X(s)}{\|\nabla X(s)\|_\epsilon} \qquad (3.11)$$

Where this norm is defined as:

$$\|S\|_\epsilon = \sqrt{\sum_{l=1}^{d} s_l^2 + \epsilon^2} \qquad (3.12)$$

$$\epsilon = \frac{\eta}{N} \int_\Omega \|\nabla X(s)\| \, d(s) \qquad (3.13)$$

In order to use the NGF as a similarity measure (F_{NGF}) for two related points p in the reference image ($X_R(p)$) and in the source image ($X_S(T(s,\mu))$), the relationship between $N_\epsilon(X_R,s)$ and $N_\epsilon(X_S(T(s,\mu)))$ must be analyzed. For example, these two vectors form an angle $\theta(x)$,

therefore, it can be either minimized the square of the dot-product or, equivalently, maximize the square of the cross-product. For this reason, the following distance measures are computed:

$$F_{NGF}^{(.)}\left(X_R(s), X_S\big(T(s,\mu)\big)\right) := -\frac{1}{2}\int_\mu [N_\epsilon(X_R,s), N_\epsilon(X_S(T(s,\mu)))]^2 \; ds \qquad (3.14)$$

$$F_{NGF}^{(\times)}\left(X_R(s), X_S\big(T(s,\mu)\big)\right) := -\frac{1}{2}\int_\mu \|N_\epsilon(X_R,s) \times N_\epsilon(X_S(T(s,\mu)))\|^2 \; ds \qquad (3.15)$$

In the optimal case, the normalized gradient field using the scalar kernel $F_{NGF}^{(.)}$ and the vector kernel $F_{NGF}^{(\times)}$ has in both the first derivatives equal to zero. Even though the gradient of the scalar product based should be analytically zero at the minimum, in practice, the gradient optimizer could drag to non-zero values because of the implementations. On the other hand, when using the cross product, the metric is not only at the maximum (when gradient vector is parallel) but also when norm of the NGF of the image are zero. These problems bring to the utilization, for the calculation of the NGF vectors, of other kernels different from the two mentioned above, such as: $F_{NGF}^{\Delta\cdot}, F_{NGF}^{\Delta}, F_{NGF}^{\Delta^2}$ [20].

3.3.5. The metric optimization and the choice of MI

The metric selection is one of the most important technical options in the image fusion procedures and the final performance of the entire process might depend from this choice [58]. In image registration the metric has fundamentally two roles: first, to measure the similarity of the reference image and the source, secondly, to calculate the derivatives of the measure varying the parameters. The estimation of the metric is needed to evaluate the similarity of the two images after the application of a candidate transformation. The metric derivatives are required to suggest an optimal combination of parameters to provide a new candidate transformation model for the next evaluation [59]. The results from the calculation of the similarity between the reference and the source images are used by the iterative optimization algorithms to converge to the optimal transformation.

The algorithms for optimization is typically performed in a continuous domain where the similarity function is optimized through continuous variables [60]. Optimization based on continuous variables essentially solves the differential of an objective function. For example, for a constant length of each step, each iteration follows a minimization of the direction of search. Based on the different search method, the most commonly used are: the gradient descent (GD), the conjugate gradient method (CG) and the Quasi Newton method (QN) [60]. The objective optimization function of the GD moves toward the direction that minimizes the difference, or the direction, of its negative gradient. Differently from GD, the CG has a faster convergence since it uses prior knowledge from gradient descent to advance in the conjugate direction of search. The QN has also a better convergence than the GD and, unlike CG, uses a second-order information to speed up its convergence [60].

For multi-modality image registration, MI is the elective state of the art metric [57]; it's usually optimized as fixed function over different candidate alignments of the two images [61]. This method was demonstrated to be highly successful for rigid transformation models [62], thus several approaches have been proposed in order to extend it to non-rigid matching. However, measuring MI presents several notorious drawbacks and therefore its optimization is still considered a hard task. MI, indeed, is defined considering the joint density of the gray value distribution, therefore, many approximations of the density are required and the summation of these typically involves some smoothing parameter which can induce a reduction of the image registration accuracy [57]. Accuracy can be also affected by the non-convexity of the metric in the parameter space that will cause sub-optimal estimation of the deformation model by creating in the MI metric local minima.

Another disadvantage of the MI is its complete decoupling of the gray level values and the pixels location information, hence MI might be considered a global evaluation of the similarity of the images [63].

4.

Materials and methods

In this chapter the process to obtain a deformed 3D geometry of the stent is explained. The procedure is based on the registration of an image coming from a Computer Aided Design (CAD) of the stent with respect to the deformed image from the IVOCT by using the gold standard techniques in image registration. The main purpose of this method is to improve the algorithms previously proposed by decreasing the time of reconstruction with a semi-automatized process. A workflow to evaluate the quality of the deformed geometry is also presented.

4.1.   MATLAB and ITK

The algorithm described in this thesis was developed using the MATLAB software (2017a version, MathWorks, Natick, MA, USA). In addition to the tools that are pre-installed in the standard version of MATLAB, it was required to install the *Medical Image Processing Toolbox* [64] that enables to perform operations such as reading and exporting images. In addition, the algorithms also use some executable that were written using the Insight Tool Kit (ITK) [19].

4.2.   PARAVIEW

To visually assess the results of the registration, the open-source software PARAVIEW (version 5.5, Kitware, Clifton Park, NY, USA) has been used. With this program it is possible to visualize the 3D model and the 3D IVOCT images before and after the registration, in order to evaluate the quality of the process.

4.3.   Stent image from IVOCT frames

The *in-vivo* implanted stent analyzed in this thesis was the XIENCE V (Abbot Laboratories, Chicago, IL, USA), a metallic prosthesis which main characteristics is shown in Table 4.1. This method exploits one 3D COP that comes from the IVOCT image segmentation. The stent struts are first detected in IVOCT images, then the scattered data of points defining the entire stent are used to form the 3D COP. This operation is not part of the registration method that is described in this thesis. However, we can briefly summarize the process in the following steps [2], [17]: i) once the images are loaded in MATLAB, pre-processing is necessary to eliminate image noise; ii) the segmentation phase follows, which can be subdivided in two parts: one procedure for the identification and isolation of the lumen and another one for the stent; iii) a 3D COP is created for both the lumen and the stent and then exported externally.

Table 4.1 Characteristics of the Abbott Xience V

Stent model	Nominal diameter	Effective nominal length
Abbott Xience V 3x28	3 mm	28 m

4.4. 3D stent geometry modeling algorithm

The proposed method for 3D stent geometry modeling is mainly based on image registration. Such procedure allows to register a CAD model to a COP that comes from the segmentation of IVOCT images. The resulting deformed model will give a realistic representation of the coronary stent which in turn can be used as part of a 3D model of the coronary artery. The creation of a realistic geometry of the stent in-vivo allows to define more realistic 3D models of stented coronary arteries, allowing more accurate CFD simulations that better describe the alterations in the local hemodynamics. The possibility to perform better simulations may improve future studies regarding the assessment of the relationship between altered fluidynamic quantities (such as WSS) and the pathological situations (such as ISR). In fact, as already exposed in previous chapters, the insurgence of re-stenosis after the stent implantation is related to the presence of the device that alters the fluid-dynamics in the coronary artery which causes inflammatory response and cells proliferation [3], [34], [35].

The overall workflow of the method is reported in Figure 4.1. The different steps, that will be explained in detail in the following paragraphs and are here briefly exposed. Therea are three main steps of the method: i) image creation, ii) image pre-processing, iii) image registration. During the image creation the two inputs (IVOCT COP and CAD model) are converted into 3D images. From this point forward, the resulting image from the IVOCT COP conversion is considered as the fixed (or the reference) image; on the other hand, the image from the CAD model is considered as the moving (or the source) image. Subsequently, a pre-processing is applied, where the two images are prepared for the next phase, the image registration, which is the main core of the procedure. Registration can be further subdivided into five steps: i) global registration, ii) stent subdivision in rings iii) local registration, iv) total deformation field reconstruction and iv) warp. In the first step, the source image is pre-aligned to the reference by performing a rigid registration. After the alignment, both the source and the reference images are cut in sub-volumes (also referred to as "rings", because each sub-volume should include just one ring) of the stent image. For each pair of corresponding rings, a local registration is performed, including both rigid and non-rigid transformations, and several local deformation fields are given as output. The local deformation fields are combined into global deformation fields that are used to deform the source image and to obtain the final 3D geometry.

The proposed method is a semi-automatic procedure that includes graphical user interfaces (GUIs) at different levels of the process. The GUIs are used: i) to set the image creation parameters; ii) to set the parameters for the pre-alignment of the entire stents; iii) to divide

the images in rings; iv) to set the parameters for the local registration of the rings. Apart from these steps in which the user must interact with the process, the method is automatic, since registration between images and reconstruction of the stent does not require any user intervention.
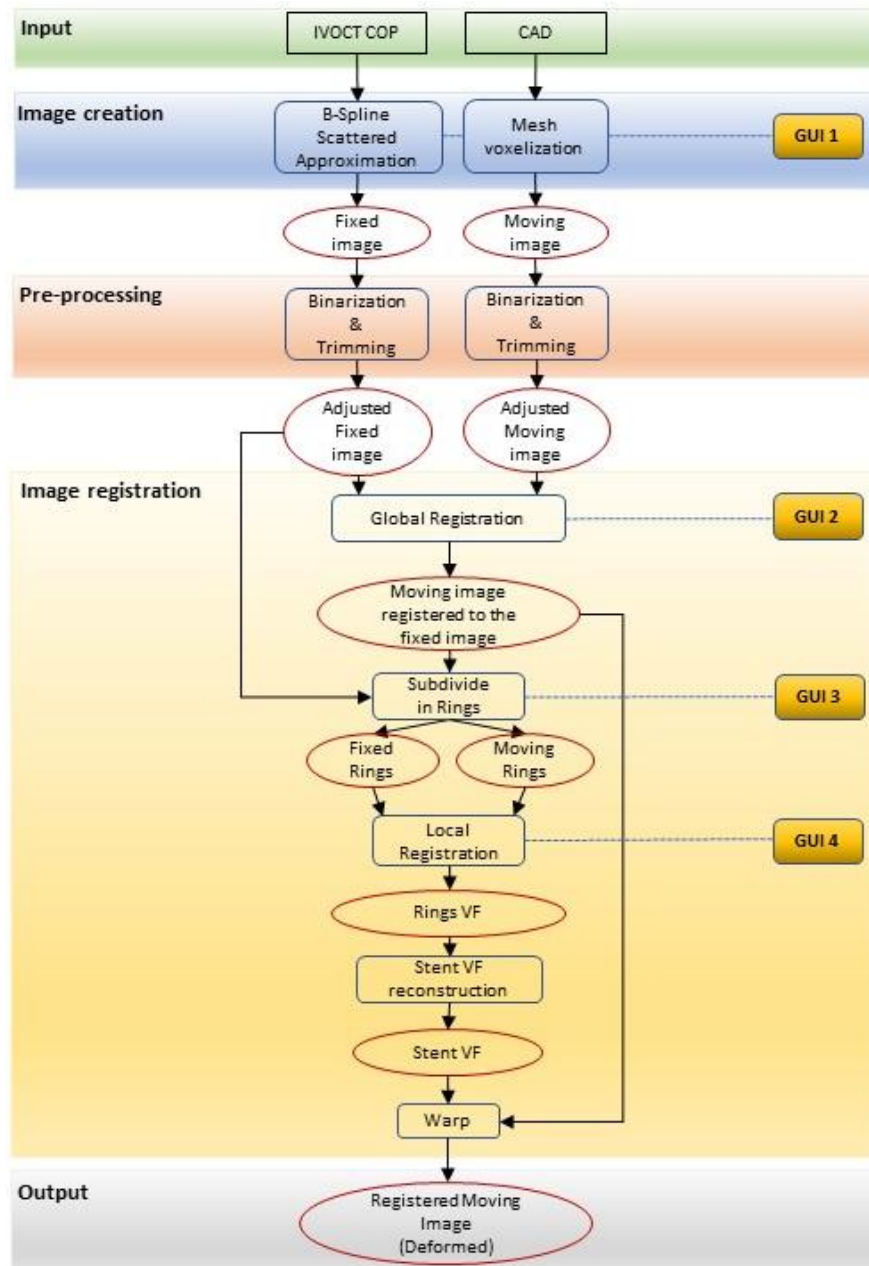

Figure 4.1 3D stent geometry morphing procedure. The workflow can be subdivided into three macro phases: i) image creation where the cloud of points obtained from optical coherence tomography (IVOCT COP) and the CAD of the stent are converted into images; ii) pre-processing, where the two images are binarized and corpped; of iii) image registration which in turn can be subdivide into 5 steps: global registration, cut in rings, local registration, stent deformation vector fields (VF) reconstruction and warp. The final output of the process is the image of the deformed stent model. In the graph, boxes represent operations and circles represent outputs. Operations that require the use of a GUI are also indicated.

4.4.1. Input data

The proposed method starts from the two inputs data: the IVOCT COP and the CAD model. The COP of the deformed stent was obtained from the procedure of Bologna and Migliori et al. [2], [17]. The COP in that method was obtained through the segmentation of the IVOCT images. Such procedure identifies the struts in polar coordinates, by exploiting the peculiar characteristic of OCT images, where the stents struts appear as high reflecting elements followed by a trailing shadow. Based on the analysis of the A-scans, a first set of the candidate pixels is identified. These pixels are selected by considering the slope of the line that connects their intensity to the 30TH low intensity pixel. Such slope must be sufficiently high, which means that there is a significant contrast with respect to the background. Subsequently, a fuzzy logic approach is applied to identify strut pixel and delete false positives. The images are then converted back to Cartesian coordinates. The detected stent is aligned and oriented, following the centerline of the artery phantom, which was assumed to be a straight vertical line. The COP of the stent is then generated from this alignment.

The CAD model of the stent was provided by Abbott Laboratories and represents the true 3D geometry in the non-deformed configuration.

4.4.2. Image creation

In this phase the two inputs are converted into 3D images based on two approaches: i) a B-Spline scattered interpolation of the COP and ii) a voxelization of the CAD model into a binary image. The parameters for generating the images are set from a GUI (as shown in Figure 4.2). Both the operations were performed using executable using the filters available in the free source library ITK [19]. Details on how these executables work are reported in the following paragraphs.

B-spline scattered data point interpolation

The conversion of a scattered data point into image is done through the algorithm developed by Tustison et al. [65]. The algorithm is implemented in the filter *BSplineScatteredDataPointSetToImageFilter* of ITK. The work of Tustison et al. extends the 2-D scattered data interpolation with multi-level B-Splines (developed by Lee et al. [66]), into N dimensions. In the Tustison et al. method, given an N-D irregularly spaced scattered data, the developed filter finds a fast approximation using uniform B-Splines. B-Splines are the most used functions for computational geometric representation. In general, uniform B-Splines have two important properties:

i. Locality: Each point of the 3D scattered data approximated by a B-Spline with degree d is influenced by only the corresponding 3D uniform grid consisting of $\prod_{j=1}^{N}(d_j + 1)$ control points where d_j is the degre of the spline in j^{th} direction.

ii. Continuity: A B-Spline curve of degree d has continuity C^{d-k} at the knots k and it is smooth elsewhere.

The approximation of the scattered data is based on the definition of a set of B-Splines and a grid of control points. To reconstruct the object, the B-Splines serve as a weighted averaging function for the set of control points. For example, for 3D scattered data a B-Spline volume is a function with three variables:

$$V(u, v, w) = \sum_{i=1}^{M}\sum_{j=1}^{N}\sum_{k=1}^{P} \boldsymbol{P_{i,j,k}}\, B_{i,d}(u)B_{j,d}(v)B_{k,d}(w) \qquad (4.1)$$

Where $\boldsymbol{P_{i,j,k}}$ is the set of control points and $B_{i,d}(u)B_{j,d}(v)B_{k,d}(w)$ are the B-Spline basis functions of degree d. The latter functions serve to weight the contribution of each control point to $V(u, v, w)$ based on its distance to the scattered data in (u, v, w). With this formulation, the problem of deriving the function V is reduced to solving for the control points in $\boldsymbol{P_{i,j,k}}$ that best approximate the scattered data [66].

In the executable one must set the degree of the B-Spline and the number of the control points is obtained accordingly $(\prod_{j=1}^{3}(d_j + 1)$, where d_j is the degre of the spline in j^{th} direction.). Multi-level approximation is as well implemented by setting the levels of B-Splines in the executable, bringing to a better approximation of the data by increasing at each level the number of control points to twice the previous one. In addition, in the algorithm the user must set the spacing of the output image and for this particular test it was set to 15μm - 15μm - 15μm respectively in the x, y, z direction. The algorithm works by approximating the scattered data points given the parametric dimension (3 for the deformation field for 3D scattered data points, i.e. *<dx(u,v,w), dy(u,v,w), dz(u,v,w)>*). The output is an image defining the sampled B-Spline parametric domain where each voxel contains the sampled B-Spline object value [65].
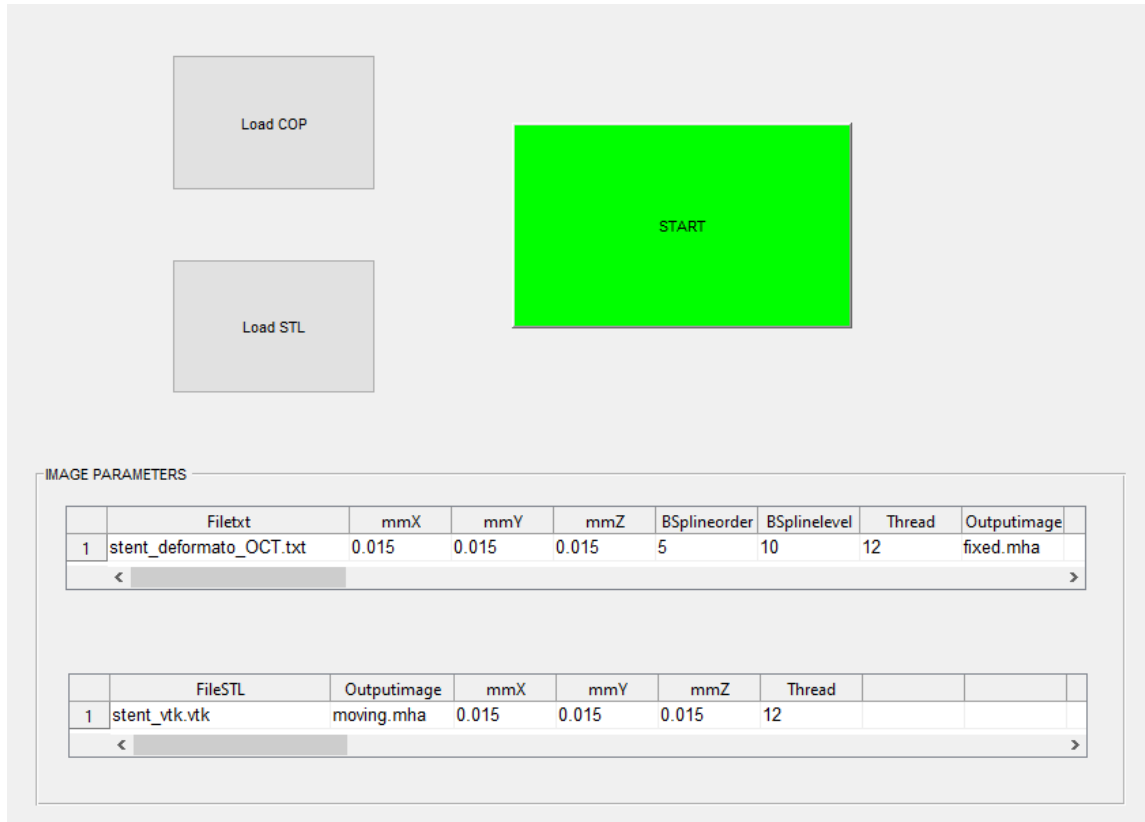
Figure 4.2 MATLAB GUI in which the parameters necessary for the image creation step are set. Parameters are defined for the creation of both the fixed image, coming from the IVOCT COP, and the MOVING image, coming from the CAD model. In the former, the conversion is performed by a B-Spline scattered data interpolation. In the latter, the conversion is performed through voxelization of the original CAD.

CAD model to image

The creation of the image coming from the CAD model (in STL format) of the non-deformed stent is also computed exploiting an executable which uses a function from the ITK library [67] and performs a voxelization process. This algorithm is implemented in the ITK filter *itkTriangleMeshToBinaryImageFilter*, which, taken a 3D CAD as input returns a binary image as output. In this executable, similarly to the previous of the IVOCT COP image creation, the user is allowed to set the spacing along the three dimensions. The same resolution as the fixed image was used (15μm - 15μm - 15μm in the x, y, z direction respectively).

4.4.3. Image pre-processing

After the 3D images are created, they undergo a pre-processing step before the image registration phase. Such pre-processing consists of two operations: i) binarization and ii) trimming.

Binarization

After converting the COP into a 3D image by performing the B-spline scattered approximation, the 3D volume loses its binary property due to the effect of the interpolation. In fact, the voxels contain grey values ranging from 0 to 255 , unlike the original scattered points (was value was either zero, for background, or 255, for the stent). A spread in the distribution of grey values of the pixels may cause an increase in the computational cost of the registration process. Binarizing the intensity level distribution to just two values helps to increase the contrast level of the stent with respect to the background. Therefore, a re-binarization of the volume is performed. The same operation is applied also in the CAD model, altough this could be usuless since the executable outputs already a binary image but still is applied in order to prevent problems in the following phases. The binarization is based on setting the median of each histogram as a threshold and re-assigns the new value of the voxel, either to 0 or 255 (if the intensity level value is below or above respectively).

Trimming

The computational cost of the registration increases also as a function of the number of voxels in the source and reference. In the raw images that were created in the previous step, the bounding box of the stent is much smaller than the entire field of view. In fact, such 3D images also contain many background voxels that have null value located externally to the stent. If these voxels are considered during the registration process, they cause an increase in the computational cost without providing any additional information. To remove such voxels a trimming operation of the 3D image is performed. The trimming is obtained by reducing the 3D image to the bounding box of the stents with an addition of only 20 layers of background voxels along the x and y axis. The number of additional layer of background voxels (20 in this case) was empirically chosen only as a good trade-off between computational cost and registration quality. A description of this operation is shown in Figure 4.3.
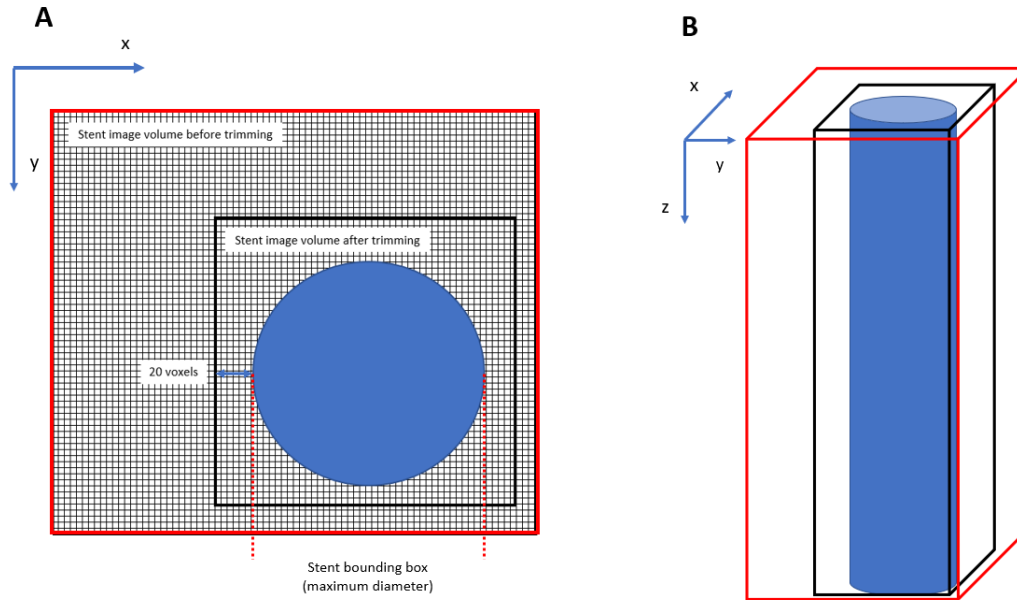
Figure 4.3 Representation of the trimming operation, performed in order to reduce the number of voxels external to the the stent (blue circle). A) View in the x and y plane where the red line indicates the previous volume of the image and the black line, after the trimming. A margin of 20 layers of background is added for better quality of the registration. B) The 3D image volume of the stent is shown before (red line) and after the trimming (black line).

4.4.4. Image registration

The image registration phase is the main core of the proposed method and it allows to super-impose the source (the CAD model image) to the reference (the IVOCT COP image) to obtain the final deformed 3D model of the stent.

The registration can be subdivided in two steps: a global registration and a local registration. This division is necessary because the computational cost required to perform non-rigid transformations on the whole stent will be too high for a common laptop and system crashes due to memory shortage will occour. Therefore, the global registration provides a first rough rigid super-imposition of the source on the target, and in the subsequent local registration the non-rigid deformations are applied on the single sub-volumes rather than the entire stent image, strongly reducing the computational cost. The output of the local registration are the deformation vector fields (VFs) necessary for the registration of each ring. Such local VFs are then combined togheter to build the VFs for the non-rigid registration of the entire stent (details about this will be reported in the following paragraphs).

In this phase it is possible to use the techniques for the image registration discussed in chapter 3. For both the global and the local registration, the method exploits executables that were developed in a doctorate thesis [20]. In these executables, used the algorithms for the registration that are available in the ITK library [19]. Such algorithms enable to perform both

rigid and non-rigid registration. There is one executable for each type of transformation: scaling, translation, roto-translation, affine and B-Spline interpolation. In the present study these executables are used in various MATLAB functions. In particular, during the global registration, only rigid transformations are applied (translation and roto-translation); on the other hand, in the local registration all the five transformations mentioned before were used. The peculiarity of the executables mentioned before is the possibility to choose from different metrics of the registration: MSE, MI, NGF, MI+NGF. In this study, only two of these metrics have been used: MSE for the translation in the global registration; MI for all the other transformations

MI was the mostly used metric in the proposed registration method, since it is the best for multi-modality registration and in general, compared to the other metrics, it has the ability to provide a good estimation of the common information between the two images that come from two different image acquisition modality. This is done through the estimation of the marginal and joint probability density function based on Mattes et al. MI estimation [54],[55]. MI computation requires high calculations and the use of this metric at this stage is only possible when the distance between the two images is decreased after the translation, where MSE is used. This same reason brings again to the choice of MI for the local registration because after the subdivision in sub-volumes of the stent, in theory, there should be a good correspondence between the images following the global registration. The choice of the MSE instead, during the global registration, is motivated from the fact that initially both the images are distant from one another and a huge number of iterations is required for the translation. MSE, among all the other metrics, is the lightest in terms of computational cost, therefore, it is suitable for the initial translation of the moving image to the fixed image.

The process of registering the moving to the fixed image is done iteratively, computing at each iterations the MI (or MSE) between the two images. In order to optimize the objective function by maximizing the MI (or minimizing the MSE) [20], the gradient descent is used as an optimization algorithm. After a few steps from the beginning of the registration, the gradient descent gives the right direction for the maximization (or minimization) of the similarity function (or the cost function).

To control the registration, the executables accept as inputs a series of parameters that for the rigid transformations (scaling, translation, rotation, general affine) are all the same, except for the number of optimization weights that depends on the degree of freedom of each transformation: 3 for scaling (in the 3 axes - [Sx, Sy, Sz]); 3 for translation (along the 3 axes - [Tx, Ty, Tz]); 6 for roto-translation (3 for the rotation around the 3 axes - [α, β, γ] and 3 for

translation – [Tx, Ty, Tz]); 12 for general affine (6 for roto-traslation - [α, β, γ , Tx, Ty, Tz], 3 for scaling - [Sx, Sy, Sz] and 3 for shearing – [Ax, Ay, Az]). In addition to these optimization weights, there are other parameters, and they are listed in Table 4.2.

Table 4.2 Registration parameters that are mainly used for the rigid transformations and that are needed to be input in the Eros Montin's executables.

Max step	The initial step that the gradient descent optimizer computes
Max step divisor	This method adopts multi-resolution registration. This value, divides the Max step of the gradient descent at each level
Min step	The minimum step to reach for the registration to stop
Min step divisor	This method adopts multi-resolution registration. This value, divides the Min step of the gradient descent at each level
Metric	MSE or MI
Number of Bins (for MI)	For the MI metric, the marginal and the joint PDF are evaluated at discrete positions or bins uniformly spread within the dynamic range of the images.
Levels	The levels of multi-resolution registration
Max iterations	The maximum number of iterations above which the registration stops
Max iterations divisor	The divisor of the iterations at each level of the multi-resolution registration
Geometrical transformation parameters	Scaling (3) : Sx, Sy, Sz Translation (3) : Tx, Ty, Tz Roto-translation (6) : α, β, γ, Tx, Ty, Tz General affine (12) : α, β, γ, Tx, Ty, Tz, Sx, Sy, Sz, Ax, Ay, Az

For the non-rigid registration, another executable is used. In this part, the moving image is deformed following the fixed image by using again MI as the cost function to be optimized. The MI metric is characterized by two components when used in image registration: the geometrical transformation and the interpolator. The geometrical transformation is used to map points from the fixed to the moving image domain. This is done automatically by the gradient descent optimizer which explores the transformation space domain. The interpolator is used to evaluate the image intensity at a user specified geometric points in the moving image. For this method, B-splines are used as interpolator. In the executable, apart from the metric (MI), the user is required to set a series of inputs. Among these, the most important are: i) the spacing of control points along x, y and z direction; ii) the maximum number of iterations; iii) the number of bins for the evaluation of the marginal and the joint PDF based on Mattes et al. estimation of the MI.

Global registration

Initially, both the fixed and moving images may not share the same origin and thus, they may be distant from one another. For this reason, preliminary alignment of the images is performed, to provide a better initialization of the 3D space to be registered. The parameters of the rigid transformation may be initialized using a GUI (as shown in Figure 4.4).
Since the optimization through gradient descent depends on the initialization, the global registration may not instantly give the optimal result in terms of alignment between the two images. Therefore, it could take more than one try before achieving a good registration. In this phase it may be useful to visualize the results at each attempt on Paraview.
In general, global registration is based on two rigid transformations: i) translation and ii) roto-translation. The aim is to achieve the best stents' structure correspondence between the two images. In these transformations, the moving image is registered on the fixed image by using MSE and MI as metrics for translation and roto-translation respectively.
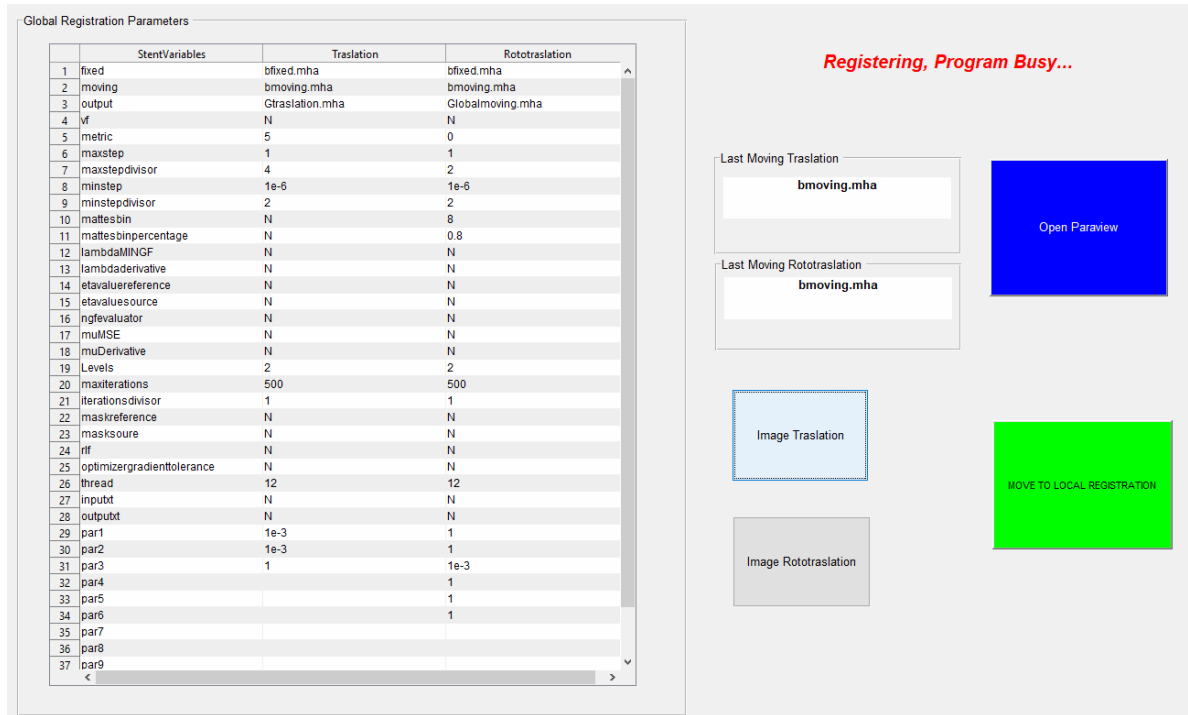
Global Registration Parameters

	StentVariables	Traslation	Rototraslation
1	fixed	bfixed.mha	bfixed.mha
2	moving	bmoving.mha	bmoving.mha
3	output	Gtraslation.mha	Globalmoving.mha
4	vf	N	N
5	metric	5	0
6	maxstep	1	1
7	maxstepdivisor	4	2
8	minstep	1e-6	1e-6
9	minstepdivisor	2	2
10	mattesbin	N	8
11	mattesbinpercentage	N	0.8
12	lambdaMINGF	N	N
13	lambdaderivative	N	N
14	etavaluereference	N	N
15	etavaluesource	N	N
16	ngfevaluator	N	N
17	muMSE	N	N
18	muDerivative	N	N
19	Levels	2	2
20	maxiterations	500	500
21	iterationsdivisor	1	1
22	maskreference	N	N
23	masksoure	N	N
24	rlf	N	N
25	optimizergradienttolerance	N	N
26	thread	12	12
27	inputxt	N	N
28	outputxt	N	N
29	par1	1e-3	1
30	par2	1e-3	1
31	par3	1	1e-3
32	par4		1
33	par5		1
34	par6		1
35	par7		
36	par8		
37	par9		

Registering, Program Busy...

Last Moving Traslation
bmoving.mha

Open Paraview

Last Moving Rototraslation
bmoving.mha

Image Traslation

MOVE TO LOCAL REGISTRATION

Image Rototraslation

Figure 4.4 MATLAB GUI in which the parameters for the global registration of the moving stent to the fixed stent are set.

Subdivision in rings

Before local registration, both the source and target images are ready to be subdivided in multiple sub-volumes. The reason of the subdivision is that, since the non-rigid registration requires a huge amount of calculations, working on the entire stent brings to crashes of the executables due to excessive consumption of system memory.

The subdivision process is managed by a GUI in which both the stent images are cut in 20 sub-volumes (Figure 4.5A). The number 20 has been used because it is the number of stent repetitive units (a.k.a *rings*). For this reason, from now on, we will use the term sub-volume and ring as sinonyms . In this phase, the subdivision is done by looking to the fixed image and by choosing along the z coordinate ot the planes that will define the boundary between two rings at the level of the stent's bridges (the metallic beams that link one ring with the next one). The cutting planes are used for the moving image, therefore, the corresponding fixed and moving ring share the same image space. Figure 4.5B and Figure 4.5C represent examples of stent partitions used before local registration.

During the pre-alignment from the global registration the two stents may not result perfectly aligned and some dephasing of the moving with respect to the fixed stent may be present. For this reason, while for the fixed image the fact that one sub-volume contains one complete ring is assured (because the cut is done by the user), the same cannot be guaranteed for the moving

image, for which a ring may be between one sub-volume and the next one. To solve this, each sub-volume is expanded in the z direction in order to have an overlap between contigous ring. The expansion of the sub-volume adds a number of layers along the z direction (above and below) that is the 35% of the length of the ring (as obtained by choosing the points in the GUI). In this way, there is a good possibility that the ring structure of the moving image is preserved even after the subdivision, bringing to a better local registration. On the other hand, this generates overlapping between the sub-volumes.

From now on, the resulting rings will be referred to using numbers from 1 (the most distal ring), to 20 (the most proximal ring).
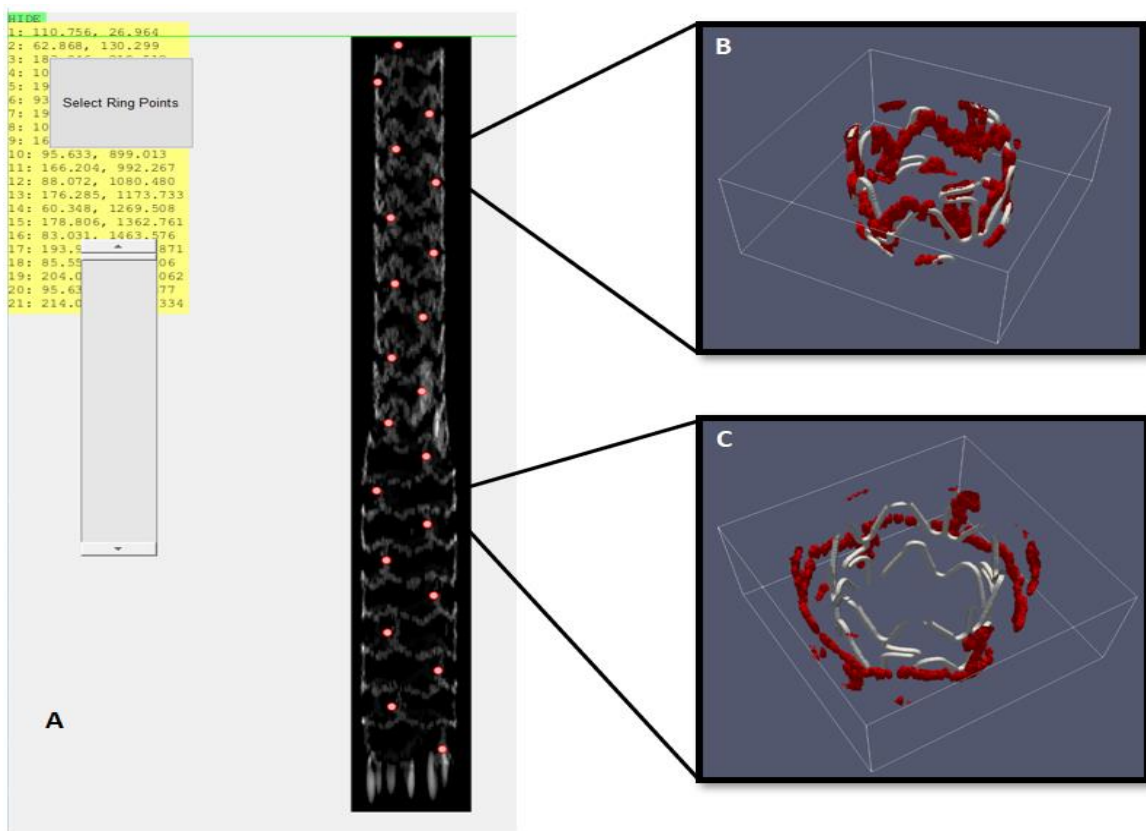
Figure 4.5 A) GUI for cutting both the fixed and moving images in rings. The red dots indicate the z-values for the cutting planes. B) Detail of the 4th ring in Paraview with moving ring in white and fixed ring in red. C) Same details for the 15th ring.

Local registration

After rings subdivision, the local registration is performed. Such operation allows to obtain local VFs for each sub-volumes in each transformation. In particular, each moving ring is registered to the corresponding fixed ring with this sequence of transformations: i) scaling (S); ii) translation (T); iii) roto-translation (R); iv) general affine (A); v) non-rigid B-splines (B)(Figure 4.6). This process results in 100 different VFs (5 transformations * 20 rings).

The transformations, both rigid and non-rigid, have the same input parameters of the ones described for the global registration, except that, in this case, scaling and general affine are also considered (with rigid registration) and a final deformation of the ring is done by applying a non-rigid registration using B-splines interpolation.

Prior to the ring by ring registration, the parameters for the transfomations are initialized from a GUI (Figure 4.7). The optimal parameters for local registration may depend from the particular ring considered. In fact, because of the deformed structure (larger diameter) of the stent, the parameters that are set for the first ring may not be suitable in the proximal portion (approximately from ring 12 to the end). For this reason, if needed, the registration parameters may be reset at any iteration. However, in our case, such parameters set was performed only twice (at ring 1 and kept till ring 11 and at ring 12).
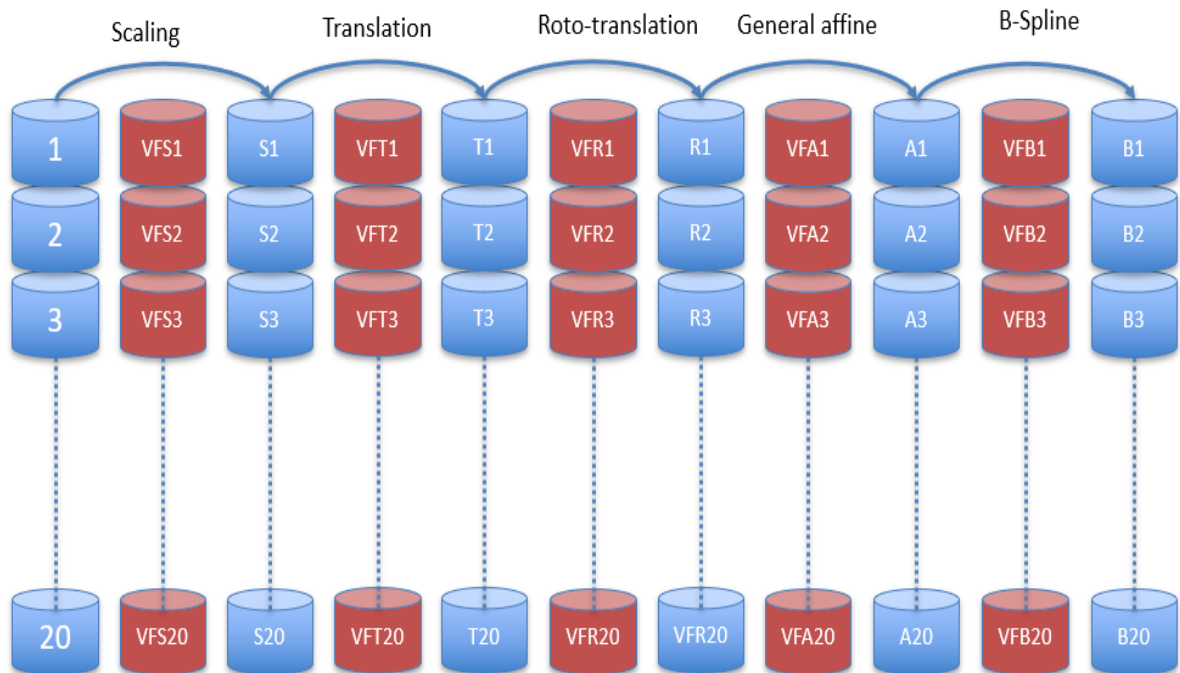

Figure 4.6 Scheme of local registration applied for each ring. The main output for each transformation in each ring are the VFs (VFSn, VFTn, VFRn, VFAn, VFBn) with a total of 100 VF for all the rings at the end of the local registration. Sn, Tn, Rn, An and Bn are the output image of each ring for each transformation.
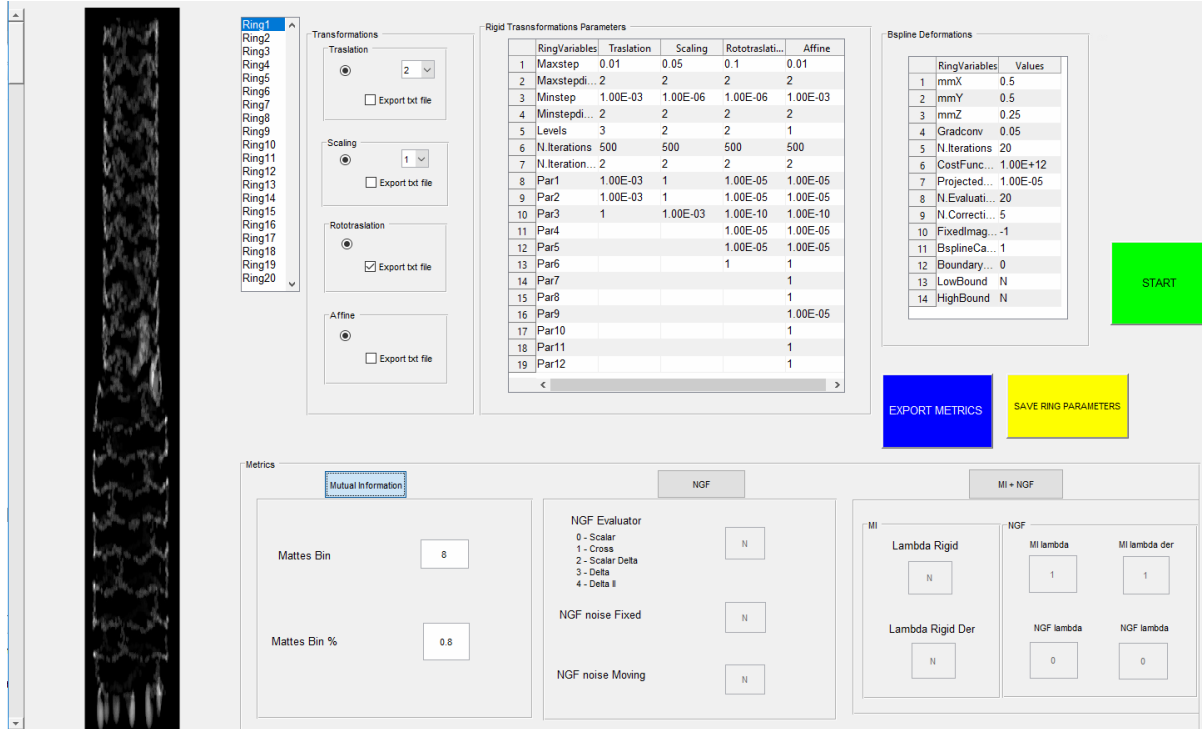
Figure 4.7 The GUI for the ring by ring registration parameters input. In this phase the registration is based on the parameters that the user inputs for each ring.

Rebuild of the VF of the entire stent

Rebuilding the entire stent is done by combining the VFs created at each ring registration. The rebuild process of the VFs will result in 5 VF for the entire stent: VFS (for scaling), VFT (for translation), VFR (for roto-translation), VFA (for general affine), VFB (for B-spline non-rigid deformation).

The ring's VF at the n-th iteration is attached to the previously stacked partial built VFs (a representation of this rebuilt process is shown in Figure 4.8). The entire stent VF for all the transformations is rebuilt iteratively. The process of stacking one VF to another for two consecutive rings has to take in account the overlap region between these two. In fact, as mentioned during the subdivision phase, a few layers above and below the ring were added in order to let the moving ring image structure be more complete prior the registration, due to the fact that the cutting was based on the fixed image and misalignments between the two could still be present.
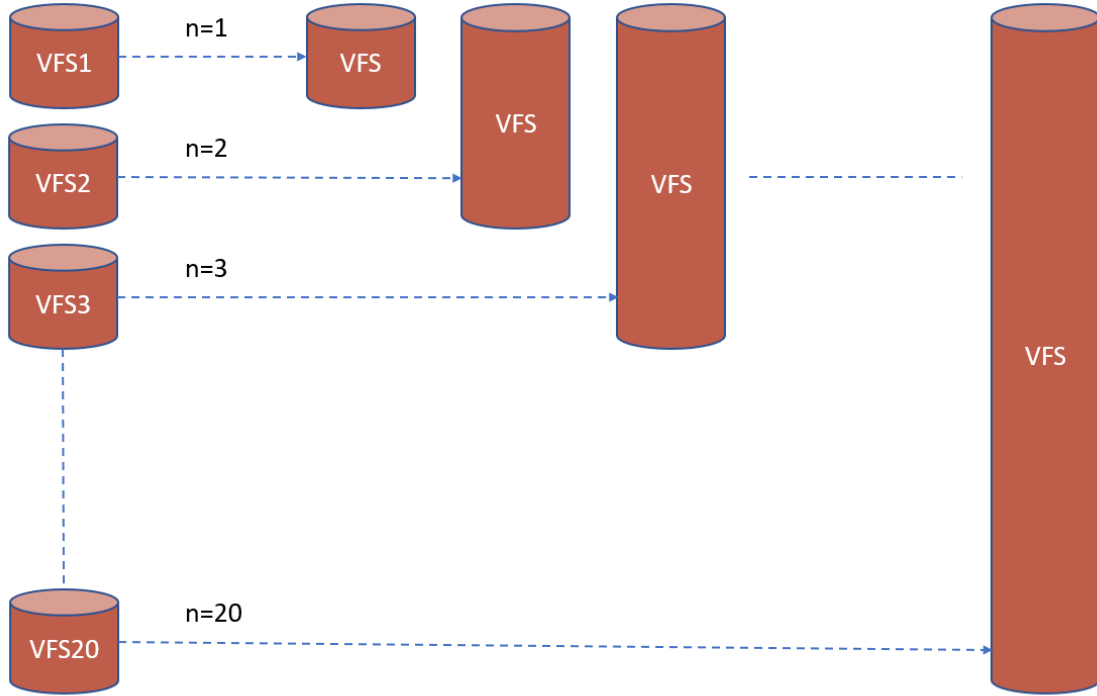
Figure 4.8 Scheme of the rebuild process of the vector fields (VF). In the example, the vector field for scaling transformation (VFS) is shown. The VF of the nth ring is attached at the nth iteration to the previously partial built VFS. As the result, the entire VFS is obtained.

The iterative process used to build a complete VF is herein described (see also Figure 4.9). In the n-th iteration, two regions are stacked on the partially created vector field: i) the non-overlapping region of VF_n and ii) the overlapping region between VF_n and VF_{n+1}. In the non-overlapping region, only the VF_n is considered. In the overlapping region, first, the two VFs are resampled so that they share the same grid, and then a combined VF is computed. An exemption has to be made for the last ring where the whole non-overlapping region of VF_{20} is considered since there is no presence of overlapping with further rings. The combined VF in the overlapping region is a weighted average of VF_n and VF_{n+1}, according to equation (4.2)

$$VF_{overlap}(i) = \frac{N-i}{N} * VF_n(i) + \frac{i}{N}VF_{n+1}(i) \qquad (4.2)$$

Where N is the number of layers in the overlapping region and $i \in [1, N]$ is the index for the layer, i=1 being the most distal layer and i=N being the most proximal one.
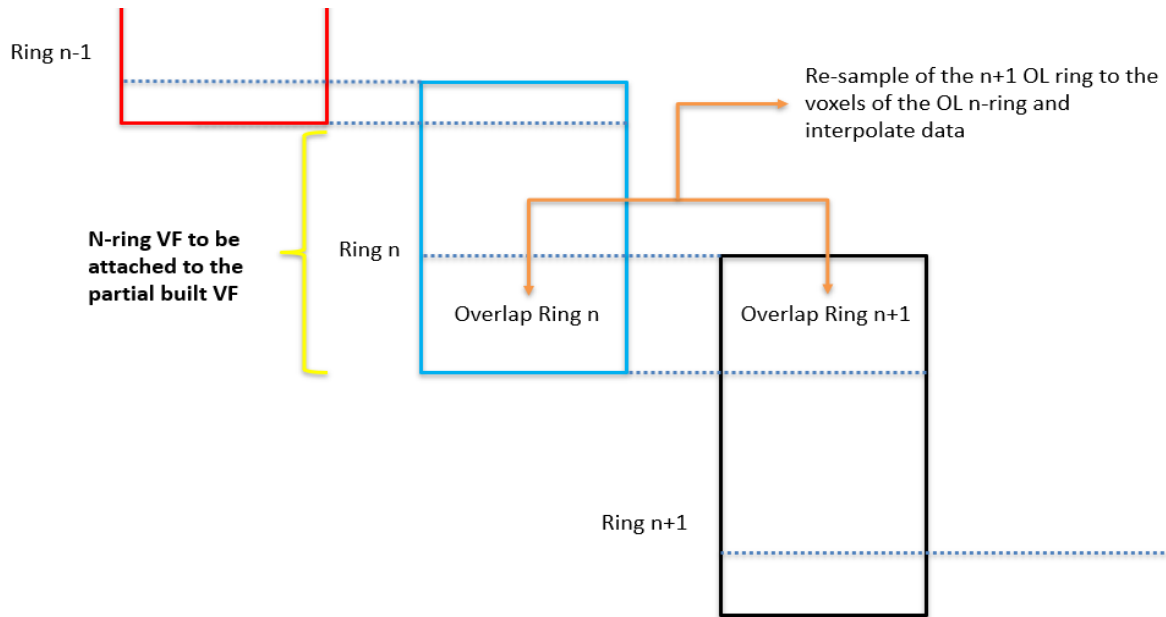
Figure 4.9 A representation of the rebuild process that considers contemporarily consecutive rings. The nth ring is composed by two regions: the non-overlapped and the overlapped region. The overlapped region needs to be adjusted with respect to the n+1 ring overlap with a linear interpolation so that the overlapping layers closer to the nth ring weigh the VF of the nth ring more and viceversa.

Application of the vector fields (warp)

Once the local registration and the stent rebuild are performed, the VFs of the 5 transformations are available. These VFs (VFS, VFT, VFR, VFA and VFB, for scaling, translation, roto-translation, affine and B-spline respectively) will have the same dimension of the initial entire stent image (both moving and fixed). To obtain the final deformed 3D geometry of the stent, the VFs are applied in cascade by warping the initial moving stent image. A scheme of this process is represented in Figure 4.10.
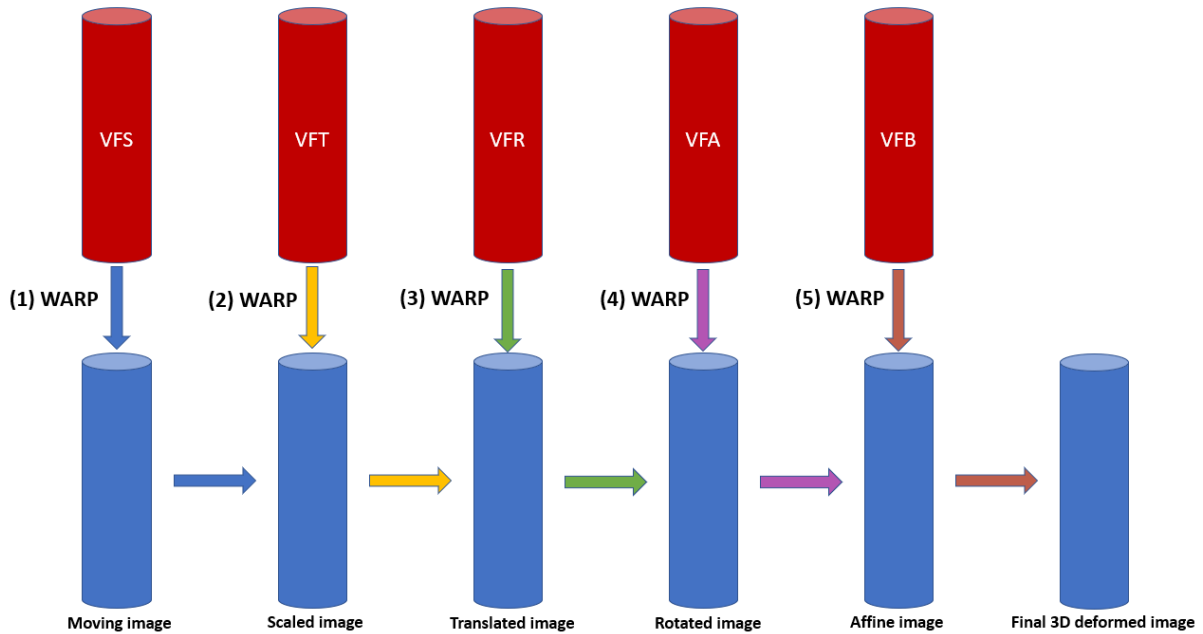
Figure 4.10 Application of the vector fields in cascade to obtain the final 3D deformed stent image.

4.5. Evaluation

For the evaluation of the proposed method the distance between corresponding points of the extracted centerline (an average line of a solid geometry) of the registered image and the centerline of the fixed image (from IVOCT) is computed. The centerline (in a form of a line of points) from the registered image is first obtained using the software MIMICS (Materialise, Leuven, Belgium) and it is exported and read in MATLAB as a Nx3 matrix containing the x, y, z coordinates of the points. Subsequently the distances, stored in a Nx1 array, between each point of the IVOCT COP and the closest point of the deformed CAD centerline is calculated. This array is confronted with a same array of distances obtained from Bologna [17] in which the centerline of the IVOCT was evaluated against the centerline of the stent from μCT reconstruction (a technique that uses the same principles of the conventional CT but with a higher resolution, in the order of tens of microns).

In Bologna [17] the array of distances was obtained after a roto-translation transformation that superimposes the centerline of the μCT to the centerline of the IVOCT. The superimposition is optimized by using a Powell optimization (i.e. optimization of one parameter at a time) and then the Iterative Closest Point (ICP). In the study [17], after a translation of the two COPs in order to have the center at the origin, each of the 6 roto-translation parameters are first optimized starting from the 3 parameters of the translation,

by finding the ones that minimize the error of the two COPs; then, the rotation angle around the z axis (360 iterations, each of 1 degree step) is also optimized. Last, to obtain the optimal roto-translation matrix, the ICP algorithm is performed, in which the error (MSE) between the two COPs is minimized.

The array of distances is used as an index of the quality of the reconstruction. In the proposed method the quality must be assessed by considering the final array of distances as a result of the best deformation of the model, from the registration process, with respect to the IVOCT image. Since the results in Bologna's experimentation brought to a good superimposition between the IVOCT and the micro CT centerline after the registration, the results, in terms of array of distances, of the proposed method can be considered reliable if they are similar to the ones obtained in that study. To allow such comparisons and to obtain a qualitative analysis, the boxplots of the array of distances were obtained and a statistical test (Mann-Whitney test) was performed to detect significant differences.

In addition to the evaluation of the distances of the entire stent, the distances between the IVOCT COP and the registered image centerline of each of the 20 rings were also computed. With this analysis, it is possible to compare the performance of the algorithm between different regions of the stent and understand where the registration performs worse and why. A statistical analysis is again performed, by showing into a table the quartiles of the distances for each of the 20 rings as well as the histograms of the total distances distribution.

5.

Results and discussion

In this chapter the results of the 3D stent geometry reconstruction resulting from the proposed algorithm are shown. First, the distance between the registered image's centerline and the COP of the IVOCT is compared to the Bologna's [17] distance between the same stent from IVOCT and μCT scans. Then, a detailed analysis of each rings is accomplished highlighting the differences in terms of performance between rings.

5.1.   Image registration results

In Figure 5.1A the IVOCT image resulting from the B-Spline interpolation of the 3D COP is shown. It is possible to observe that the geometry of the stent is clear and the radial deformation in the superior regions, due to balloon expansion, is noticeable. However, the lack of details of the structure is still present and, in addition to this, there is a lack of points due to the shadow caused by the reflection of infrared light on the metallic guide during the acquisition process of the OCT. On the other hand, the image obtained from the model has a defined geometry and the stent structure is well represented Figure 5.1B.
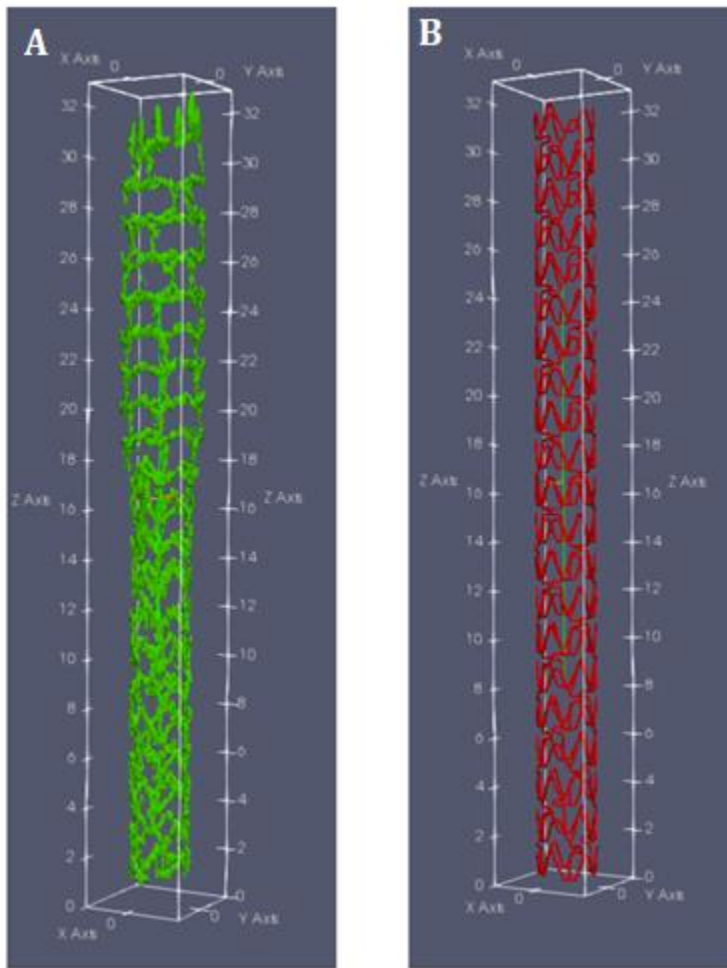
Figure 5.1 View of the 3D images of the IVOCT and CAD in Paraview. A) The resulting image of the B-spline interpolation of the IVOCT COP. It is possible to notice that the conversion brings to a clear geometry of the stent, but the details of the structure are lacking. B) The image coming from the conversion of the CAD model.

The whole operation of stent geometry modeling from this algorithm, including the pre-processing, in which the images are prepared to the next phase of global, local registration and stent reconstruction took around two and a half days. This time also includes the manual part of the process, where the user is asked to interact with the GUI's to input the parameters.

The final stent geometry obtained after the 3D modeling is shown in Figure 5.2A. By putting the images (the IVOCT and the registered model) one on top of the other (Figure 5.2B), it is possible to observe that in general there is a good superimposition. The result of the registration is better at the level of the distal region (Figure 5.2D) where the stent is less deformed. On the other hand, in the proximal region (Figure 5.2C), where there is the presence of a radial deformation, the moving image (model) was still able to follow the fixed image (IVOCT) but with lower degree of deformation, from the point of view of structural details, although the scaling and the roto-translation transformations performed well.
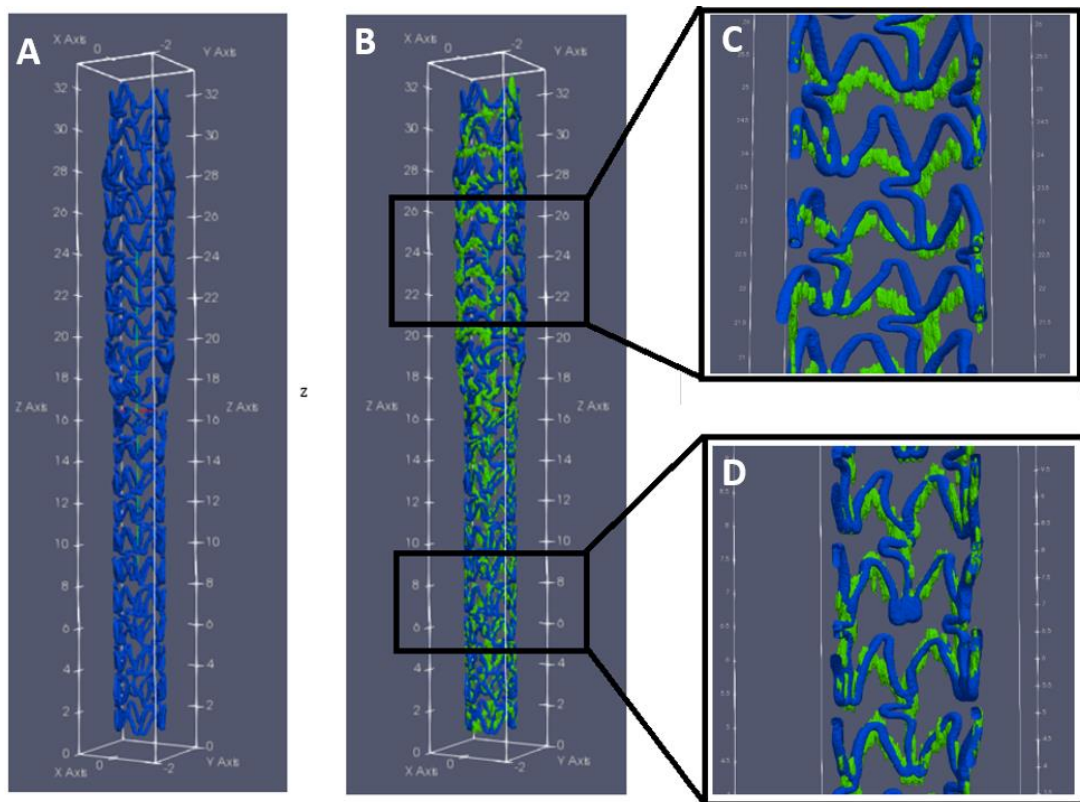

Figure 5.2 Screenshots in Paraview of the resulting registered image of the model (A) and the superimposition with the reference IVOCT image (B). The good result of the registration in the early rings can be observed in (D) with a good matching between the two structures. In the late rings (C), a macro deformation was still obtained, although the structures are not perfectly matching.

5.2.   Algorithm evaluation results

Figure 5.3A shows the plot of the registered model centerline (red) superimposed to the IVOCT COP (blue). The resulting distances between these two centerlines were compared to the distances between the μCT and IVOCT COP. In Figure 5.3B is shown the centerlines of the μCT (green) and the IVOCT COP (blue) before the application of the ICP + Powell algorithm; whereas in Figure 5.3C is shown the same centerlines after the registration.
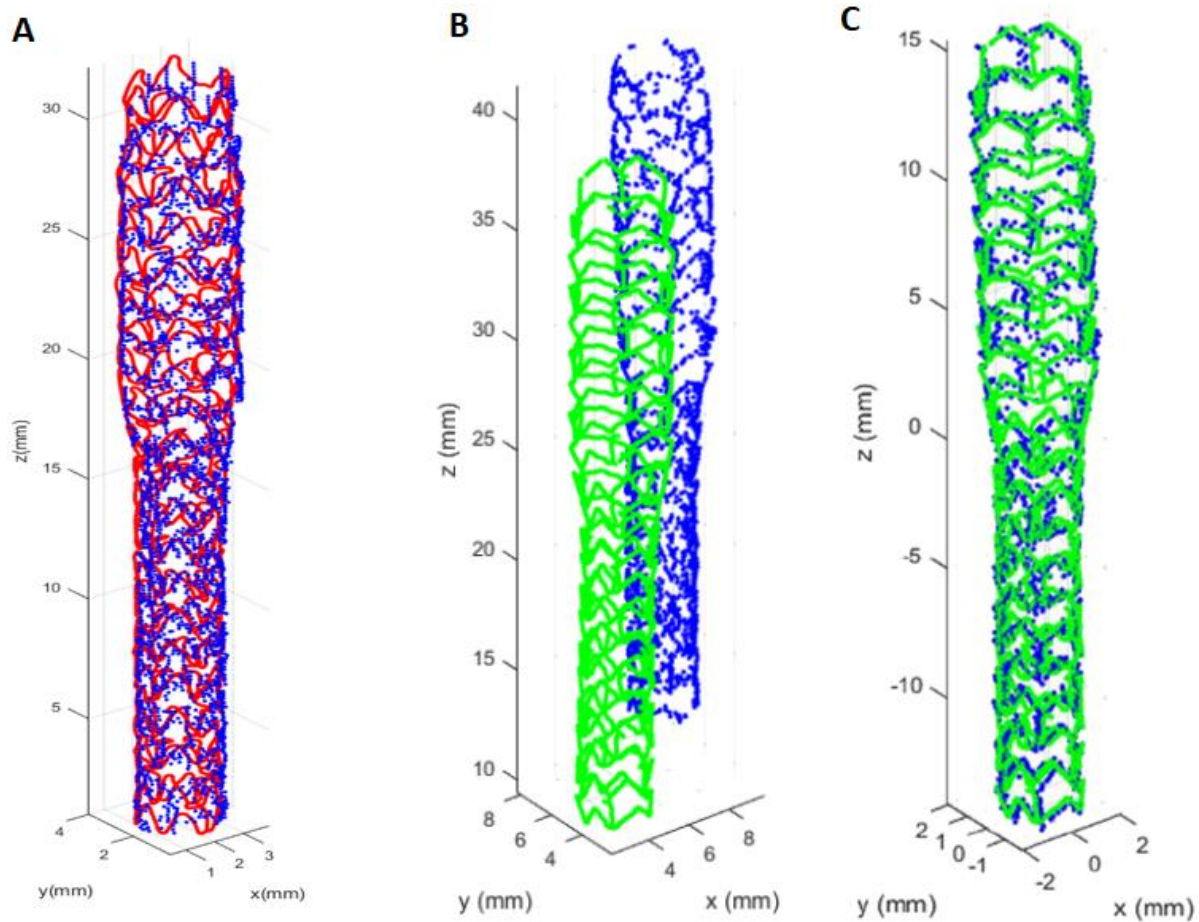

Figure 5.3 View of the different registered point clouds in MATLAB: A) the IVOCT (blue) and the registered model (red) centerline; B) the IVOCT (blue) and the μCT (green) centerlines before the registration; C) the same centerlines after the registration.

The statistical analysis shows that the overall IVOCT-µCT distances distribution is lower compared to the IVOCT-model as highlighted in the boxplot in Figure 5.4 and more specifically in the Table 5.1, where the quartiles and the median are shown. It can be observed a difference of around 40 µm between the medians of the two distributions. Although the Mann-Whitney test proves a significative difference between the results (p<<0.05), the histograms (Figure 5.5, Figure 5.6) seem to demonstrate a distribution similarity with even a slight better compactness (maximum distances ~ 650 µm) in the case of IVOCT – model (versus ~ 900 µm in the IVOCT-micro CT).
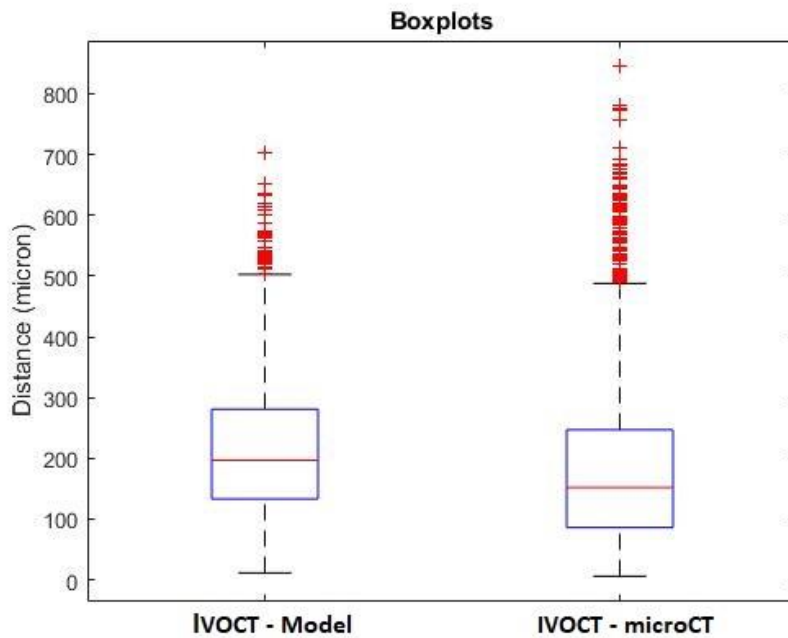

Figure 5.4 Boxplot of the two distances. The IVOCT-micro CT shows an overall distribution of distances that is lower with respect to the IVOCT-model distance distribution.

Table 5.1 The quartiles of the two distances distributions.

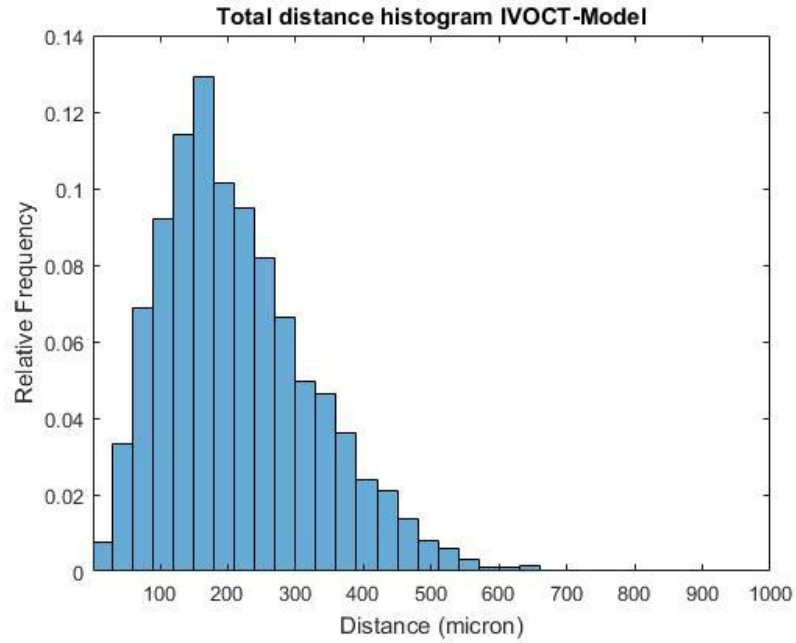| Quartile	1ST	2ND	3RD
IVOCT – Model (µm)	133.11	196.68	281.05
IVOCT – µCT (µm)	86.10	152.01	246.84

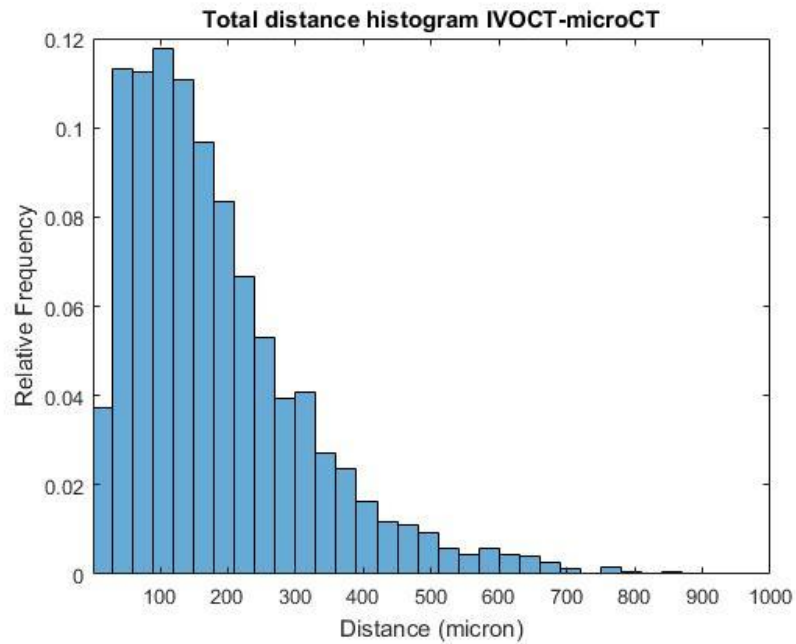*Figure 5.5 Histogram of the IVOCT-model distance distribution.*

Figure 5.6 Histogram of the IVOCT- µCT distance distribution.

5.3. Comparisons of the 20 rings

An overall better performance of the algorithm in the early rings of the stent is observable (look for details between Figure 5.8 - Figure 5.27), from the starting rings up to ring 10 (with the exception of ring 1 and ring 6) where the median is less or equal than 170 μm, with the best results in ring 4 and ring 10. On the other hand, in the region of the stent from ring 11 to 20 where there is a higher presence of deformations, which lead to a worse performance of the algorithm characterized by an overall increase of the distances. These observations can be also seen in the side by side comparison of all the ring in Figure 5.7 where there is an evident shifting to the bottom of the figure in the early rings. In the following figures from Figure 5.8 to Figure 5.27 are shown one by one the results of the registration for all the ring. In particular there are represented the initial non-deformed stent (left part of the figure in red) super-imposed to the fixed image of the COP (green) and the final deformed stent (right image in blue). The boxplots, the histograms and the quartiles of the resulting distance for each ring registration are as well shown.
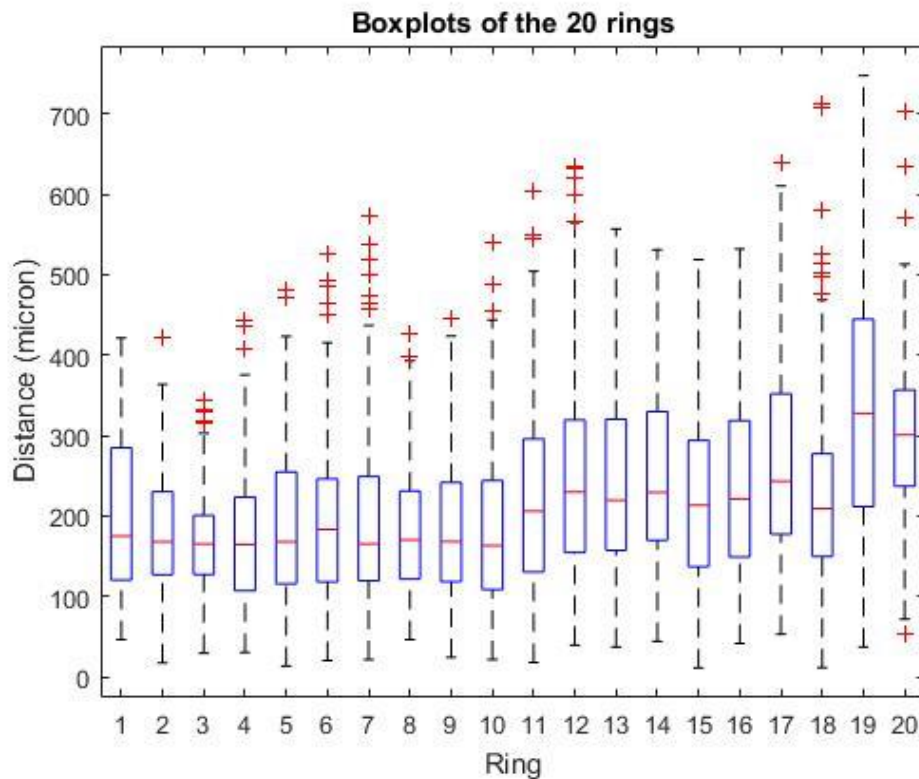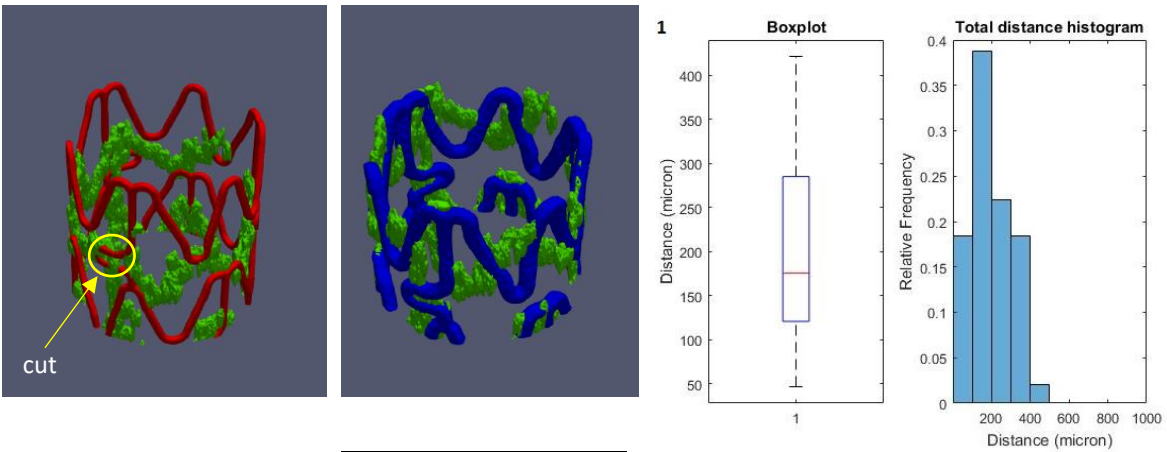

Figure 5.7 Boxplots of the 20 rings. It can be observed that the early rings on the left side (from 1 to 10) tend to have lower point to point distance between the two centerlines. On the other hand, the algorithm performance for the rings at the right side (from 11 to 20) is worse compared to the first rings.
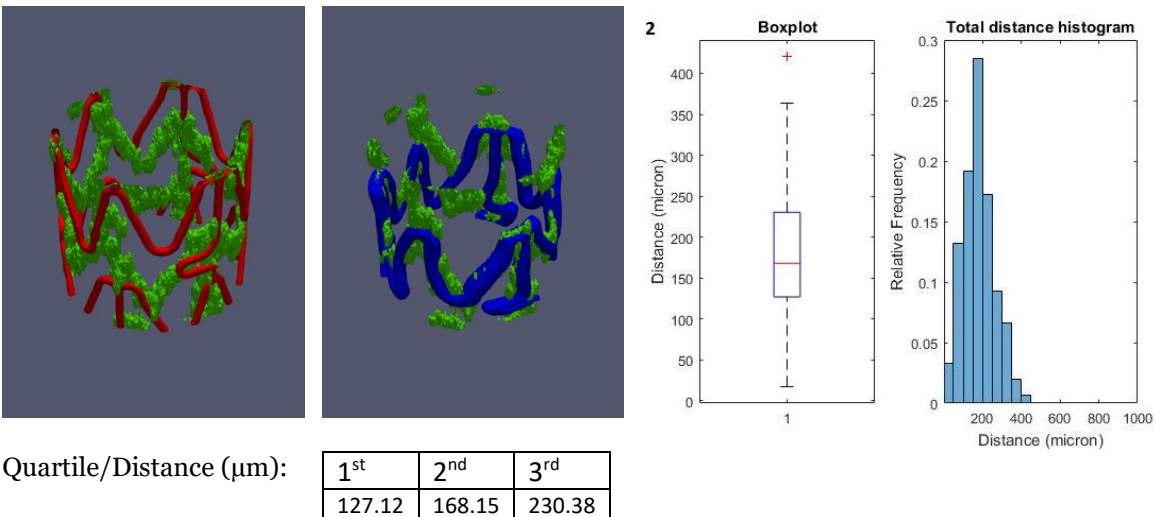
Quartile/Distance (μm):	1st	2nd	3rd
	120.66	175.28	285.01

Figure 5.8 Ring 1. Local registration of the ring. In general, in this image and also in the following images of the rings, it can be observed the results of the subdivision of the stent in which, in order to have a good registration between the moving and the fixed, it is added an overlap layer to the top and to the bottom of the sub-volumes. For this ring, it can be observed a slight worse registration with respect to the rest of the rings in the distal region (rings 1-10). This is probably because the initial position of the two rings are shifted with one respect to another along the longitudinal axis as it can be observed in the comparison between the initial non-deformed ring and the fixed ring.

Quartile/Distance (μm):	1st	2nd	3rd
	127.12	168.15	230.38

Figure 5.9 Ring 2. From this ring the local registration starts to give its first good result with an overall distance between centerlines that decreases compared to the previous ring.

Quartile/Distance (μm):

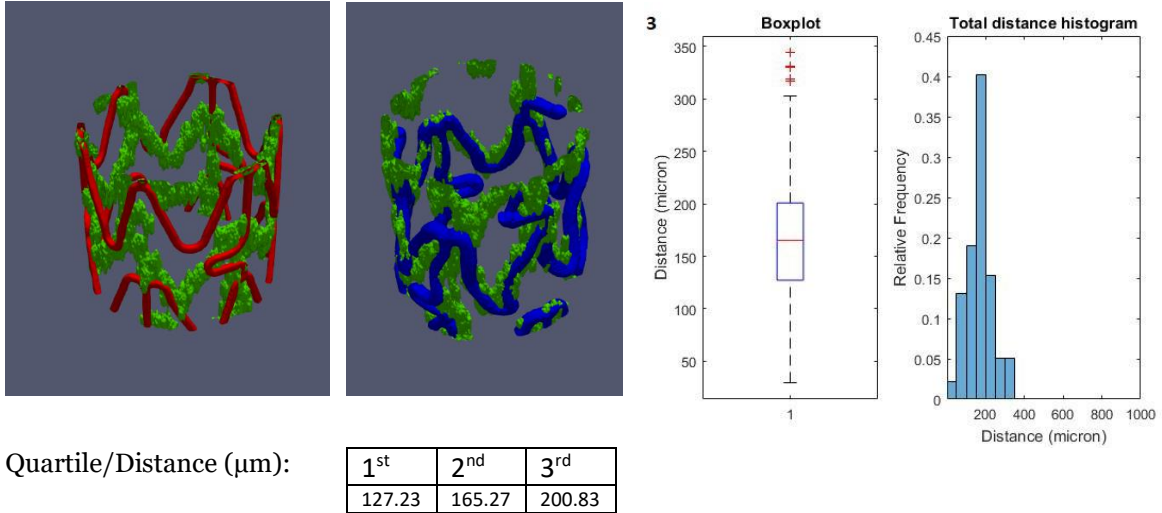| 1ˢᵗ	2ⁿᵈ	3ʳᵈ
127.23	165.27	200.83

Figure 5.10 Ring 3. The local registration in this ring is furtherly improved as it can be observed from the final deformed ring (blue) when it is super-imposed with the fixed ring image (green).

Quartile/Distance (μm):

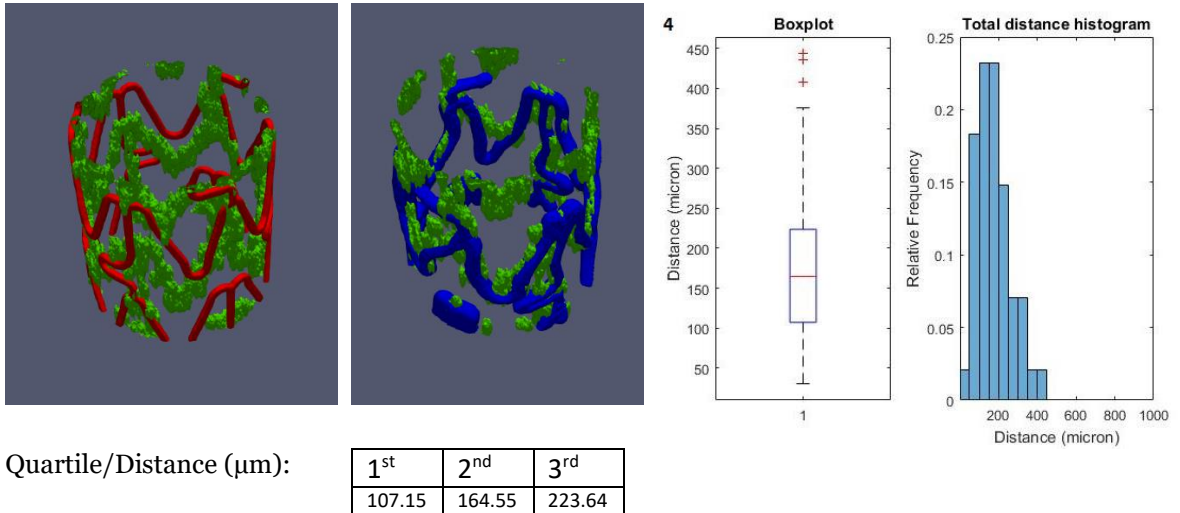| 1ˢᵗ	2ⁿᵈ	3ʳᵈ
107.15	164.55	223.64

Figure 5.11 Ring 4. This is the second ring that had the best result in terms of registration since it has the lowest value of the median. This can be observed on the final image of the deformed ring where it is noticeable a good deformation, with the blue line of the moving stent following the green mesh of the fixed stent.
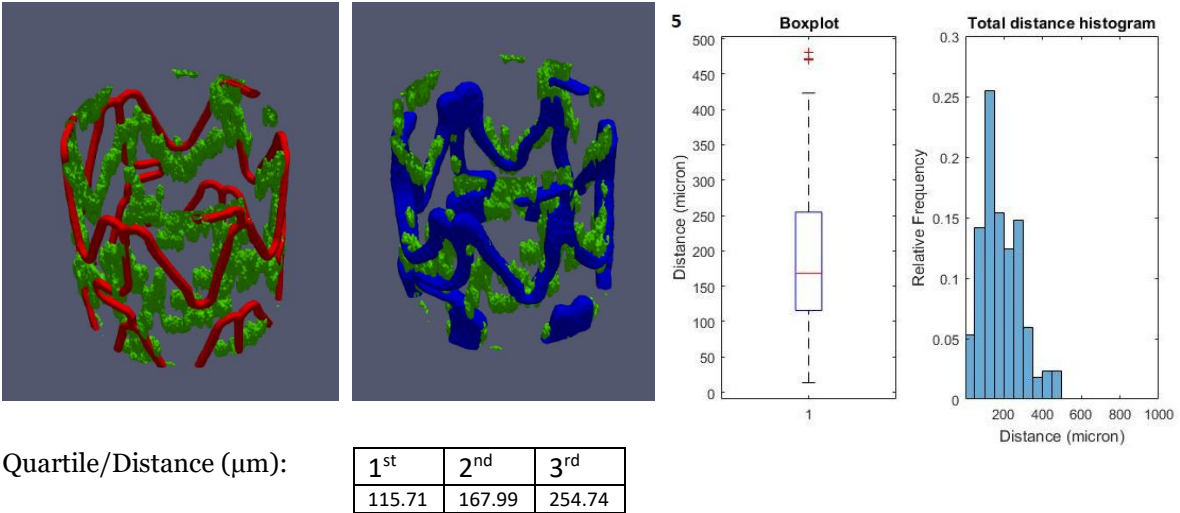
Quartile/Distance (µm):

1st	2nd	3rd
115.71	167.99	254.74

Figure 5.12 Ring 5. Similarly to the last ring, the local registration in this ring performed well.

Quartile/Distance (µm):

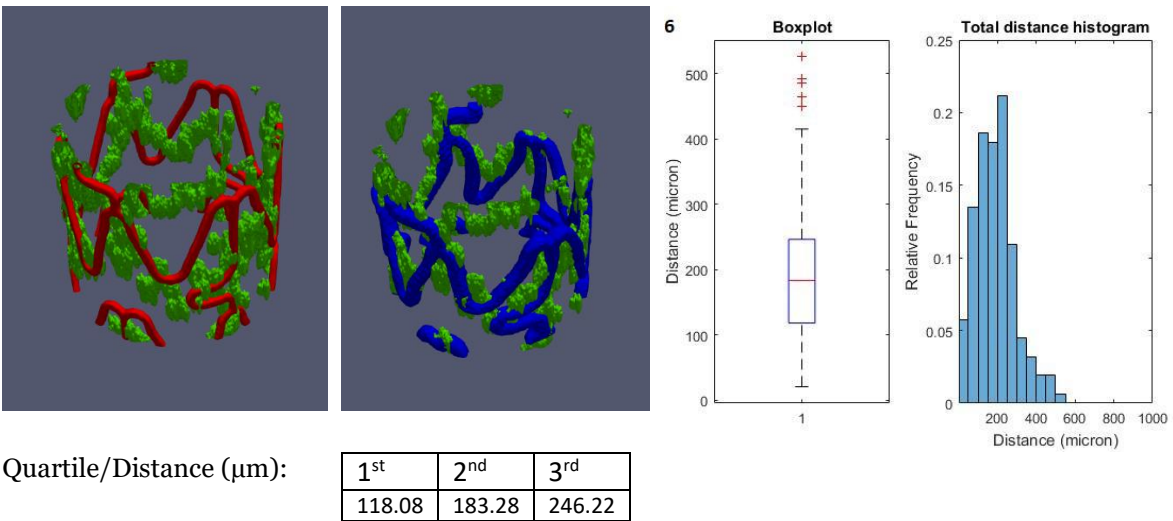| 1st	2nd	3rd
118.08	183.28	246.22

Figure 5.13 Ring 6. In this ring, like in Ring 1, although there is a visibly acceptable result of the registration, the median of the distances shows a higher distance with respect to all the rings in the distal region.

Quartile/Distance (μm):

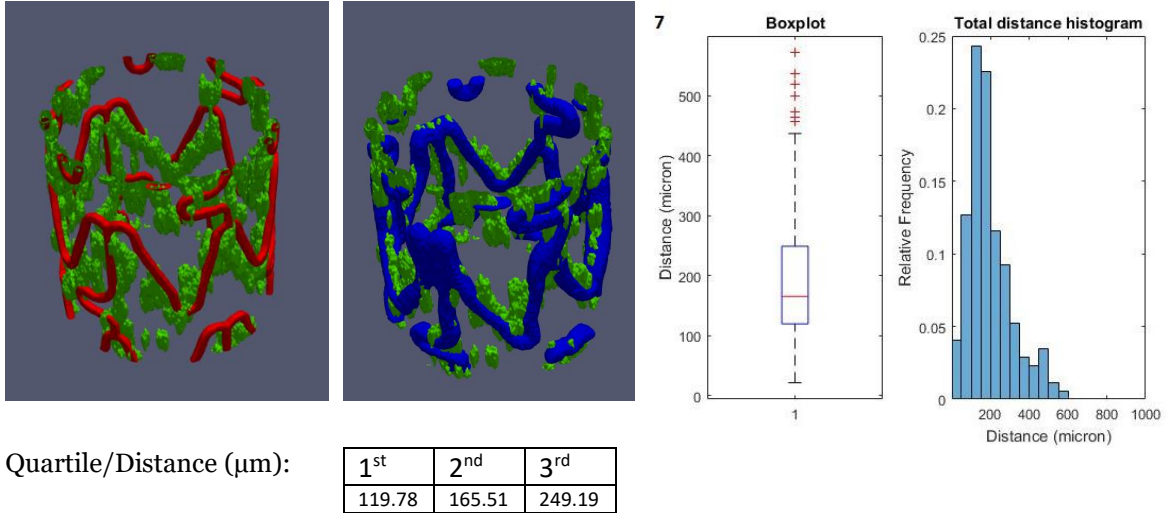| 1ˢᵗ	2ⁿᵈ	3ʳᵈ
119.78	165.51	249.19

Figure 5.14 Ring 7. In this ring, the registration results into a good super-imposition between the moving and the fixed ring like in the previous rings (excluding the Ring 6 and 1)

Quartile/Distance (μm):

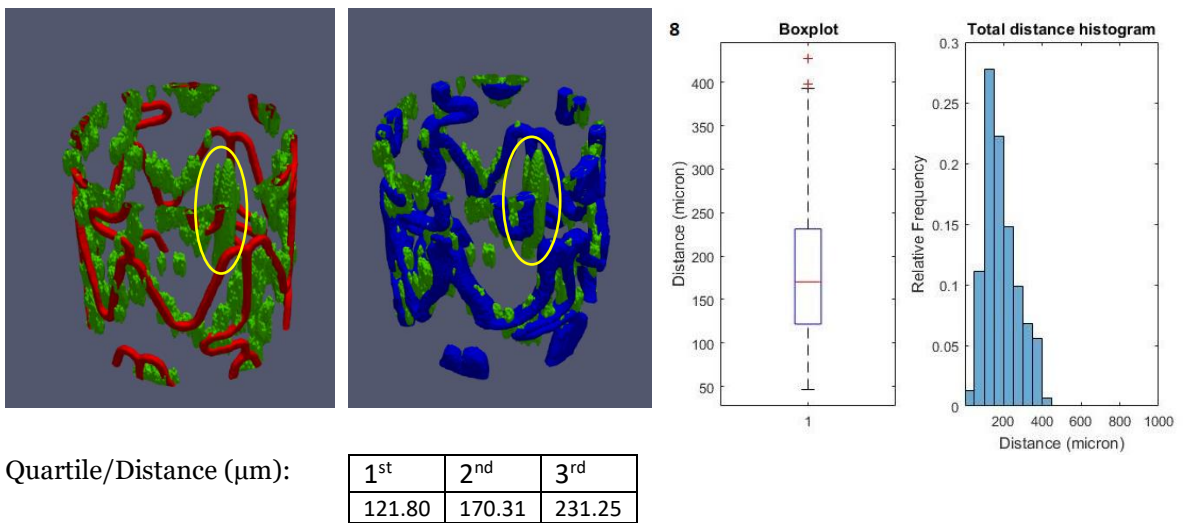| 1ˢᵗ	2ⁿᵈ	3ʳᵈ
121.80	170.31	231.25

Figure 5.15 Ring 8. From this point on, in the fixed image, it can be observed an artifact (highlighted in yellow) in the middle of the stent image. Despite this, the registration performed well and the result is similar to the previous rings.

Quartile/Distance (µm):

1st	2nd	3rd
118.42	168.28	241.87
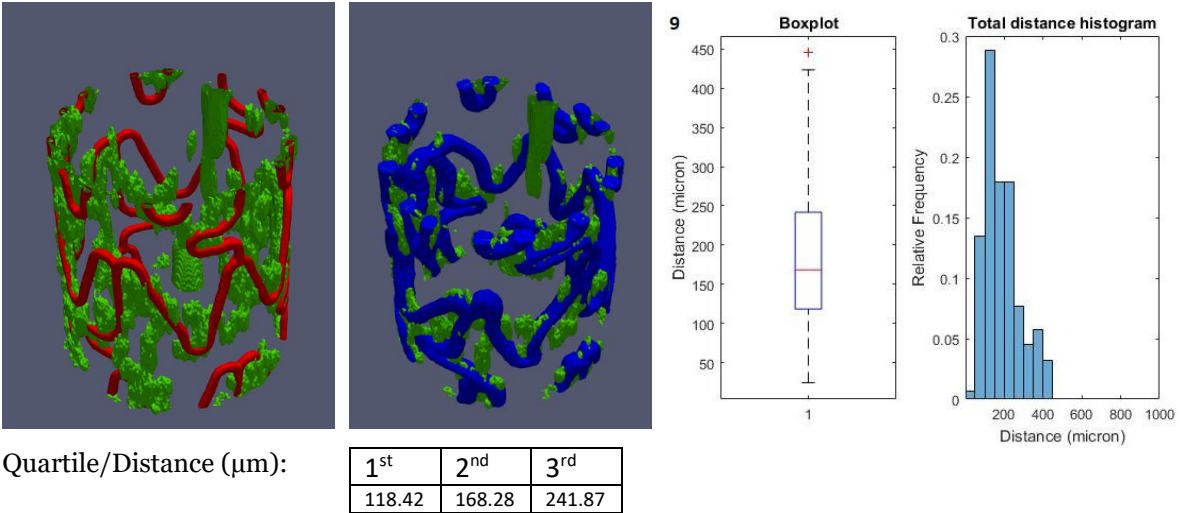
Figure 5.16 Ring 9. In this ring, the resulting registered ring is similar to the previous ones although the artifact is increasing in dimensions.

Quartile/Distance (µm):

1st	2nd	3rd
108.86	163.25	244.32

Figure 5.17 Ring 10. This ring defines the boundary between the non-deformed region of the stent and the deformed region in which the stent has an increased diameter. Numerically, among the other rings, the local registration in this ring had the best result (lowest median) despite the presence of the artifact in the stent image.

Quartile/Distance (μm):
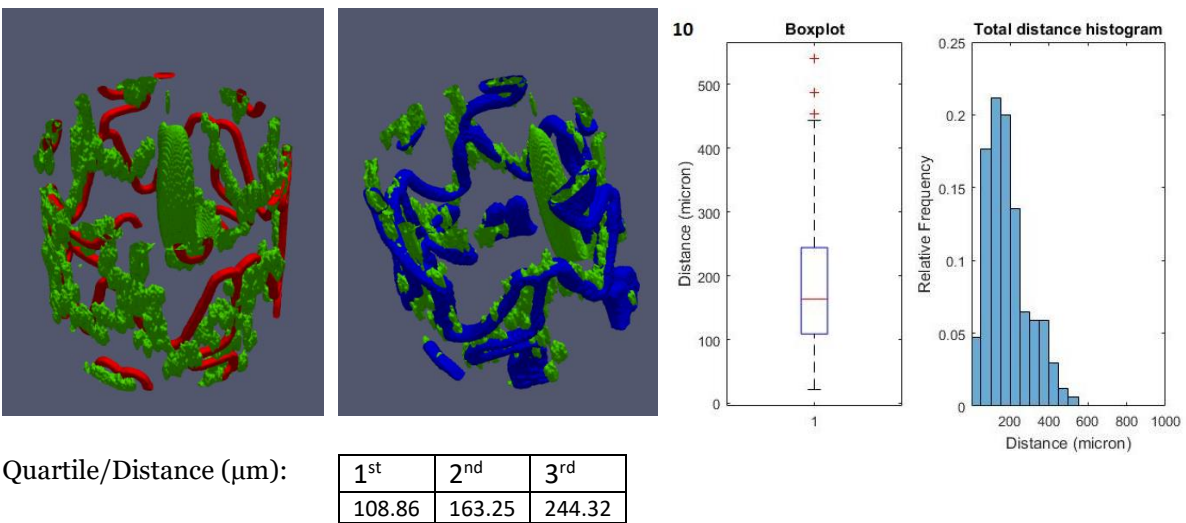
1st	2nd	3rd
130.51	206.25	295.73
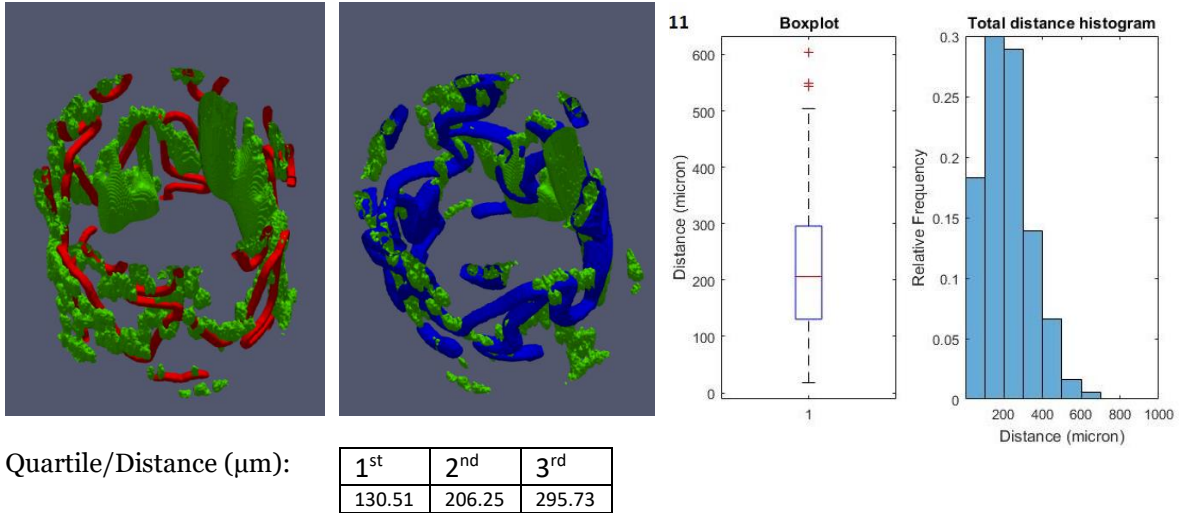
Figure 5.18 Ring 11. The deformation (enlargement of the stent) in this region results into a worse performance of the registration compared to the distal part as it can be observed in the histogram where the distribution of the distance starts to dilate to higher values. This results are similar to the remaining rings of the stent.

Quartile/Distance (μm):

1st	2nd	3rd
154.90	230.08	319.42

Figure 5.19 Ring 12. In this ring as already mentioned in Ring 11, the diameter starts to increase and the scaling transformation in the local registration deforms the moving image so that it can follow the structure of the fixed ring.

Quartile/Distance (µm):

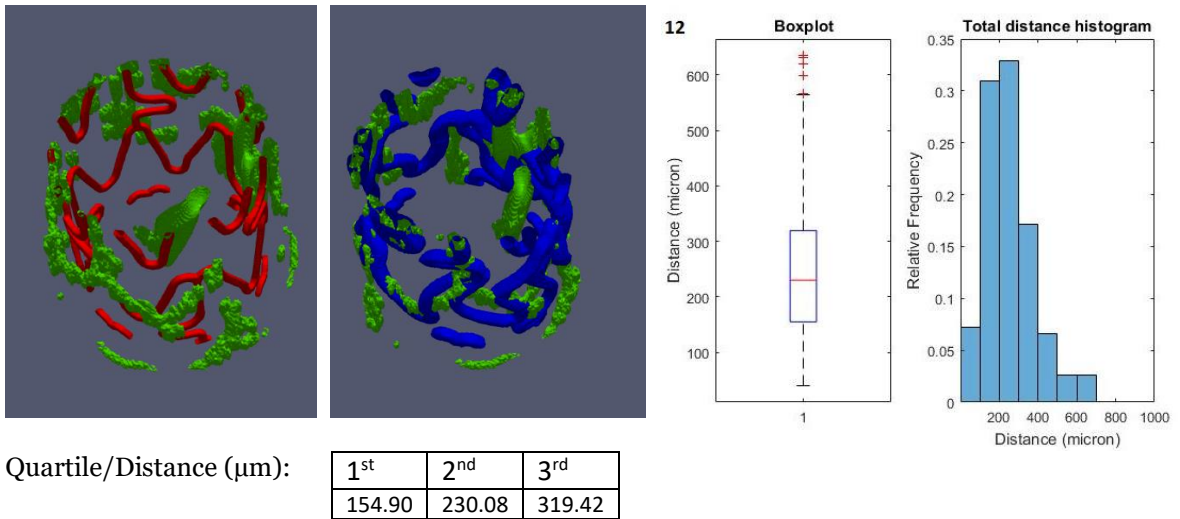| 1st	2nd	3rd
157.58	219.64	320.44
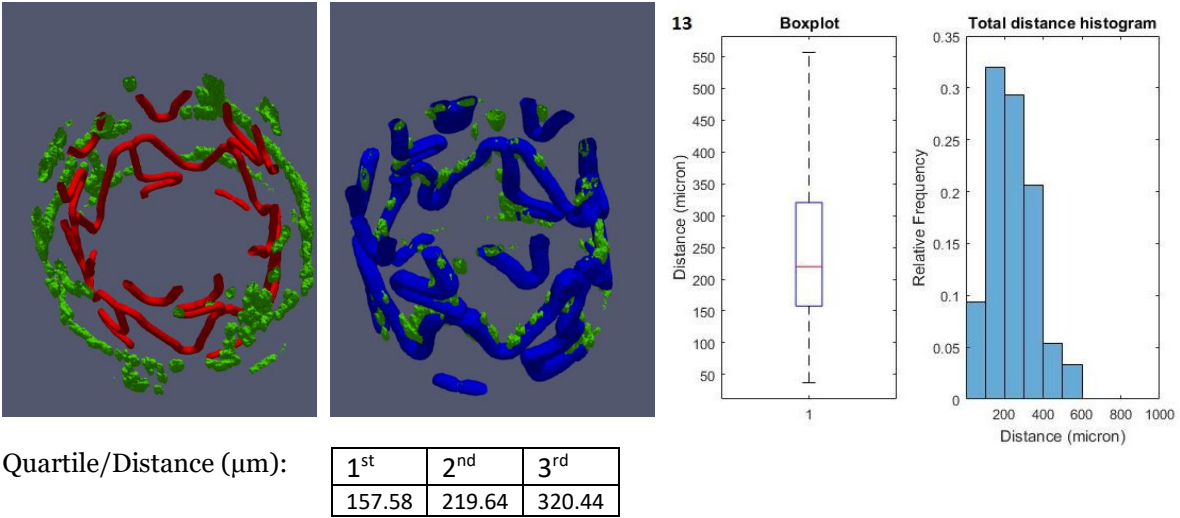
Figure 5.20 Ring 13. In this ring the artifact that compared in the mid-region of the stent is disappeared resulting into a good registration at least from the point of view of rotation and scaling.

Quartile/Distance (µm):

1st	2nd	3rd
169.93	229.44	329.60
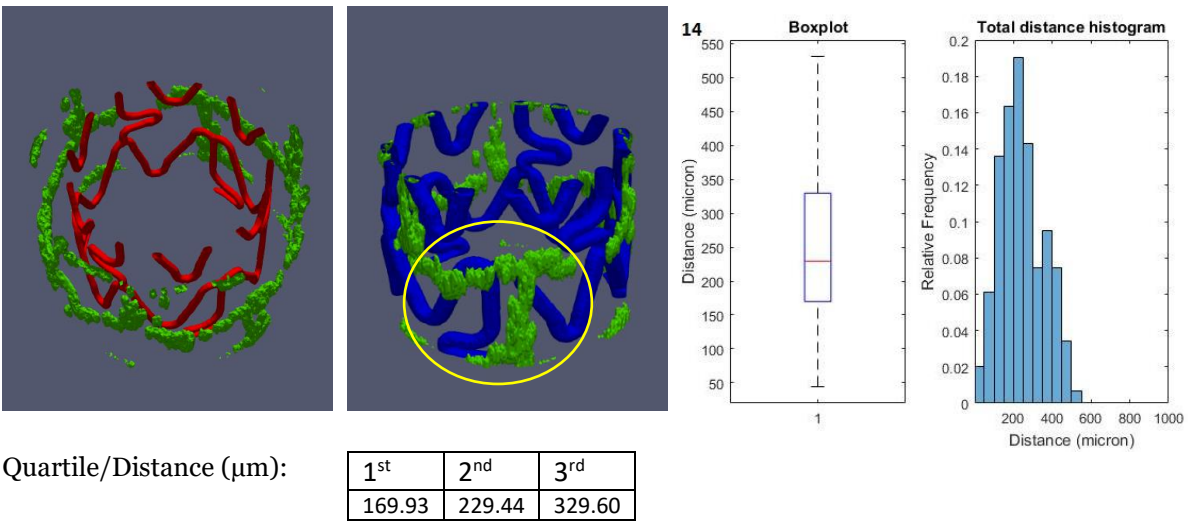
Figure 5.21 Ring 14. In this ring although the scaling performed well it can be observed that the local registration resulted into a lack of rotation as it evidenced in the figure with a yellow circle.

Quartile/Distance (µm):

1st	2nd	3rd
136.94	213.52	294.01
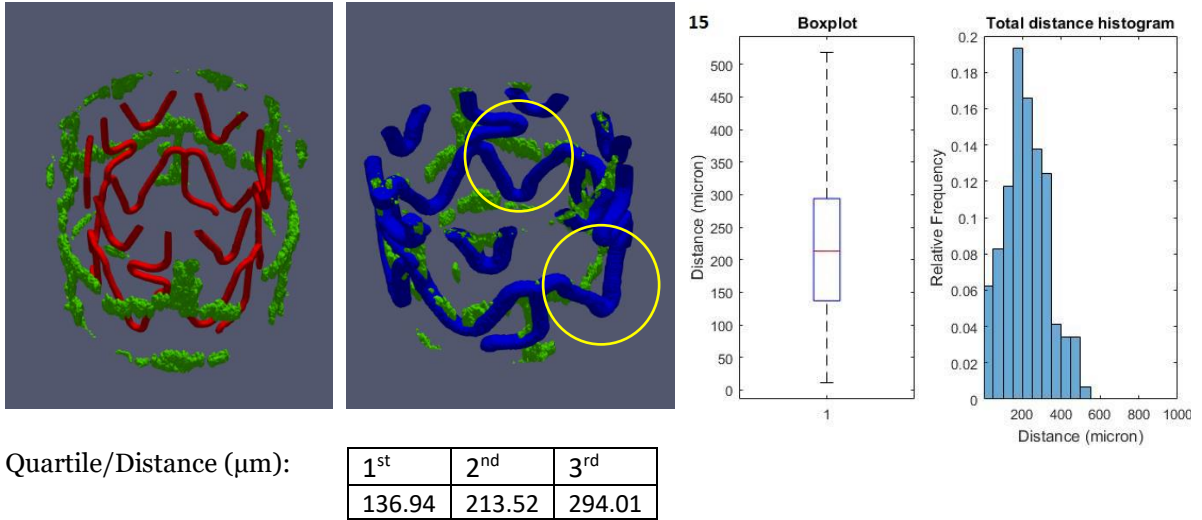
Figure 5.22 Ring 15. In this ring it can be observed a good scaling and rotation similarly to the previous rings but here emerges a problem regarding the non-rigid deformation. One can notice a good macro deformation of the ring but it is also observable that some curves of the fixed images are not completely recovered during the local deformation.

Quartile/Distance (µm):

1st	2nd	3rd
149.32	221.21	318.62
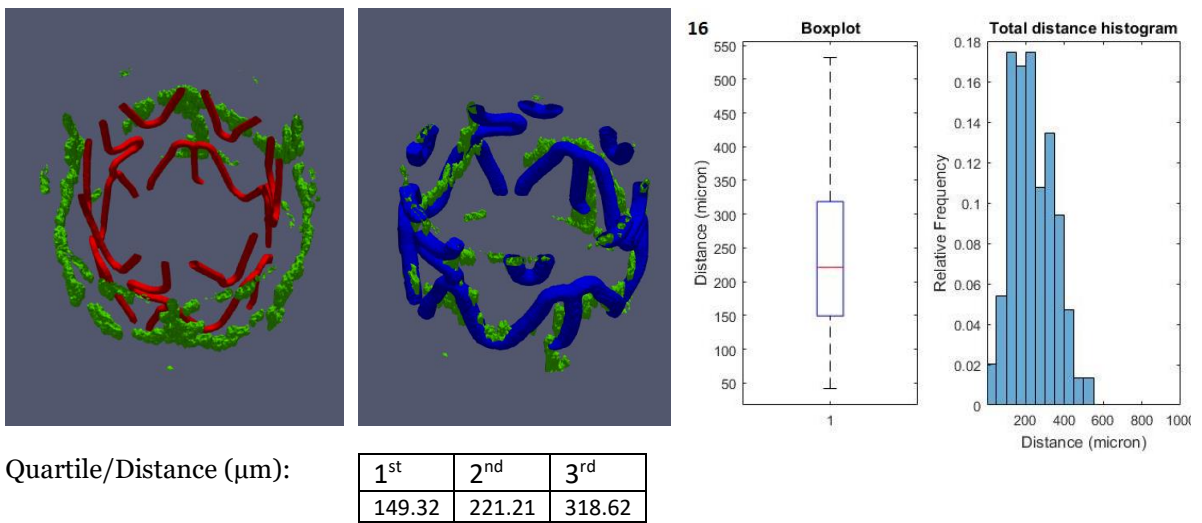
Figure 5.23 Ring 16. Differently from the previous ring, here it can be observed in addition to the good scaling and rotation a bettere local deformation.

Quartile/Distance (μm):	1st	2nd	3rd
	177.59	243.18	351.95
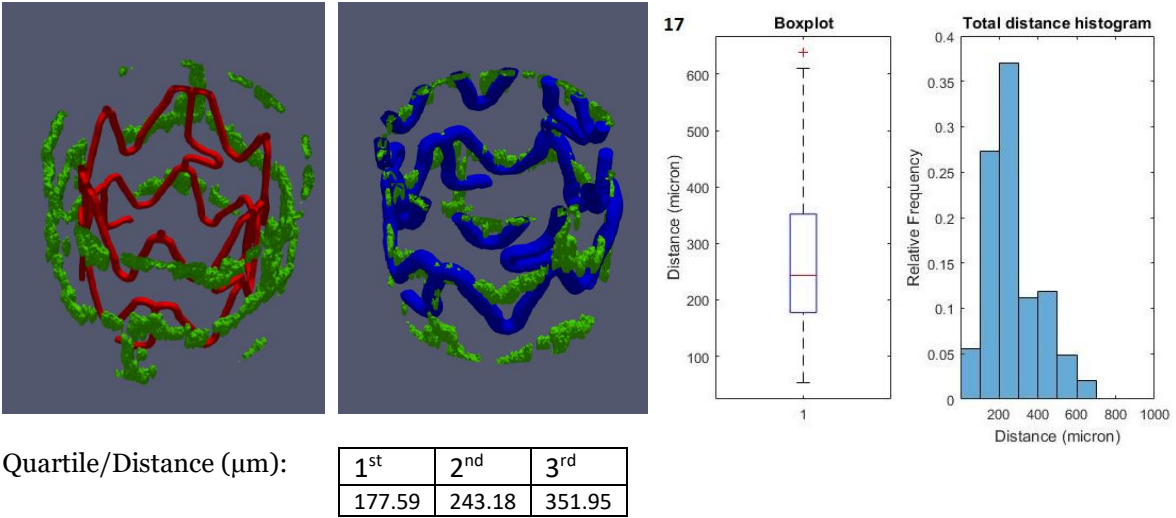
Figure 5.24 Ring 17. Similarly to the Ring 16 but slightly worse, in this ring it can be observed a good scaling and rotation.

Quartile/Distance (μm):	1st	2nd	3rd
	149.82	209.40	277.46
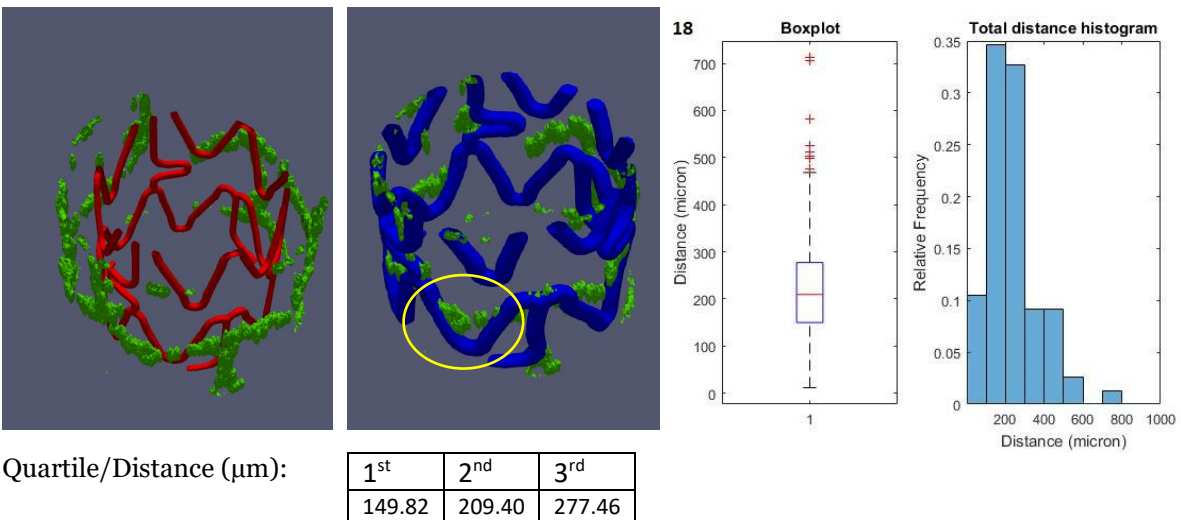
Figure 5.25 Ring 18. In general, the registration in the proximal region of the stent resulted into a good scaling and in part good rotation. The main problem, as shown here is the local deformation that has to be recovered by the non-rigid transformation. Similarly to Ring 15, in this ring it can be observed a resulting misalignment between the the two curves (yellow circle), probably due to the local non-rigid registration.

Quartile/Distance (µm):

1st	2nd	3rd
211.71	327.58	444.65
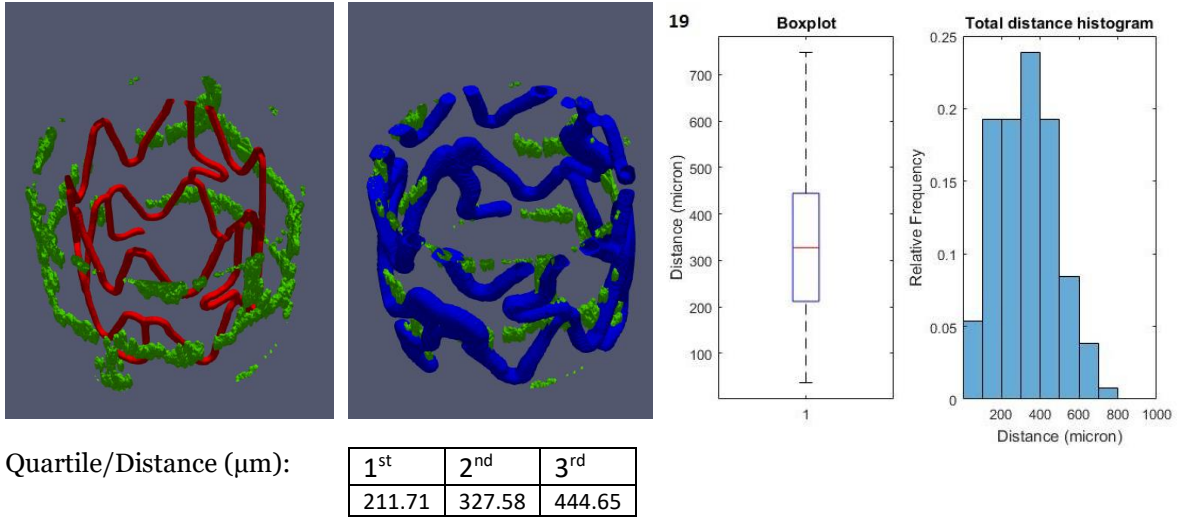
Figure 5.26 Ring 19. In this ring the same problem seen in Ring 18 is observable.

Quartile/Distance (µm):

1st	2nd	3rd
236.99	300.96	356.46

Figure 5.27 Ring 20. The last ring, in which the registration did not performed well due to an evident presence of an artifact in the fixed ring.

5.4.   Results discussions

The image registration that mapped the CAD model to the IVOCT image in this test brought to a visibly good superimposition of the two images, although the distances from respective points is still significantly higher than the ones observed in Bologna's work [17]. This result could be explained in several ways.

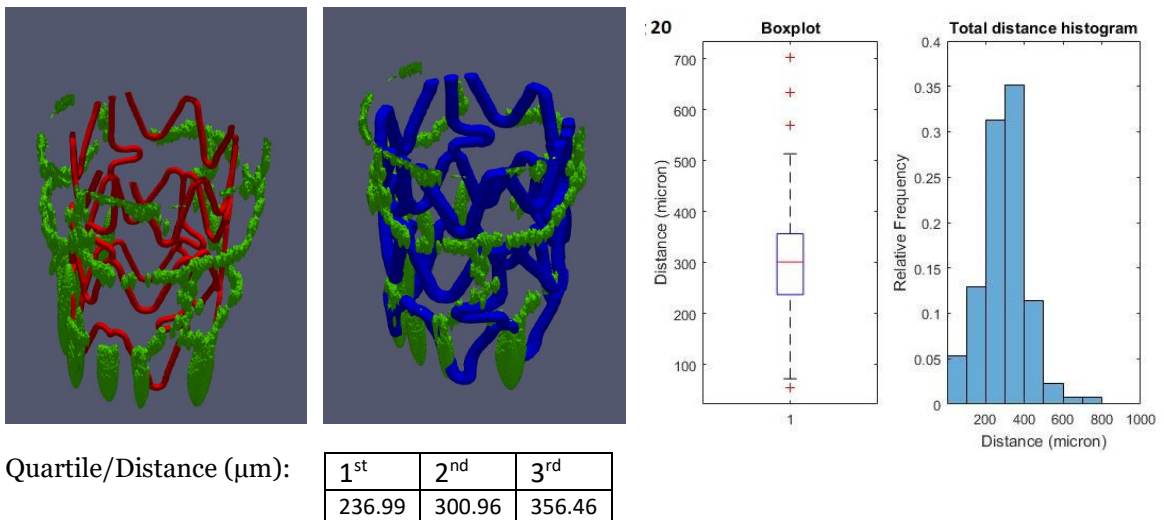One reason is the non-uniformity of the ring-length in IVOCT COP, which may cause a slight dephasing between rings in the longitudinal direction. This could produce problems when performing the local registration. This problem cannot be avoided because it is related to an artifact of the IVOCT image acquisition itself. However, an implementable solution could be considered and that is related to the phase subdivision in rings. In particular, a possible solution could be to increase the the length of the sub-volumes by increasing the overlapping. If the level of overlap with adjacent rings was increased, for example, from 35% (the value used in this thesis) to 50%, that should reduce the effect of the longitudinal dephasing between the respective moving and fixed ring on the final, since the use of larger sub-volumes will allow a better local registration. Another approach could be using sub-volumes that contain more than one ring at a time so that the registration is computed onto bigger volumes, again reducing the effect of the dephasing during the local registration. Both the adjustments assume that sub-volumes larger than a single ring would provide a more complete source and reference and this would improve the image registration procedure. However, the mentioned algorithm adjustments imply the increase of the overall dimension of the volume to register, which, as already pointed out many times before, may cause computer crashes due to the system lack of memory.

The non-uniform rotational distortion along the stent length may be another cause of the difficulty of the registration algorithm. Again, this is an artifact of the OCT image acquisition because of relative movement between the acquisition catheter and the metallic guide wire where the catheter moves. Two are the possible solution to this problem. One solution is to implement a correction for this effect during the point cloud creation, by applying algorithms to eliminate the torque effect along the longitudinal axis, which was not done in our case. Another solution is to correct for this effect during image registration. In this study, we tried to apply the latter type of correction during the local registration. As a matter of fact, we tried to correct for the rotation artifact by saving the last rotation matrix of the nth ring and using it at the beginning of the rotation of the nth+1 ring. This let the nth +1 ring start the rotation to the same point where the last ring had finished and helps reducing the relative twist problem.

Although the relative twist between two rings was partially solved by this, but still there are margins for improvements.

Another possible problem of the registration might be the number of control points used for the non-rigid registration. Since the level of details of the 3D stent in the current procedure is much higher with respect to other image registration problems applied in the biomedical imaging field (i.e., registering a CT with an MRI of the same subject), a higher number of control points must be used to obtain the best deformation. We tried to make the grid as fine as possible, but still we have just a relatively small number of control points . A larger number of control points will certainly lead to a better performance of the registration, but this is made difficult because of hardware limitations. The increase of control points will certainly need a computer with higher level of performance.

Despite this algorithm brought to distances significantly higher compared to other similar 3D stent registration algorithm, if we look at the boxplots and histograms of the distances between corresponding points it can be observed that the array of distances coming from the two experiments are still in the same order of magnitude (~100 – 300 μm), with a difference of 40 μm between the medians. This loss in accuracy can be considered acceptable, if we look at the advantages that come from this algorithm, such as reduced time for registration and semi-automation of the process. As a matter of fact, the time of processing to obtain such comparable results is much less (2-3 days) compared to the algorithms available in the literature (around a week), where manual morphing is adopted, and the part of the algorithm that are manual are just a small portion of the entire workflow.

Decreasing the time to obtain a deformed 3D model of the stent is a particularly important step in the workflow of patient-specific CFD simulations, because it makes the whole process faster and more automatic. From the clinical point of view this would facilitate the analysis of the causes of pathologies such as restenosis and/or thrombosis. In fact, from the literature, it emerges that carrying out CFD analysis on realistic 3D models of stents allows to estimate the local hemodynamics more accurately, bringing to a better understanding about the connection between altered hemodynamics and ISR.

6.

Limitations, future developments and conclusions

In this chapter the final thoughts about the proposed method for stent geometry modeling are exposed. Strengths and weakness of the algorithm are analyzed and compared to the ones found in literature. Limitations of the algorithm and possible solutions of the algorithm are also described.

6.1. Algorithm limitations and future developments

The developed method has some limitations that are herein exposed together with some possible solutions for future developments and improvements.

The sample used in this experiment was only one 3D COP coming from the IVOCT scans of an Abbott Xience V metallic stent. Consequently, the developed algorithm tended to focus on the specific application, losing some of its generalization property. Testing the algorithm into alternative samples would certainly improve the generalization of the method. In fact, the results of this experimentation were obtained by specific image pre-processing and registration parameters, suitable for the sample in analysis. Another consequence of this, is that the transformations sequence during the local registration is fixed in this order: scaling, translation, roto-translation, general affine and B-Spline interpolation. In the case that the algorithm was tested into another sample, this sequence might not be good. The user should have the possibility, by looking to the two images side by side, to choose the best sequence of transformation for each ring. Initially, this was implemented in the algorithm, but it gave problems during the rebuild process of the entire stent.

Another possible improvement is the full automation of the process, avoiding the use of GUI's. The user should be able to input the two images to register and just wait for the output, without interacting with the process. This would certainly imply a higher level of implementation, with the need of an auto optimization of the registration parameters. For example, by using a genetic algorithm (GA), it is possible to obtain the best parameters by means of a minimization of the output, given a set of optimized parameters. Such solution would substitute the GUI's for the parameters input of the registration, but, on the other hand, would increase the time of calculation, since this optimization process is done for each transformation, and not only once unlike the actual application, where the parameters are set by the user.

In this algorithm, the registration metric was fixed into MSE and MI in the global and only MI during the local registration. In the executables there are also available other metrics such as NGF and metrics combination (MI+NGF). The computational cost and the time required for each entire stent registration brought to the choice of only MSE and MI, which were the metrics that gave at first the best results. This does not mean that they are the best metric among those that are cited. A complementary study of the metric optimization for this application could deliver another improvement of the entire process.

6.2. Conclusions

In this thesis, a method for 3D stent morphing of an undeformed CAD to an IVOCT COP is developed. The method should provide a useful semi-automated tool to create a realistic 3D model of a stent implanted in the blood vessel. Such model may be used to perform CFD simulations that provide an accurate instrument for the determination of variables such as the WSS. This would eventually allow to make a detailed analysis of the relationship between these variables and the main problematics that characterize the post-implant phase of a stent, i.e. ISR.

The entire algorithm was written in MATLAB and includes the GUI's (for image creation and registration parameters input) and the image registration, which is fully automatized and performs the automatic mapping of the CAD (moving image) with respect to the IVOCT image (fixed image). In the first phase of image processing, the model and the IVOCT images are created, followed by the binarization and the trimming. The latter eliminates the voxels that are useless for the registration, decreasing in this way, the calculation time. The second phase is the image registration, which is divided in global and local. In the global, the moving stent is pre-aligned to the fixed stent through a translation and a roto-translation transformation. Its purpose is to facilitate the local registration by globally moving the entire stent model to the IVOCT image. In fact, the global is the preparation for the next phase, the local registration, where the main objective is to subdivide the computation volume into a smaller image space for the registration procedure, by applying these transformations in sequence: scaling, translation, roto-translation, general affine and B-Spline interpolation. These operations were only possible for the rings, since, if applied to the entire stent, they would cause computer crashes. The tridimensional stent model geometry is obtained after rebuilding the registered rings images, to form the entire stent. Such operation is done by considering the VF that were created in each transformation of the local registration. The actual rebuild process, for each transformation, is applied to these VF and the final registered image is obtained by warping them in cascade, starting from the initial non-deformed model image, in the same sequence of transformations seen in the local registration.

The evaluation of the algorithm was performed only for one sample of 3D COP which was obtained from the segmentation of IVOCT images of an implanted metallic stent. The resulting final registered model visibly gave a good sense of superimposition, especially in the distal region, where the stents structures almost perfectly matched. On the other hand, in the proximal region, the algorithm had a little bit of difficulty to provide a good matching due to the increase in diameter of the fixed image, that required a higher level of calculations. Despite

this, a deformation in a macro level in the radial direction was still obtained. The difference in terms of performance of the two regions was also demonstrated by the numerical evaluation as shown in the boxplots of all the rings in Figure 5.7. In fact, it can be observed a shifting of the boxplots towards the top from the distal to the proximal part, which asserts the increase in distance of the registered model and the IVOCT COP centerlines.

The statistical analysis was performed on the entire stent. The distribution of the distances between corresponding points of the centerlines of the stent obtained by IVOCT and CAD was compared to the distance obtained from the centerlines of IVOCT and micro CT. This resulted into a worse overall performance of the IVOCT-CAD registration. In fact, it could be observed a higher distance distribution in the proposed algorithm with respect to the mentioned method. Despite this, the order of magnitude of both distributions are still in the same level and, in addition, the proposed algorithm can exhibit features that other methods seen in literature lack. As a matter of fact, most of the algorithms for stent reconstruction from COP, starting from the segmentation of the IVOCT images, use a morphing procedure in which the centerline of a free expanded stent (from µCT scans) is move to points belonging to the COP, minimizing their distance [2]. Such procedure is done manually and to obtain the final stent geometry it could take several days. In contrast, in the proposed method, although it is only semi-automatic, once the parameters of the registration are set, the process does not require any user interaction and the time of application is shorter.

In conclusion, in this study it has been demonstrated that morphing procedure of a stent can be semi-automatized. Although the method presents some limitations, it solves most of the main flaws in other methods, such as time and automation. Moreover, the proposed method has the objective of setting the basis of the process automation and speeding, which will certainly decrease the level of difficulty in obtaining 3D stent models for CFD simulations.

Bibliography

[1]   F. Andrew D. Michaels, MD; Kanu Chatterjee, MB, "Angioplasty Versus Bypass Surgery for Coronary Artery Disease," *Circulation*, vol. 106, no. 22, p. 176e–178, 2002.

[2]   S. Migliori *et al.*, "A framework for computational fluid dynamic analyses of patient-specific stented coronary arteries from optical coherence tomography images," *Elsevier*, p. 12, 2017.

[3]   C. Chiastra, S. Migliori, F. Burzotta, G. Dubini, and F. Migliavacca, "Patient-Specific Modeling of Stented Coronary Arteries Reconstructed from Optical Coherence Tomography: Towards a Widespread Clinical Use of Fluid Dynamics Analyses," *Journal of Cardiovascular Translational Research*, pp. 1–17, 2017.

[4]   G. Ferrante, P. Presbitero, R. Whitbourn, and P. Barlis, "Current applications of optical coherence tomography for coronary intervention," *International Journal of Cardiology*, vol. 165, no. 1. pp. 7–16, 2013.

[5]   L. Vignali, E. Solinas, and E. Emanuele, "Research and Clinical Applications of Optical Coherence Tomography in Invasive Cardiology : A Review," *Curr. Cardiol. Rev.*, vol. 10, no. 4, pp. 369–376, 2014.

[6]   L. M. Ellwein *et al.*, "Optical Coherence Tomography for Patient-specific 3D Artery Reconstruction and Evaluation of Wall Shear Stress in a Left Circumflex Coronary Artery," *Cardiovasc. Eng. Technol.*, vol. 2, no. 3, pp. 212–227, 2011.

[7]   M. I. Papafaklis *et al.*, "In vivo assessment of the three-dimensional haemodynamic micro-environment following drug-eluting bioresorbable vascular scaffold implantation in a human coronary artery: Fusion of frequency domain optical coherence tomography and angiography," *EuroIntervention*, vol. 9, no. 7, p. 890, 2013.

[8]   C. V. Bourantas *et al.*, "Fusion of optical coherence tomographic and angiographic data for more accurate evaluation of the endothelial shear stress patterns and neointimal distribution after bioresorbable scaffold implantation: Comparison with intravascular ultrasound-derived rec," *Int. J. Cardiovasc. Imaging*, vol. 30, no. 3, pp. 485–494, 2014.

[9]   C. V. Bourantas *et al.*, "Effect of the endothelial shear stress patterns on neointimal proliferation following drug-eluting bioresorbable vascular scaffold implantation: An optical coherence tomography study," *JACC Cardiovasc. Interv.*, vol. 7, no. 3, pp. 315–324, 2014.

[10]   E. Tenekecioglu *et al.*, "Corrigendum to 'Assessment of the hemodynamic characteristics of Absorb BVS in a porcine coronary artery model' [Int. J. Cardiol. 227 (2017) 467–473]

(S0167527316334064)(10.1016/j.ijcard.2016.11.005)," *International Journal of Cardiology*, vol. 235. p. 206, 2017.

[11] E. Tenekecioglu, R. Torii, C. V. Bourantas, R. Al-Lamee, and P. W. Serruys, "Non-Newtonian pulsatile shear stress assessment: A method to differentiate bioresorbable scaffold platforms," *European Heart Journal*, vol. 38, no. 33. p. 2570, 2017.

[12] E. Tenekecioglu *et al.*, "Preclinical assessment of the endothelial shear stress in porcine-based models following implantation of two different bioresorbable scaffolds: Effect of scaffold design on the local haemodynamic micro-environment," *EuroIntervention*, vol. 12, no. 10. p. 1296, 2016.

[13] E. Tenekecioglu *et al.*, "The effect of strut thickness on shear stress distribution in a preclinical model," *Int. J. Cardiovasc. Imaging*, vol. 33, no. 11, pp. 1675–1676, 2017.

[14] V. Thondapu, E. Tenekecioglu, E. K. W. Poon, Y. Onuma, and P. W. Serruys, "Improvement in local haemodynamics 5 years after implantation of a coronary bioresorbable scaffold: A pulsatile non-Newtonian shear stress analysis," *European Heart Journal Cardiovascular Imaging*, vol. 18, no. 11. p. 1294, 2017.

[15] R. Torii *et al.*, "Five-year follow-up of underexpanded and overexpanded bioresorbable scaffolds: Self-correction and impact on shear stress," *EuroIntervention*, vol. 12, no. 17. pp. 2158–2159, 2017.

[16] C. C. O'Brien *et al.*, "Constraining OCT with knowledge of device design enables high accuracy hemodynamic assessment of endovascular implants," *PLoS One*, vol. 11, no. 2, 2016.

[17] M. Bologna, "Sviluppo di un metodo di creazione di modelli 3D di biforcazioni coronariche con stent per simulazioni fluidodinamiche a partire da immagini di tomografia a coerenza ottica," 2015.

[18] M. T. Todd Neale, "Thrombosis Risk Lower with Xience Stent," *March 23*, 2012. [Online]. Available: https://www.medpagetoday.com/cardiology/pci/31788.

[19] KitWare, "Insight ToolKit." [Online]. Available: https://itk.org/.

[20] E. Montin, "A novel image registration strategy for oncological pediatric images brain fusion," Politecnico di Milano.

[21] S. Khonsary, "Guyton and Hall: Textbook of Medical Physiology," *Surg. Neurol. Int.*, vol. 8, no. 1, p. 275, 2017.

[22] Z. D. Balboni G.C., Bastianini A., Brizzi E., Castorina S., Comparini L., Donato R.F., Filogamo G., Fusaroli P., Lanza G.G., Grossi C.E., Manzoli F.A., Marinozzi G., Miani A., Mitolo V., Motta P.,

Bibliography

Nesci E., Orlandini G.E., Passaponti A., Pizzini G., Reale E., R, *Anatomia umana - Volume primo*, 3a ed. Edi-Ermes, 1997.

[23] K. B. Manning, K. B. Chandran, S. E. Rittgers, and A. P. Yoganathan, *Biofluid Mechanics: The Human Circulation (second edition)*, vol. 3, no. 4. 2012.

[24] Euroform Healthcare, "Normal Coronary Blood Flow." [Online]. Available: http://www.euroformhealthcare.biz/medical-physiology/normal-coronary-blood-flow.html.

[25] NHBLI, "Coronary heart disease." [Online]. Available: https://www.nhlbi.nih.gov/health-topics/coronary-heart-disease.

[26] D. F. Young and F. Y. Tsai, "Flow characteristics in models of arterial stenoses - II. Unsteady flow," *J. Biomech.*, vol. 6, no. 5, pp. 547–559, 1973.

[27] K. MedTrip, "BYPASS-SURGERY (CABG)." [Online]. Available: https://www.kansanmedtrip.com/BYPASS-SURGERY.php.

[28] Wikipedia, "Minimally invasive cardiac surgery." [Online]. Available: https://en.wikipedia.org/.

[29] J. Iqbal, J. Gunn, and P. W. Serruys, "Coronary stents: Historical development, current status and future directions," *British Medical Bulletin*, vol. 106, no. 1. pp. 193–211, 2013.

[30] B. Chandrasekar and J. F. Tanguay, "Platelets and restenosis," *J. Am. Coll. Cardiol.*, vol. 35, no. 3, pp. 555–562, 2000.

[31] S. Garg and P. W. Serruys, "Coronary stents: Current status," *Journal of the American College of Cardiology*, vol. 56, no. 10 SUPPL. 2010.

[32] D. Fornell, "Bioresorbable Stents Are the Way of the Future," *Daic*, 2014. [Online]. Available: https://www.dicardiology.com/article/bioresorbable-stents-are-way-future.

[33] G. Dangas and F. Kuepper, "Restenosis: Repeat narrowing of a coronary artery - Prevention and treatment," *Circulation*, vol. 105, no. 22, pp. 2586–2587, 2002.

[34] E. A. Murphy and F. J. Boyle, "Reducing In-Stent Restenosis Through Novel Stent Flow Field Augmentation," *Cardiovascular Engineering and Technology*, vol. 3, no. 4. pp. 353–373, 2012.

[35] E. R. Edelman and C. Rogers, "Pathobiologic responses to stenting," in *American Journal of Cardiology*, 1998, vol. 81, no. 7 A.

[36] D. S. Wah, Y. Wang, Y. Q. Wang, R. Y. Zhang, and M. Chui, "Multivessel spasm during coronary and peripheral angiography.," *J. Invasive Cardiol.*, vol. 13, no. 4, pp. 320–322, 2001.

[37] C. V. Bourantas, S. Garg, K. K. Naka, A. Thury, A. Hoye, and L. K. Michalis, "Focus on the research utility of intravascular ultrasound - Comparison with other invasive modalities," *Cardiovascular Ultrasound*, vol. 9, no. 1. 2011.

[38]   E. Escolar, G. Weigold, A. Fuisz, and N. J. Weissman, "New imaging techniques for diagnosing coronary artery disease.," *CMAJ*, vol. 174, no. 4, pp. 487–95, 2006.

[39]   E. M. Tuzcu, O. Bayturan, and S. Kapadia, "Coronary intravascular ultrasound: A closer view," *Heart*, vol. 96, no. 16, pp. 1318–1324, 2010.

[40]   D. Huang *et al.*, "Optical coherence tomography.," *Science*, vol. 254, no. 5035. pp. 1178–81, 1991.

[41]   J. G. Fujimoto, C. Pitris, S. A. Boppart, and M. E. Brezinski, "Optical Coherence Tomography: An Emerging Technology for Biomedical Imaging and Optical Biopsy," *Neoplasia*, vol. 2, no. 1–2, pp. 9–25, 2000.

[42]   F. Prati, M. W. Jenkins, A. Di Giorgio, and A. M. Rollins, "Intracoronary optical coherence tomography, basic theory and image acquisition techniques.," *Int. J. Cardiovasc. Imaging*, vol. 27, no. 2, pp. 251–8, 2011.

[43]   L. S. Athanasiou *et al.*, "3D reconstruction of coronary arteries using frequency domain optical coherence tomography images and biplane angiography.," *Conf. Proc. IEEE Eng. Med. Biol. Soc.*, vol. 2012, pp. 2647–50, 2012.

[44]   H. G. Bezerra, M. A. Costa, G. Guagliumi, A. M. Rollins, and D. I. Simon, "Intracoronary Optical Coherence Tomography: A Comprehensive Review," *JACC Cardiovasc. Interv.*, vol. 2, no. 11, pp. 1035–1046, 2009.

[45]   R. Hamdan, R. G. Gonzalez, S. Ghostine, and C. Caussin, "Optical coherence tomography: From physical principles to clinical applications," *Archives of Cardiovascular Diseases*, vol. 105, no. 10. pp. 529–534, 2012.

[46]   R. Waksman, H. Kitabata, F. Prati, M. Albertucci, and G. S. Mintz, "Intravascular ultrasound versus optical coherence tomography guidance," *Journal of the American College of Cardiology*, vol. 62, no. 17 SUPPL. 2013.

[47]   E. A. Mehanna, G. F. Attizzani, H. Kyono, M. Hake, and H. G. Bezerra, "Assessment of coronary stent by optical coherence tomography, methodology and definitions," *Int. J. Cardiovasc. Imaging*, vol. 27, no. 2, pp. 259–269, 2011.

[48]   T. S. Yoo *et al.*, "Engineering and algorithm design for an image processing API: A technical report on ITK - The Insight Toolkit," in *Studies in Health Technology and Informatics*, 2002, vol. 85, pp. 586–592.

[49]   B. Zitová and J. Flusser, "Image registration methods: A survey," *Image and Vision Computing*, vol. 21, no. 11. pp. 977–1000, 2003.

[50] W. M. Wells, P. Viola, H. Atsumi, S. Nakajima, and R. Kikinis, "Multi-modal volume registration by maximization of mutual information," *Med. Image Anal.*, vol. 1, no. 1, pp. 35–51, 1996.

[51] W. R. Crum, T. Hartkens, and D. L. G. Hill, "Non-rigid image registration: theory and practice," *Br. J. Radiol.*, vol. 77, no. suppl_2, pp. S140–S153, 2004.

[52] M. Holden, "A review of geometric transformations for nonrigid body registration," *IEEE Trans. Med. Imaging*, vol. 27, no. 1, pp. 111–128, 2008.

[53] M. P. Wachowiak, R. Smolíková, Y. Zheng, J. M. Zurada, and A. S. Elmaghraby, "An approach to multimodal biomedical image registration utilizing particle swarm optimization," *IEEE Trans. Evol. Comput.*, vol. 8, no. 3, pp. 289–301, 2004.

[54] D. Mattes, D. R. Haynor, H. Vesselle, T. K. Lewellen, and W. Eubank, "PET-CT image registration in the chest using free-form deformations," *IEEE Trans. Med. Imaging*, vol. 22, no. 1, pp. 120–128, 2003.

[55] D. Mattes, D. R. Haynor, H. Vesselle, T. K. Lewellyn, and W. Eubank, "Nonrigid multimodality image registration," in *SPIE Medical Imaging*, 2001, vol. 4322, pp. 1609–1620.

[56] J. P. W. Pluim, J. B. A. A. Maintz, and M. A. Viergever, "Mutual-information-based registration of medical images: A survey," *IEEE Transactions on Medical Imaging*, vol. 22, no. 8. pp. 986–1004, 2003.

[57] E. Haber and J. Modersitzki, "Intensity gradient based registration and fusion of multi-modal images," *Methods of Information in Medicine*, vol. 46, no. 3. pp. 292–299, 2007.

[58] B. B. Avants, N. J. Tustison, M. Stauffer, G. Song, B. Wu, and J. C. Gee, "The Insight ToolKit image registration framework," *Front. Neuroinform.*, vol. 8, 2014.

[59] M. Simonovsky, B. Gutiérrez-Becker, D. Mateus, N. Navab, and N. Komodakis, "A deep metric for multimodal registration," in *Lecture Notes in Computer Science (including subseries Lecture Notes in Artificial Intelligence and Lecture Notes in Bioinformatics)*, 2016, vol. 9902 LNCS, pp. 10–18.

[60] G. Song, J. Han, Y. Zhao, Z. Wang, and H. Du, "A Review on Medical Image Registration as an Optimization Problem," *Curr. Med. Imaging Rev.*, vol. 13, no. 3, 2017.

[61] S. M. Hughes and I. Daubechies, "Simpler alternatives to information theoretic similarity metrics for multimodal image alignment," in *Proceedings - International Conference on Image Processing, ICIP*, 2006, pp. 365–368.

[62] F. Maes, A. Collignon, D. Vandermeulen, G. Marchal, and P. Suetens, "Multimodality image registration by maximization of mutual information," *IEEE Trans. Med. Imaging*, vol. 16, no. 2,

pp. 187–198, 1997.

[63] G. Wollny, M. J. Ledesma-carbayo, and A. Santos, "An ITK implementation of the Normalized Gradient Field Image to Image Metric," *Insight J. - 2010 January-June.*, 2010.

[64] A. Gomez, "Medical Imaging Processing Toolbox ver 1.3," *MATLAB, MathWorks*. [Online]. Available: https://it.mathworks.com/matlabcentral/fileexchange/41594-medical-image-processing-toolbox?focused=6499080&tab=function.

[65] N. J. Tustison and J. C. Gee, "Generalized n-D C k B-Spline Scattered Data Approximation with Confidence Values," in *Lecture Notes in Computer Science*, no. September 2017, 2006, pp. 76–83.

[66] S. Lee, G. Wolberg, and S. Y. Shin, "Scattered data interpolation with multilevel b-splines," *IEEE Trans. Vis. Comput. Graph.*, vol. 3, no. 3, pp. 228–244, 1997.

[67] C. Leila Baghdadi, MICe, Hospital for Sick Childern, Toronto, "Convert Triangle Mesh To Binary Image," *Insight Journal*. [Online]. Available: https://itk.org/ITKExamples/src/Core/Mesh/ConvertTriangleMeshToBinaryImage/Documentation.html.